

ASSESSMENT OF THE PETROLEUM GENERATION POTENTIAL OF THE NEAL SHALE
IN THE BLACK WARRIOR BASIN, ALABAMA

by

JOEL ARTHUR LEGG

RONA J. DONAHOE, COMMITTEE CHAIR

ANDREW M. GOODLIFFE

JACK C. PASHIN

YUEHAN LU

A THESIS

Submitted in partial fulfillment of the requirements
for the degree of Master of Science
in the Department of Geological Sciences
in the Graduate School of
The University of Alabama

TUSCALOOSA, ALABAMA

2014

Copyright Joel Arthur Legg 2014
ALL RIGHTS RESERVED

ABSTRACT

The Neal shale, the organic-rich interval of the Floyd Shale located in the Black Warrior Basin of Alabama and Mississippi, has attracted recent attention as a potential economic source of hydrocarbons. X-ray diffraction (XRD) and X-ray fluorescence (XRF) spectroscopic analysis of 54 Neal shale samples indicate the formation is clay-rich and quartz-poor, with the clay content averaging 47.2 wt% and the quartz content averaging 25.2 wt%.

Total organic carbon (TOC) values averaged 2.27 wt%, based on the correlation of XRF trace element concentrations to pyrolysis data. Nine samples of the Neal shale, representing 3 different levels of thermal maturity, were analyzed by FIB-FESEM to determine if organic porosity increases with thermal maturation. Based on this analysis, Neal shale porosity is a mixture of fissure, organophillic, and interparticle porosity. However, no increase in organic matter porosity was observed with increasing thermal maturation. Instead, the organophillic porosity development was found to be linked to bitumen migration/maturation. This suggests organic porosity development was significantly affected by the organic matter composition, rather than by thermal maturity alone (Figure 8). Kinetic porosity modeling indicates the formation developed as much as 4.82% kerogen porosity. However, kinetic porosity models like the one used in this study may not be valid because they do not account for the chemical composition of the organic matter (i.e., kerogen vs. bitumen). Basin modeling indicates that the Neal shale has a large resource potential, with an adsorbed gas estimate of 460 Tcf and recoverable free gas estimates ranging from 227–4,943 Bcf.

Uniaxial strength tests indicate Neal shale samples have an average unconfined axial strength of 3.42 MPa, and the underlying Lewis Limestone samples have an average unconfined diametral strength of 22.22 MPa. This suggests that the underlying Lewis Limestone should serve as an active barrier to hydraulic fracturing efforts within the Neal shale. Although the Neal shale has retained a large volume of natural gas, mapping of the limestone fracture barriers and additional testing of hydraulic fracturing mechanics on clay-rich formations will be necessary before the potential development of the Neal shale as an unconventional petroleum reservoir can be fully evaluated.

DEDICATION

I would like to dedicate this work to my father who taught me the value of hard work and what it takes to succeed.

LIST OF ABBREVIATIONS AND SYMBOLS

ASTM	American Standard for Testing and Materials
Bcf	Billion Cubic Feet
BSE	Back-Scattered Electron
C _C	Convertible Carbon
C _R	Residual Carbon
EDS	Energy Dispersive Spectroscopy
FESEM	Field Emission Scanning Electron Microscope
FIB	Focused Ion Beam
FIB-FESEM	Focused Ion Beam coupled with a Field Emission Scanning Electron Microscope
ft	Feet
HI	Hydrogen Index
HI _o	Original Hydrogen Index
HI _{pd}	Present Day Hydrogen Index
km	Kilometer
MMbo	Million Barrels of Oil
MPa	Mega-Pascal

nm	Nanometer
OI	Oxygen Index
PI	Production Index
PI _o	Original Production Index
PI _{pd}	Present Day Production Index
r	Correlation Coefficient
R ²	Coefficient of Determination
RhoK	Kerogen Density
RhoB	Bulk Density
R _o	Vitrinite Reflectance in Oil
SE	Secondary Electron
SEM	Scanning Electron Microscope
Tcf	Trillion Cubic Feet
TOC	Total Organic Carbon
TOC _o	Original Total Organic Carbon
TOC _{pd}	Present Day Total Organic Carbon
TR	Transformation Ratio

TR _{HI}	Transformation Ratio based on the Hydrogen Index
TTI	Time Temperature Index
wt%	Weight Percent
XRD	X-ray Diffraction diffractometer/diffraction
XRF	X-ray Florescence spectrometer/spectrometry

ACKNOWLEDGMENTS

I would like to thank my thesis committee, Dr. Rona Donahoe, Dr. Jack Pashin, Dr. Andrew Goodliffe, and Dr. Yuehan Lu for their guidance and assistance during the process of conducting this study. I would also like to thank Rich Martens for all of his help and guidance in the FIB-FESEM work. If not for his knowledge and expertise, that aspect of this study would not have been accomplished. In addition, I would like to thank Marcella McIntyre and Tony Smithson for sharing their technical expertise with me.

Finally I would like to thank my wife, Amy, for always being there and supporting me through this long journey. I cherish the love and support you have shown me through this time.

CONTENTS

ABSTRACT	ii
DEDICATION	iv
LIST OF ABBREVIATIONS AND SYMBOLS	v
ACKNOWLEDGMENTS	viii
LIST OF TABLES	xi
LIST OF FIGURES	xii
1 INTRODUCTION	1
1.1 Background	1
1.2 Motivation	9
2 METHODS	10
2.1 XRD and XRF Sample Crushing	11
2.2 XRD Analysis	12
2.3 XRF	14
2.4 Strength Test	14
2.5 FESEM	15
2.5.1 FESEM Sample Preparation	16
2.5.2 FESEM Analysis	17
2.5.3 FESEM 3-D Image Reconstruction	18
2.6 Modeling	19
2.6.1 Kinetic Porosity Modeling	20

2.6.2	<i>Basin Modeling</i>	22
2.7	Volumetric Analysis	23
3	RESULTS	24
3.1	XRD Results	24
3.2	XRF Results	25
3.3	Strength Test Results	29
3.4	FESEM Results	30
3.5	Modeling Results	35
3.5.1	<i>Kinetic Porosity</i>	35
3.5.2	<i>Basin Modeling</i>	36
4	DISCUSSION	47
4.1	Mineralogy	47
4.2	Strength Test	49
4.3	Organic Porosity	50
4.4	Volumetric Analysis	53
5	CONCLUSIONS	55
	REFERENCES	56
	APPENDIX	60

LIST OF TABLES

Table 1. Comparison of TOC values estimated from XRF Cr+Mo+Ni concentration with measured TOC values from Pashin et al. (2011)	28
Table 2. Results of FESEM 3-D reconstruction analysis of Neal shale samples, reported in volume percent	35
Table 3. Table of calculated kerogen porosity including input data	36
Table 4. Recoverable free gas estimates and adsorbed gas-in-place based on risk analysis and basin modeling	53
Table A-1. Geochemical Data for the Neal shale	60
Table A-2. XRD results for Well 2191 samples	61
Table A-3. XRD results for Well 1780 samples	62
Table A-4. XRD results for Well 15668 samples	63
Table A-5. XRF results for Well 2191 samples	64
Table A-6. XRF results for Well 1780 samples	66
Table A-7. XRF results for Well 15668 samples	68
Table A-8. XRF trace element data for samples from Well 2191	69
Table A-9. XRF trace element data for samples from Well 1780	71
Table A-10. XRF trace element data for samples from Well 15668	72
Table A-11. Uniaxial strength test results for Well 15668 core samples.....	73
Table A-12. TerraTek [®] XRD analysis of Well 15668 for the Geological Survey of Alabama study by Pashin et al. (2011)	75

LIST OF FIGURES

Figure 1. Isopach map of the Neal shale of the Black Warrior Basin	3
Figure 2. Location of the Black Warrior Basin in relation to tectonics, including the three counties in Alabama where the wells used in this study are located	6
Figure 3. Regional cross-section showing the facies relationships in Devonian-Mississippian strata of the Black Warrior Basin	8
Figure 4. Sample 9044.0 from Well 15668 showing the ridge necessary to rapidly find the coincidence point of the FIB-FESEM	16
Figure 5. Sample 9044.0 from Well 15668 showing the trench milled on both sides of the area of interest and the flattened top	18
Figure 6. Graph of TOC values obtained by pyrolysis (Pashin et al., 2011) vs. Cr+Mo+Ni concentrations, determined for the Neal shale samples by XRF analysis	27
Figure 7. EDS maps of Neal shale 2920-25 ft sample showing the location of organic matter (blue arrow) and a pyrite framboid (red arrow)	32
Figure 8. Image of Neal shale 3000-05 ft sample collected using the BSE detector (left) and the SE detector (right)	33
Figure 9. 3-D models of Neal Floyd 3000-05 ft sample showing the reconstructed sample using A) the BSE detector, B) the SE detector, C) reconstructed organic matter, D) porosity, and E) pyrite with the scale bar in micrometers	34
Figure 10. Easy %R _o values for Well 2191	37
Figure 11. Easy %R _o values for Well 1780	38
Figure 12. Easy %R _o values for Well 15668	39
Figure 13. Burial history of Well 2191, including Easy %R _o values as an overlay	40
Figure 14. Burial history of Well 1780, including Easy %R _o values as an overlay	41

Figure 15. Burial history of Well 15668, including Easy %R _o values as an overlay	42
Figure 16. Transformation ratio of the kerogen within the Neal shale	43
Figure 17. Burial history of Well 2191 with overlain hydrocarbon zones	44
Figure 18. Burial history of Well 1780 with overlain hydrocarbon zones	45
Figure 19. Burial history of Well 15668 with overlain hydrocarbon zones	46
Figure A-1. Correlation coefficient matrix for the Neal shale	76
Figure A-2. Correlation coefficient matrix for the Lewis Limestone	77

1 INTRODUCTION

For each potential shale play, a comprehensive petrologic analysis needs to be performed to fully understand the degree to which porosity, hydrocarbon content, and mineralogy vary, so that production can be maximized. If the shale unit is thoroughly characterized, informed decisions can be made about the drilling and completion technologies to be used in developing the reservoir. Successful evaluation of the potential economic viability of the Neal shale includes verifying the amount of gas-in-place, the mineralogy, and the pressure of the formation (Pashin, 2008). By analyzing the development of nanoporosity within organic matter as a function of thermal maturation, its contribution to the total porosity of the Neal shale can be determined. Analyzing the mineralogy of the formation allows for sweet-spot identification for landing laterals and designing completion programs. If the Neal shale has generated and maintained sufficient volumes of hydrocarbons and the mineralogy is suitable for hydraulic fracturing, production of this resource could assist in the U.S. goal of energy independence. In addition, results from this study will assist in understanding the development of organic porosity and thus enable better modeling for other shale plays.

1.1 Background

The Neal shale has been identified as a potential unconventional hydrocarbon reservoir within the Black Warrior Basin of Alabama and Mississippi (Pashin et al., 2011). The Neal shale is an informal term for the organic-rich interval of the Floyd Shale and ranges in thickness from less than 25 feet to 350 feet in Alabama (Figure 1). This zone may be a viable target for economic hydrocarbon production (Pashin et al., 2011). Petroleum exploration companies have had limited success using vertical wells within the Neal shale; horizontal wells will likely be

necessary for economic production, due to the limited thickness of the unit (Pashin, 2008). To date, companies targeting the organic-rich shale have drilled near faults; however, wells that have been drilled near faults in the stratigraphically equivalent Barnett Shale of the Fort Worth Basin have resulted in low returns, compared to those of other areas (Bowker, 2003). This is due to the presence of macro-fractures that are filled with carbonate cement which make the shale less responsive to stimulation efforts (Bowker, 2003). In addition, low returns near fault zones may be caused by diversion of the hydraulic fracture fluid along these preexisting pathways thus diverting energy away from the target formation.

Carroll et al. (1995) studied the burial history and source rock characteristics of the Neal shale, based on measured mean-maximum vitrinite reflectance in oil values (R_o). From this information, time temperature index (TTI) values were calculated using Lopatin's method to determine the petroleum generation history of the Neal shale. An average geothermal gradient of 16°F/1000 ft (-8.9°C/304.8 m) was used in the TTI calculations. Lopatin's TTI method (Lopatin, 1971) was originally calibrated based on Type III kerogen and only takes into account the temperature at depth and amount of time the formation of interest was buried. This model does not suffice for the Neal shale, which is dominated by Type II kerogen (Carroll et al., 1995; Pashin et al., 2011) and has a complex tectonic history. Kinetic modeling of the chemical reactions that took place over time, as incorporated into Petromod[®] software, can be used to model the timing and volume of hydrocarbons generated from the formation. In addition, Petromod[®] calculates Easy % R_o values using the Sweeney and Burnham (1990) method which allows for correlation to measured R_o values. The Sweeney and Burnham (1990) method of calculating R_o is based on running 20 parallel first-order Arrhenius chemical reactions which control vitrinite maturation.

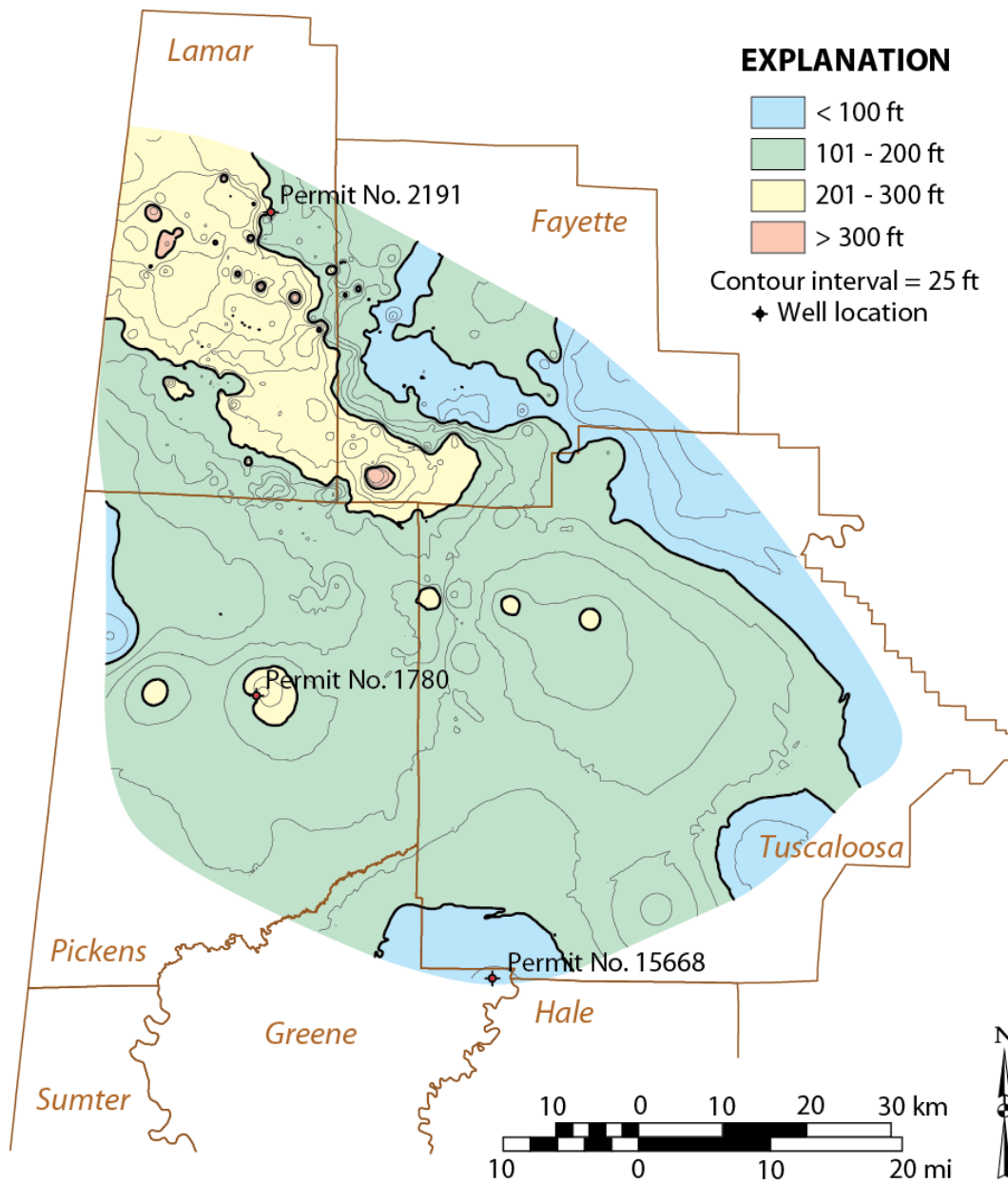


Figure 1: Isopach map of the Neal shale of the Black Warrior Basin (modified from Pashin et al., 2011).

The use of scanning electron microscopy (SEM) has led to better understanding of organic porosity development. The relationship of organic porosity to thermal maturity has been studied by Curtis et al. (2010, 2011, 2012, and 2013), Sondergeld et al. (2010), Modica and

Lapierre (2012), Bernard et al. (2012), and Ambrose et al. (2012), amongst others. Some of these studies have shown an increase in porosity with thermal maturation, but the mathematical nature of that relationship is undetermined. In addition, Curtis et al. (2012) showed that porosity development may not be linked to thermal maturity alone, but may also be related to the chemical makeup of the macerals.

A kinetic model of porosity development may be employed without the use of SEM. A kinetic model for assessing kerogen porosity was developed by Modica and Lapierre (2012). Their model utilizes geochemical data collected through pyrolysis studies to determine kerogen porosity. The mathematical model uses the original amount of total organic carbon (TOC_o), the present day TOC (TOC_{pd}), the labile portion of TOC termed 'convertible carbon' (Cc), the transformation ratio (TR), and the density of both kerogen ($RhoK$) and the inorganic matrix ($RhoB$). However, this model may not be adequate for all systems, based on a study by Curtis et al. (2012) that found that separate pieces of organic matter at the same level of maturity did not have the same proportion of porosity development.

In the Barnett Shale of Texas, mineralogy may be the deciding factor controlling the best well locations (Bowker, 2003). The best production in the Barnett Shale occurs where the shale contains more than 45 weight percent (wt%) quartz and less than 27 wt% clay (Bowker, 2003). This is due to the higher quartz content making the formation sufficiently brittle to fracture, thus allowing a linkage between the wellbore and shale micro-porosity.

The mechanisms controlling the quality of the source rock depend on tectonics, stratigraphy and sedimentation, burial history, and other geologic processes (McCarthy et al., 2011; Pashin et al., 2011). Because of this, a brief overview of these facets as they pertain to the

deposition and organic richness of the Neal shale will allow a more in-depth interpretation of the study results.

The Black Warrior Basin is a Paleozoic foreland basin that formed due to extensional and compressional tectonic settings (Pashin et al., 2011). The Paleozoic basin formed adjacent to the intersection of the Appalachian and Ouachita orogenic belts (Thomas et al., 1977, 1988; Pashin et al., 2011), and includes a triangular area in northwestern Alabama and northeastern Mississippi. The Basin is bordered on the southeast by the Appalachian Orogeny, on the southwest by the Ouachita Orogeny, and on the north by the Nashville Dome (Figure 2) (Carroll et al., 1995). The Basin is mainly a Ouachita foreland basin; Appalachian thrust and sediment loads did not deposit on the southeastern portion of the Basin until the Early Pennsylvanian (Pashin, 2004).

The tectonic history of the Black Warrior Basin can be summarized by 6 stages, according to Thomas (1988):

- 1) Late Precambrian – Early Cambrian: Iapetan rifting with the associated deposition of muddy, calcareous clastic sediment;
- 2) Middle Cambrian – Mississippian: development of a passive continental margin with deposition of shallow-water carbonates;
- 3) Late Mississippian: initial Ouachita orogenesis with deposition of a mixed carbonate-siliciclastic succession;
- 4) Early – Late Pennsylvanian: maximum basin subsidence associated with the Appalachian-Ouachita orogenesis (Pashin, 1994) and deposition of synorogenic sediment; progradation of thick, coal-bearing siliciclastic successions from source areas in the Appalachian-Ouachita orogen.

- 5) Late Pennsylvanian – Early Mesozoic: uplift resulting in Permian-Cretaceous erosion and non-deposition (Telle et al., 1987);
- 6) Mesozoic: transgressive marine sediments of the Mississippi embayment overlapped the passive margin-shelf.

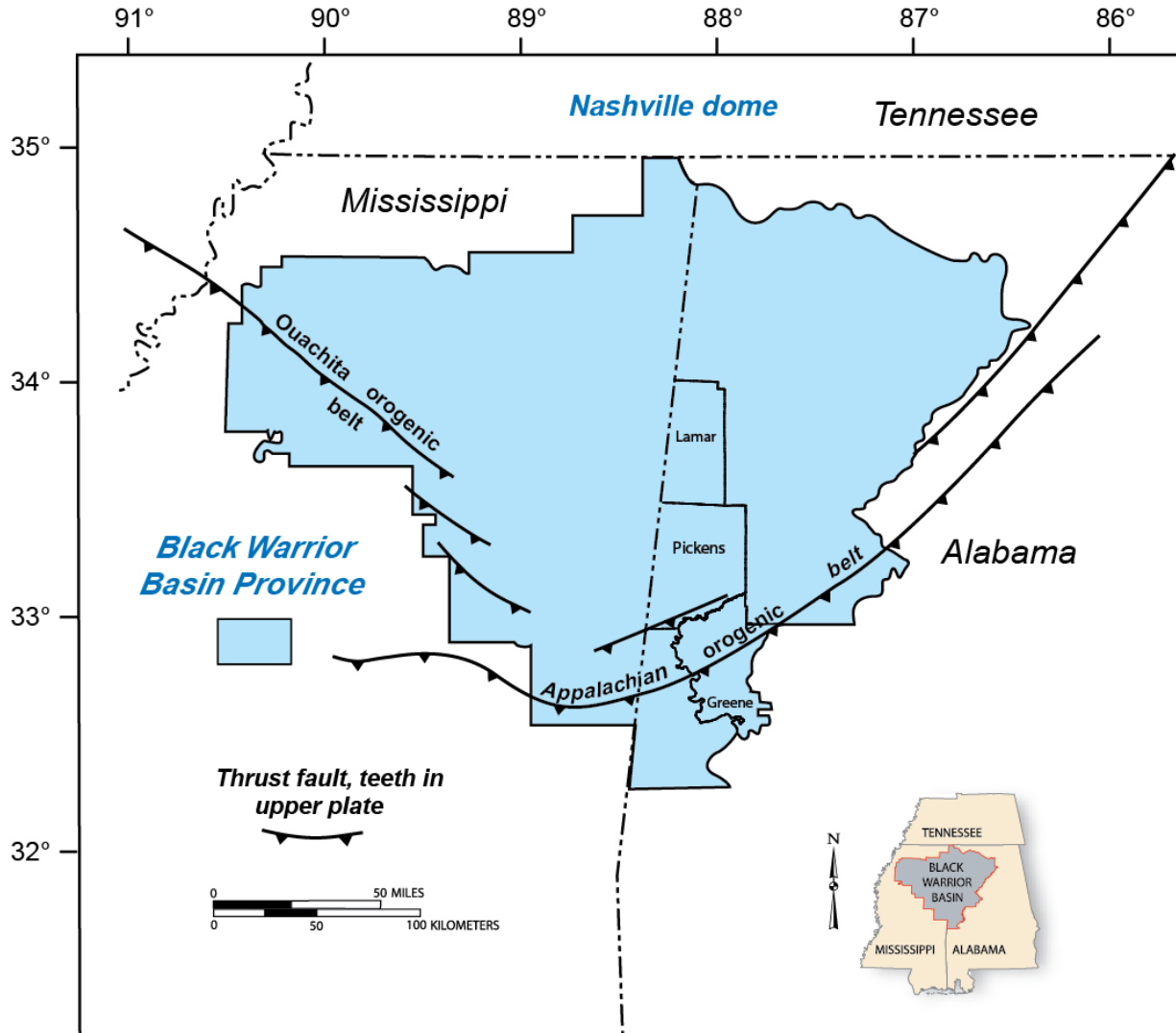


Figure 2: Location of the Black Warrior Basin in relation to tectonics, including the three counties in Alabama where the wells used in this study are located (modified from Pawlewicz and Hatch, 2007)

The Black Warrior Basin is a structural homocline that dips southwest toward the Ouachita Orogen and is broken by extensional faults, which show multiphase tectonic development that spanned the Paleozoic Era (Thomas, 1988; Groshong et al., 2010; Pashin et al., 2011). The geologic structure of the Black Warrior Basin affects the geometry, continuity, and permeability of shale reservoirs (Pashin et al., 2011). Faults within the Basin pose a significant risk for leak-off of stimulation fluid during hydraulic fracturing (Pashin et al., 2011) that would hinder fracture stimulation efforts. Thus, care must be taken to avoid drilling near fault zones.

The Neal shale was deposited as part of the Chester Group Floyd Shale in the Black Warrior Basin during the Upper Mississippian Period. The Neal shale, the object of recent shale gas exploration, is the organic-rich interval of the clastic wedge that deposited at the toe of the ramp (Figure 3). The formation sediment was transported towards the southeast along depositional strike of the Warrior platform, and deposited in epeiric ramp and basinal environments during the Late Mississippian. The Neal shale is in a complex facies relationship with strata of the Pride Mountain Formation, Hartselle Sandstone, Bangor Limestone, and lower Parkwood Formation (Pashin, 2008) with the majority of the Neal shale being equivalent to the Bangor Limestone. Individual parasequences thin towards the southwest and define a clinoformal stratal geometry in which near-shore facies of the Pride Mountain-Bangor interval pass into condensed, starved-basin facies of the Neal shale (Pashin, 2008). Overlying Pottsville sediments had a principal source to the southeast of the Black Warrior Basin and represents the thick clastic wedge shed from the Appalachian orogenic belt (Pashin and Raymond, 2004). Pottsville deposition caused the foreland basin to rapidly subside during the Pennsylvanian-Early Permian (Cleaves and Broussard, 1980).

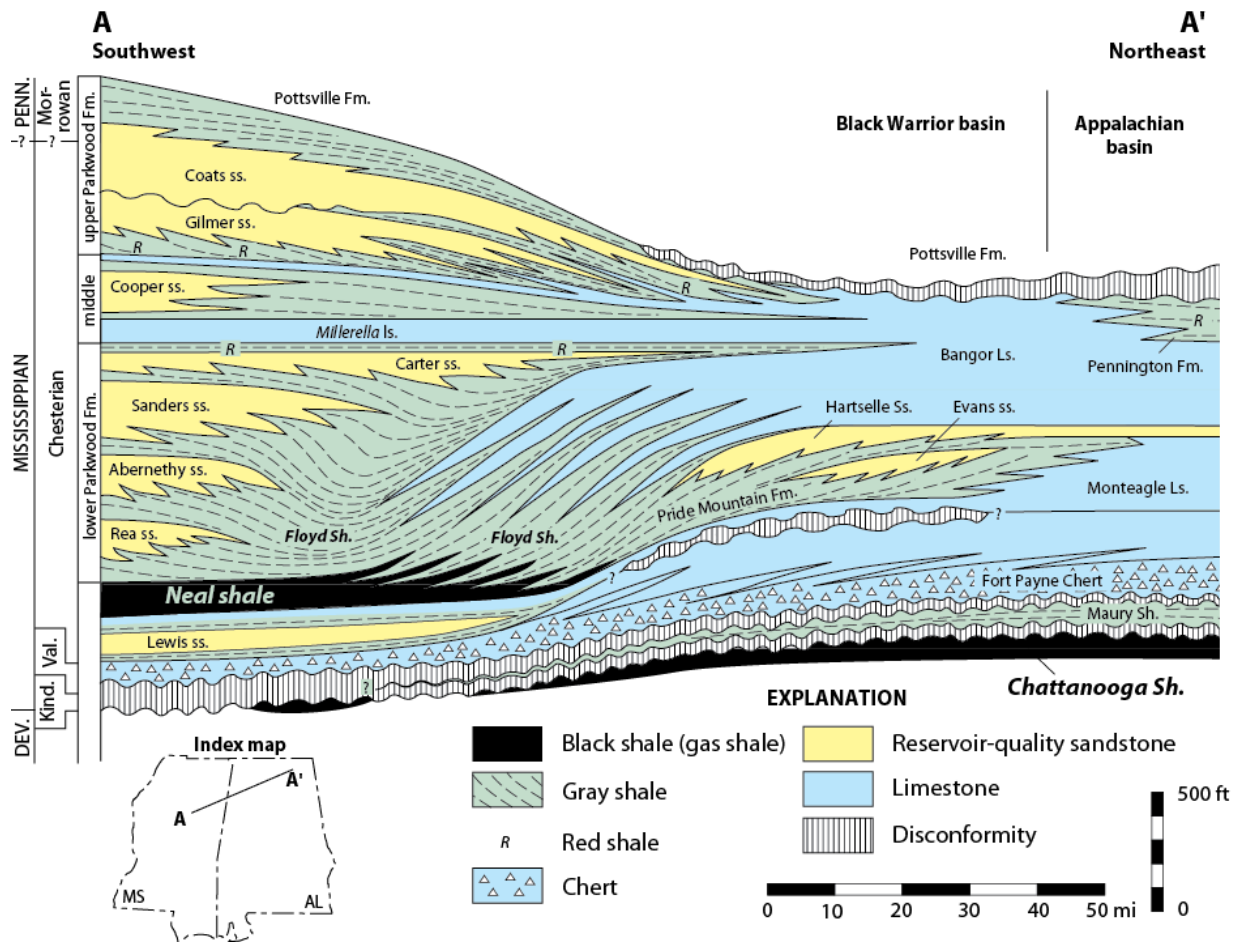


Figure 3: Regional cross-section showing the facies relationships in Devonian-Mississippian strata of the Black Warrior Basin (from Pashin et al., 2011)

The Neal shale is an organic-rich silty, calcareous, laminated to thick-bedded shale formation that was deposited in slope and epeiric basin floor environments (Pashin et al., 2011). Processes occurring within the basin were varied and influenced by the development of carbonate ramps, siliciclastic coastal plains and marine shelves (Pashin et al., 2011). Deposition of the Neal shale was highly dynamic, reflecting changing redox conditions, variable sediment and nutrient flux, and reworking by storms, which resulted in heterogeneous facies and reservoir quality (Pashin et al., 2011). The Neal shale also contains thin interbeds of limestone and siltstone, that are wavy or lenticular and contain ripple cross-laminae (Pashin et al., 2011).

These interbeds are more abundant to the northwest where the Neal shale transitions to the Bangor Limestone. Pyrite framboids within the formation range in size from 3-10 μm and are related to the amount of oxygen within the water column (Pashin et al., 2011). From this data it was suggested that the Neal shale deposited in an exaerobic or dysaerobic environment.

The organic content of the Neal shale is dominated by amorphous Type II marine kerogen (Carroll et al., 1995). Based on visual inspection of the kerogen from whole-rock polished pellets, Carroll et al. (1995) determined that the Neal shale is dominated by matrix bituminite. This maceral type has been attributed to degraded marine sources, but the Neal shale organic matter is also mixed with varying amounts of terrestrial plant material. When the calculated hydrogen index (HI) values were plotted against the oxygen index (OI) values, the organic matter plotted as a Type III kerogen, which was attributed to reduced HI values by thermal maturation (Carroll et al., 1995).

1.2 Motivation

An assessment of the petroleum generation potential of the Neal shale was conducted to determine if the formation is a suitable unconventional reservoir. An analysis of porosity in the Neal shale was conducted on samples with Easy % R_o ranging from 0.9– 2.3%. The validity of the Modica and Lapierre (2012) model was tested by analyzing organic porosity development of the Neal shale, which is dominated by a single kerogen type, at varying thermal maturities using focused ion beam milling coupled with a field emission scanning electron microscope (FIB-FESEM). The Neal shale mineralogy has been characterized by X-ray diffraction (Pashin et al., 2011) but not at the sampling resolution used in this study. By analyzing the mineralogy every 10 ft, zones with suitable mineralogy may be targeted for hydraulic fracturing.

2 METHODS

FIB-FESEM was used to analyze the development of organic porosity as a function of thermal maturation using samples of the Neal shale selected from cores/cuttings of three wells located in Alabama (Figure 1). Cuttings from Wells 2191 and 1780 were collected at 5-ft intervals and 10-ft intervals respectively during the drilling process. These cuttings samples will thus be referred to by their sample depth range. These samples were obtained from the sample collection of the Geological Survey of Alabama. The wells chosen for this study are the Gilmer 17-12 #1 well (permit number 2191) located in Lamar County, the Ralph W. Holliman #13-16 well (permit number 1780) located in Pickens County, and the Lamb 1-3 No.1 well (permit number 15668) located in Greene County, Alabama. These wells will subsequently be identified by their permit number (e.g., Well 15668). A total of 54 samples of the Neal Shale, 6 samples of the Floyd Shale, and 4 samples of the Lewis Limestone were obtained from the core collection of the Geological Survey of Alabama. Only rock cuttings were available from Wells 2191 and 1780 (sampled at 10-ft intervals). Hereafter, the cuttings samples will be referred to by their sample depth range (e.g., 2740-45 ft). While drilling Well 15668, a 25 ft core of the Neal shale was collected. The core was sampled approximately every 10 ft to correlate with the cuttings sampled from the other two wells. Within Wells 2191 and 1780, measured vitrinite reflectance values ranged from 0.92– 0.98% and 1.44– 1.59%, respectively, according to data previously published by Carroll et al. (1995). Within Well 15668, calculated Easy %R_o values ranged from 2.2– 2.3%.

X-ray Diffraction (XRD) and X-ray Fluorescence (XRF) analyses of all 64 core/cuttings samples were completed in an effort to predict how mineralogy may affect development of this resource. A limited number of unconfined uniaxial strength tests for samples collected from the

Well 15668 core were conducted to evaluate whether the Neal shale mineralogy would be suitable for hydraulic fracturing. The diametral strength of core samples taken at five depths containing the Neal shale was compared to that of the underlying Lewis Limestone.

Geochemical data previously collected in a study performed by the Geological Survey of Alabama (Pashin et al., 2011), were utilized to calculate kerogen porosity development in the Neal shale with Modica and Lapierre's (2012) kinetic model. This calculated porosity was compared to physical porosity measurements made using the FIB-FESEM to evaluate how well the kinetic model works. The geochemical data utilized in the kinetic porosity model include TOC, kerogen type, and the HI for different parts of the Neal shale. Measured porosity values were used in conjunction with basin modeling to predict the type and volume of hydrocarbons that have been generated and stored within the Neal shale. The methods used in this study are described in detail, below.

2.1 XRD and XRF Sample Crushing

XRD and XRF analyses required the 64 samples of rock core and cuttings obtained from the Geological Survey of Alabama to be milled to less than 230 mesh. To crush each sample, approximately 50 grams of core or chips were added to a SPEX low-C, ring and puck hardened steel mill and milled for one minute. The pulverized sample was then poured into a clean, labeled, plastic container. The mill was cleaned between samples by milling pure quartz for one minute, discarding the pulverized sand, followed by rinsing with isopropanol. The steel mill is relatively soft and will contaminate the sample with iron and a minor amount of chromium and manganese. However, the amount of iron contamination is on the order of ppm, and thus should

not have a major effect on XRF results. The crushed samples were subjected to XRD and XRF analyses.

2.2 XRD Analysis

XRD analysis of 54 Neal shale samples was conducted to determine how the mineralogy varies within the formation and to estimate the brittleness of the formation. Because shale brittleness is related to mineralogy, analysis of the mineralogical variation of the Neal shale is crucial. Rock brittleness is a key factor determining whether an effective hydraulic fracture network capable of accessing economic reservoir volume can be developed (Bowker, 2003). It has been found that brittle failure suitable for hydraulic fracturing occurs in zones with highly siliceous shale intervals (Bowker, 2003). This has been observed in both the Barnett Shale and Haynesville Shale, where hydraulically fractured zones with quartz contents greater than 45 wt% have shown greater production than wells completed in clay-rich zones (Jarvie et al., 2007).

To analyze the mineralogy of the Neal shale, a random bulk mount and an oriented clay mount were prepared for each sample. The oriented clay mount allowed for the concentration and identification of clays by removing a large percentage of the higher density minerals. In addition, the oriented mount allows clay particles to settle through water during filtration in their preferred orientation so a higher intensity basal peak occurs in the diffraction pattern. To make an oriented clay mount, 2–10 grams of crushed rock were placed into a 500 ml beaker with approximately 400 ml of water. The sample was vigorously stirred for 2–3 minutes and then placed on the sonicator for 30 seconds to completely suspend the sediment. Next, the sample was left to settle for 30 minutes to 2 hours to allow the particles with greater density to drop out of suspension, according to Stokes Law. The upper 150 ml of liquid was filtered through a 0.45

μm nylon filter membrane, the sample transferred from the membrane to a glass slide, and then allowed to dry for several hours before analysis by XRD.

The XRD bulk sample mounts and oriented clay mounts were analyzed using a Bruker D8 Advance Diffractometer. A total of 128 samples (64 bulk mounts and 64 clay mounts) were run at 45 kV, 40 mA, and 0.9876° $2\text{-}\theta$ per minute, from $5\text{--}70^\circ$ $2\text{-}\theta$. The diffraction patterns were analyzed using Bruker's EVA software and EDA search software for peak identification. Once the diffraction peaks were identified for the clay mount and the bulk mount patterns, the interpreted mineral content was estimated using the Rietveld method (Reitveld, 1969).

For the Rietveld analysis, the generalized crystal structures included in the TOPAS Structure Database that corresponded to the interpreted minerals were used, which accounted for the preferred orientation of minerals before the quantitative analysis. In addition, instrument parameters were included to correct for varying effects caused by the machine in order to improve the Rietveld pattern fitting. For background correction, the $1/X$ background function, which is a hyperbola, was used to account for the observed increasing background level at low $2\text{-}\theta$ angles caused by air scattering of the primary X-ray beam. Sample displacement was accounted for by shifting the pattern to align the quartz peaks in EVA and recording the $2\text{-}\theta$ displacement in TOPAS. Finally, polarization effects from the secondary graphite monochromator were accounted for by changing the monochromator angle to 26.37° $2\text{-}\theta$ (DIFFRACplus, 2005).

The Rietveld refinement program, TOPAS, may have difficulty in distinguishing between illite and muscovite because the two minerals have similar structures and XRD patterns. Although muscovite is not a clay, it was included as part of the clay fraction for the purposes of this study. This same methodology was used by TerraTek[®] and allowed for a comparison

between studies in regards to bulk mineralogy. Because of the structure similarity, at depths where the illite concentrations fall below detection and the muscovite concentrations rise to greater than 25 wt%, it was assumed that the computer program was unable to distinguish between the two minerals. Therefore, under these conditions, the calculated percentage of muscovite would represent a sum of both minerals, rather than muscovite alone. Even though distinguishing between the two minerals is difficult, the overall analysis will not be affected because only the total sum of all clays present is of interest in this study.

2.3 XRF

The chemical composition of the Neal shale was analyzed using a Philips PW2400 X-ray Fluorescence Spectrometer. To verify that there were no instrumental errors, the accuracy of the instrument was checked by running several standards. The instrument also runs a single standard several times per week to adjust for the instrument condition and/or aging of the X-ray tube. The software application used was TraceEl40, which is set up to run 40mm pressed pellets for trace element identification with minimal error in major element percentages. This allowed for a comparison of the XRF data to the mineralogy and TOC of the Neal shale formation. To make the pressed pellets for XRF analysis, 15 drops of polyvinyl alcohol were mixed with approximately 15 cm³ of powdered sample, the mixture was transferred to a 40mm aluminum cup and pressed for 5 minutes at 40,000 psi.

2.4 Strength Test

A strength test was conducted to compare the strength of the Neal shale to that of the underlying Lewis Limestone. A uniaxial compressive point load test was conducted on the

unconfined samples according to the American Standard for Testing and Materials (ASTM) D7012–13 protocol. This test is used as an index test for the strength of rock specimens. The equipment used for this test was the PLT-10 designed by Structural Behavior Engineering Laboratories, Inc. This setup used the Enerpac C 102 hydraulic piston assembly with a maximum compressive pressure of 10,000 psi. For diametral tests, the rock core was loaded into the apparatus with the bedding plane parallel to the contact points. Because the shale samples were highly fissile, the core size specifications may not have conformed to the testing procedures recommendation. For axial tests, the sample bedding plane was loaded perpendicular to the platens. Once the sample was mounted, the load was steadily increased so that failure would occur between 10 and 60 seconds, as specified by the protocol. For the irregular lump of shale tested, the bedding plane was oriented parallel to the platens with the smallest dimension of the sample resting between the contact points.

2.5 FESEM

Structures within shale can be resolved on the nanometer scale using focused ion beam (FIB) coupled to a field emission scanning electron microscope (FESEM). The FIB-FESEM technique allowed the analysis of organic porosity development in relation to thermal maturation. Once the samples were prepared, images were collected overnight with a TESCAN LYRA FIB-FESEM, using the secondary electron (SE) detector, the back-scattered electron (BSE) detector, or both, depending on the conditions under which the images were collected. The SE detector provides a high-resolution image because the detector collects low-energy secondary electrons that originate within a few nanometers of the sample surface, while the BSE detector allows for better image contrast due to high-energy electrons being back-scattered by

elastic scattering interactions with specimen atoms (Goldstein et al., 2003). The higher the atomic number of the element, the brighter the sample will appear (Goldstein et al., 2003). The SE detector was useful for the organic porosity analysis, while the BSE was useful in mapping dense minerals, organic material, and inorganic minerals due to better density contrast. Because of the pros and cons offered by each detector, a combination of the SE and BSE was used to analyze the 3-D network of organic matter, porosity, and pyrite in the shale samples.

2.5.1 FESEM Sample Preparation

Ten samples of the Neal shale representing three levels of thermal maturity, and five samples of the Lewis Limestone, were selected for FIB-FESEM analysis. The samples ranged in size from 1 mm to 10 mm and consisted of broken rock chips and core from Well 2191, Well 1780, and Well 15668. Seven samples from Well 15668 core were collected at 10-ft intervals. Four samples from Well 2191 and four samples from Well 1780 were collected at approximately 100-ft intervals. The samples were cleaned with methanol and mounted to aluminum stubs using carbon paint. Samples were coated with a thin layer of gold to help prevent the sample from charging during argon-ion beam milling and imaging. Initially, samples were mounted with the grains parallel to the aluminum stub but this required that they be tilted 45 degrees for both milling and imaging. Because of this, a large amount of drift occurred while imaging the sample. After this was noted, samples were mounted with the grains perpendicular to the aluminum stub. Samples displaying a ridge were chosen in order to rapidly find the coincidence point of the FIB and FESEM (Figure 4). Once this point was found, a trench was milled on both sides of the sample to ensure that the milled material would not be re-deposited during the milling process (Figure 5). The top of the sample was smoothed so the FIB would begin each

sequential mill at the same position. In addition, a fiducial mark was milled into the trench on the left side of the sample so the 2-D images could be realigned.

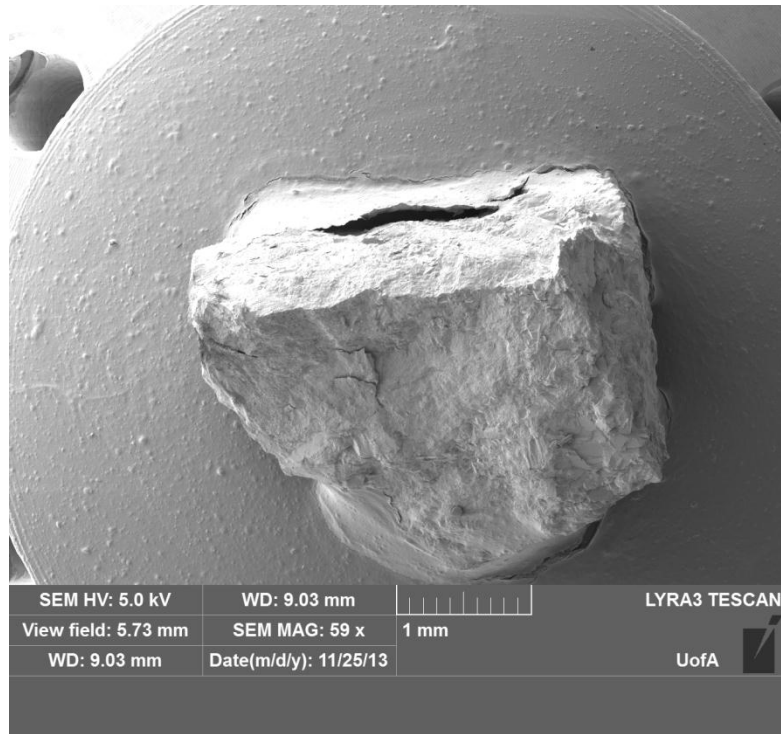


Figure 4: Sample 9044.0 from Well 15668 showing the ridge necessary to rapidly find the coincidence point of the FIB-FESEM.

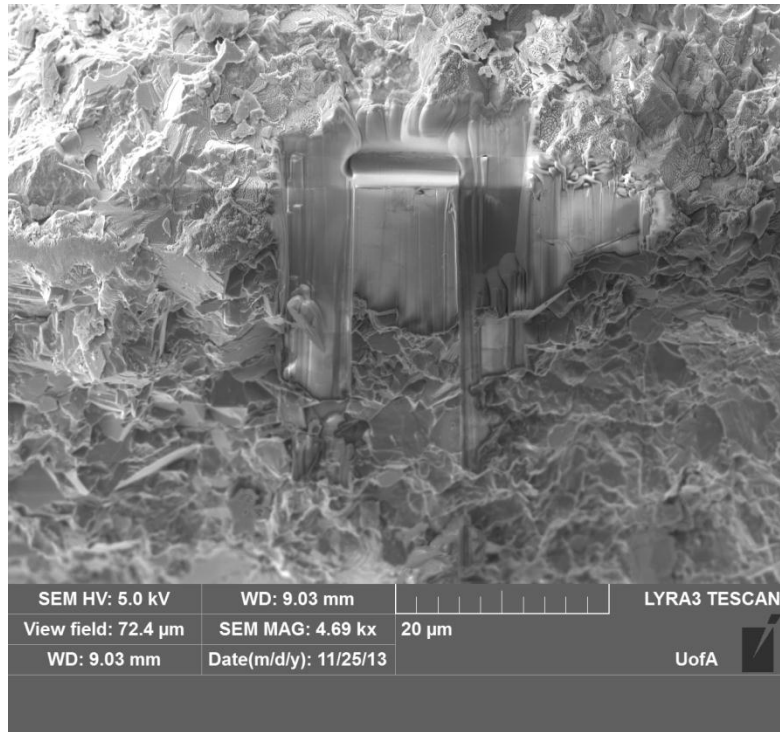


Figure 5: Sample 9044.0 from Well 15668 showing the trench milled on both sides of the area of interest and the flattened top.

2.5.2 FESEM Analysis

After a section of the sample was prepared for the sequential milling and imaging, samples were scanned for 8–12 hours. The size of the area imaged depended on the size of the cube left after trenching around the sample, with the goal being $5 \times 5 \times 5 \mu\text{m}$. Depending on the size of the cube, 300–500 2-D images were collected sequentially, after exposing new layers by milling away a 15nm slice between scans. The 15 nm slice thickness did not restrict the analysis of void space because pores as small as 30nm were resolved in 2-D space and thus could be seen in 3-D space. Samples were milled 2 micrometers further than the bottom of the sample to remove all material and prevent re-deposition at the bottom of the imaged sample. The resolution of the images collected was set at 8–10 nanometers (nm) per pixel to obtain a sufficiently high-resolution image for analysis.

2.5.3 FESEM 3-D Image Reconstruction

The 2-D images collected during the milling and imaging process were used to reconstruct the sample in 3-D using the software program ImageJ. 2-D images were imported into ImageJ and converted to a stack. The 2-D images were then aligned to a fiducial mark on the sample. The area of interest within the composite image was cropped and saved for future work. A threshold of the image gray-scale was set to identify the feature of interest and analyzed using the particle analyzer that is built into ImageJ. A mask of the threshold values and a summary of the particles were saved for further analysis. To create a 3-D structure of the feature of interest from the binary image, the white background had to be shaded black by setting a threshold value for the background and creating a mask. Once this was completed, the image could be viewed using the 3-D viewer in order to map the feature of interest. For this study, porosity was displayed as green, organic material is shown in red, and pyrite is yellow.

2.6 Modeling

Kinetic models of organic matter porosity development enable rapid analysis of porosity development in a given region. However, the validity of such a model must be tested to ensure that calculated and measured results agree. With validation, the model could be used across an entire basin with reasonable confidence to identify sweet spots for drilling. If the model results disagree with the measured data, then the model should not be used and an investigation would need to be undertaken to determine reasons for the disagreement. In addition to kinetic modeling of organic porosity development, basin modeling allows for more complete understanding of thermal maturation of the source rock kerogen, as well as an analysis of the type and volume of hydrocarbons generated.

2.6.1 Kinetic Porosity

Modica and Lapierre's (2012) kinetic model of kerogen porosity development was tested to determine if it is applicable to the Neal shale of the Black Warrior Basin. Pyrolysis data showing the present day conditions of the Neal shale, compiled by Pashin et al. (2011), (Table A-1) were utilized in organic porosity calculations. Input values necessary for Modica and Lapierre's method, were determined using an alternative method described by Jarvie et al. (2007). These calculations were then compared to measurements made by FIB-FESEM to test for model validity.

The kinetic model by Modica and Lapierre (2012) was created to describe porosity development within the Mowry Shale in the Powder River Basin, Wyoming. For their study, the original TOC (TOC_o) was mapped across the basin by correlating the gamma ray logs to TOC measurements. This method was not utilized in this study because using logs for only 3 wells would not be as accurate as calculating TOC_o through the method of Jarvie et al. (2007), which requires first computing the original hydrogen index (HI_o) using equation (1):

$$HI_o = \left(\frac{\% \text{ Type I}}{100} \times 750 \right) + \left(\frac{\% \text{ Type II}}{100} \times 450 \right) + \left(\frac{\% \text{ Type III}}{100} \times 125 \right) + \left(\frac{\% \text{ Type IV}}{100} \times 50 \right). \quad (1)$$

As generated hydrocarbons migrate from the formation, the HI will decrease from its original value, giving an indication of the maturity of the sample. As shown in equation (1), Type I kerogen has an average initial HI of 750, Type II averages 450, Type III averages 125, and Type IV averages 50 (Jarvie et al, 2007).

Once HI_o is determined, the transformation ratio based on the HI (TR_{HI}) can be calculated using equation (2). The transformation ratio (TR) represents the extent to which kerogen has

been converted to hydrocarbons and is based on the decrease in the HI from original values. The hydrogen index transformation ratio (TR_{HI}) is derived from the change in the original hydrogen index (HI_o) to the present day hydrogen index (HI_{pd}) where the original production index (PI_o) = 0.02 and increases to the present day production index (PI_{pd}).

$$TR_{HI} = 1 - \frac{HI_{pd}[1200 - HI_o(1 - PI_o)]}{HI_o[1200 - HI_{pd}(1 - PI_{pd})]} \quad (2)$$

Jarvie et al. (2007) incorporated the formula of Pelet (1985) for computing the TR_{HI} , where 1200 $\mu\text{g g}^{-1}$ is the maximum amount of hydrocarbons that could be generated, assuming 83.33% carbon in hydrocarbons. Once the HI_o , HI_{pd} , TR_{HI} , and TOC_{pd} values are calculated, the original total organic carbon (TOC_o) value can be calculated with equation (3):

$$TOC_o = \frac{HI_{pd} \left(\frac{TOC_{pd}}{1+k} \right) (83.33)}{\left[HI_o(1 - TR_{HI}) \left(83.33 - \left(\frac{TOC_{pd}}{1+k} \right) \right) \right] - \left[HI_{pd} \left(\frac{TOC_{pd}}{1+k} \right) \right]} \quad (3)$$

where TOC_{pd} represents the present day TOC and k is a correction factor based on residual organic matter being enriched in carbon at higher maturity levels (Jarvie et al., 2007). For a formation like the Neal shale, which is dominated by Type II kerogen, the increase in residual carbon (C_R) at high maturity would be assigned a value of 15%. The correction factor, k , is then: $TR_{HI} \times C_R$.

One additional variable, the portion of organic carbon that can still be converted to hydrocarbons (C_c), must also be calculated using equation (4) before the porosity can be modelled.

$$C_c = \left(\frac{1}{TR}\right) \left(1 - \frac{TOC_{pd}}{TOC_o}\right) \quad (4)$$

Once the values described above are calculated (equations 1–4), the kerogen porosity of the formation can be determined with equation (5):

$$\text{PhiK} = [(TOC_o \times C_c)k]TR_{HI} \left(\frac{\text{RhoB}}{\text{RhoK}}\right), \quad (5)$$

where PhiK represents the kerogen porosity. A dimensionless scaling factor (k) is used to estimate kerogen mass from the C_c mass. The k factor used by Modica and Lapierre was 1.118 and was based on the assumptions that about 95% of the TOC_o is from kerogen and that a C_c mass represents about 85% of a convertible kerogen mass ($k = \frac{0.95}{0.85} \approx 1.118$). The last term $\left(\frac{\text{RhoB}}{\text{RhoK}}\right)$ is a density conversion from weight percent to volume percent, where RhoB is the bulk density of the rock and RhoK is the bulk density of kerogen estimated at 1.2 g/cc (Modica and Lapierre, 2012; Okiongbo et al., 2005). For this study, RhoB was set to 2.553, based on TerraTek's TRA[®] tight rock analysis.

2.6.2 Basin Modeling

A burial history model was run for each well using Petromod[®], which allowed a more complete understanding of the thermal history of the Black Warrior Basin and estimation of the type and volume of hydrocarbons that were generated and stored within the Neal shale. The thickness and depth of the various formations used in the model were selected based on well log analysis and mud log reports. The eroded thickness of the Pottsville formation and the Tuscaloosa Group for Well 2191 and Well 1780 were determined from Carroll et al.'s (1995)

study of the burial history and source-rock characteristics of the Black Warrior Basin in Alabama. The amount of erosion for Well 15668 was estimated based on the burial history models for the other two wells. The geothermal history was modeled to correlate the basin model's Easy %R_o values with measured R_o values from Carroll et al. (1995).

2.7 Volumetric Analysis

The type and volume of hydrocarbons generated and stored within the Neal shale were determined using a combination of techniques. The basin modeling software Petromod[®] (2011) allows the type and volume of hydrocarbons adsorbed to organic matter to be determined using the Langmuir equation and/or the Pepper and Corvi (1995) method. However, because the software lacks the ability to incorporate pore space water saturations and would not allow for a statistical analysis of the range of values seen for porosity, water saturation, and the formation volume factor, Rose and Associates risk analysis was used for the volumetric assessment of free hydrocarbons. However, the Rose and Associates Multi-Method Risk Analysis (2012) software cannot calculate the volume of adsorbed gas, so Petromod[®] was used to estimate gas adsorption. Free hydrocarbons were determined by entering the range of values seen for porosity and hydrocarbon saturation, as determined by core analysis from Pashin et al. (2011), the gas expansion factor due to differing pressures across the Basin, and gas recovery efficiencies. Free gas volume estimates represent recoverable gas, while adsorbed gas estimates represent gas-in-place.

3 RESULTS

3.1 XRD Results

Based on results from the quantitative Rietveld analysis of the 54 Neal shale facies samples selected for this study (Tables A-2–A-4), clay contents range from 15.0– 59.5 wt% while quartz concentrations range from 14.7– 37.0 wt%. Quartz content averages 25.2 wt%, while the average clay content is 42.9 wt%. In addition to being clay-rich and quartz-poor as compared to the Barnett Shale of the Fort Worth Basin, where clay content averages 27 wt% and quartz content averages 45 wt% (Bowker, 2003), the Neal shale is also relatively rich in potassium feldspar. Orthoclase ranges in concentration from 3.2– 28.6 wt%, and averages 11.1 wt%. Within the Neal shale facies, the calcite content ranges from below detection to 36.2 wt%, and averages 9.7 wt%. In addition to calcite, dolomite is found within the formation and ranges in concentration from 0.4– 18.1 wt%, averaging 4.9 wt%. In zones where the calcite content of the Neal shale falls below the XRD detection limit, dolomite concentrations average 5.9 wt%.

XRD results for the Neal shale samples from Well 2191 (Table A-2) between depths of 2740–2945 feet, show quartz contents ranging from 16.7– 37.0 wt%, while clay contents range from 20.0– 55.3 wt%. Within the same well, quartz concentrations average 25.2 wt% and clay contents average 42.9 wt%. Calcite concentrations average 10.4 wt%, while the concentration of dolomite averages 4.7 wt%. Within Well 2191, orthoclase concentrations range from 8.3– 28.6 wt% and have a slightly higher average of 12.3 wt%, compared to an average of 11.1 wt% for all well samples.

XRD results from Well 1780 (Table A-3) between depths of 6270–6570 feet confirm that the Neal shale is a clay-rich and quartz-poor formation. The clay contents range from 15.0– 59.5 wt%, while quartz concentrations ranges from 14.7– 35.0 wt%. Clay contents within Well 1780

average 43.2 wt%, while quartz concentrations average 24.6 wt%. It should be noted that the average mineral contents differ by less than 1.0 percentage points between Wells 1780 and 2191, indicating that while there are minor variations in mineralogy within each well, the average Neal shale formation is fairly homogenous.

XRD results from Well 15668 samples (Table A-4) tell a similar story, although the thickness of the Neal shale in this well is less than 25 feet. The quartz concentrations range from 17.8– 37.0 wt% and average 29.0 wt%, while the clay concentrations range from 33.8– 50.2 wt% and average 43.4 wt%. While the average quartz content for Well 15668 differs from the overall average by 3.8 percentage points, clay varies by less than 0.5 percentage points. Calcite concentrations within this well average 0.7 wt% and range from below detection to 2.0 wt%. While the concentrations of calcite in Well 15668 samples are low, dolomite concentrations range from 6.0– 7.4 wt%, and average 6.9 wt%. The average dolomite concentration within Well 15668 samples is higher than the overall average by 2.0 percentage points, while the average calcite concentration is lower than the overall average by 9.0 percentage points. Orthoclase concentrations range from 8.8– 12.3 wt% and average 11.0 wt%. In contrast the average concentration of orthoclase within Well 15668 samples differs by less than 0.1 percentage points from the overall average.

3.2 XRF Results

XRF analysis of the 54 Neal shale samples, 6 Floyd Shale samples, and 4 Lewis Limestone samples (Tables A-5–A-7) was conducted to obtain composition data for major, minor and trace element chemistry. (Major and minor element data are given in Tables A-5–A-7). The SiO₂ concentrations for the Neal shale range from 46.1– 66.9 wt% and average 60.2 wt%, while in the

Floyd Shale SiO₂ concentrations range from 65.7– 88.9 wt% and average 79.1 wt%. The Al₂O₃ contents in the Neal shale range from 7.3– 22.0 wt% and average 17.4 wt%, while in the Floyd Shale Al₂O₃ ranges from 5.8– 12.4 wt% and average 8.8 wt%. CaO concentrations within the Neal shale range from 1.4– 33.6 wt% and average 8.9 wt%. CaO concentrations in the Floyd Shale range from 1.4– 15.9 wt% and average 5.8 wt%.

Overall, trace element abundance within the siltstone facies of the Floyd Shale is less than that of the black, organic-rich Neal shale (Tables A-8–A10). The trace elements V, Cr, Ni, Cu, Zn, Rb, Sr, Y, Nb, Ba, and U show an average decrease of 47.2 percent as we transition from the Neal shale to the Floyd Shale, while Mo and Zr increase 36.2 percent. However, due to the standard deviation of the Mo concentration data (3.4 ppm in the Neal shale versus 13.3 ppm in the Floyd Shale), the apparent decrease may not be significant. Chromium concentrations decrease 69.0 percent, from an average of 433.3 ppm in the Neal shale to an average of 90.2 ppm within the Floyd Shale. Average nickel concentrations also decrease 64.7 percent, from 112.0 ppm to 29.4 ppm.

The correlation matrix (Figure A-1) shows that TOC in the Neal shale is strongly related to the presence of 6 trace elements (Cr, Ni, Cu, Zn, Ba, and Mo), with r values ranging from 0.81– 0.96, and is moderately correlated with K and Y, with r values ranging from 0.65– 0.73. The strongest TOC correlations, with r values above 0.9, are with Cr, Ni, and Mo. Molybdenum concentrations range from 3.2– 40.0 ppm, and average 8.4 ppm. Nickel concentrations within the Neal shale range from 20.8– 163.9 ppm and average 78.2 ppm. Chromium concentrations range from 67.5– 778.1 ppm and average 273.5 ppm. The sum of these three trace element concentrations (Cr+Mo+Ni) was plotted against the shale TOC content in Figure 6.

Linear regression of TOC data reported by Pashin et al. (2011) and the Cr+Mo+ Ni concentrations obtained from XRF analysis in this study, gave the following relationship: $TOC=0.0079(Cr+Mo+Ni) - 0.756$. Using this relationship, the TOC content of shale samples can be estimated for other depths where pyrolysis data are not available. The estimated TOC values are shown in Table 1 and compared with measured TOC data from Pashin et al. (2011).

The average value of estimated TOC for the shale samples is 2.07 wt%, excluding the Lewis Limestone. If Floyd Shale samples are excluded, the average estimated TOC for the Neal shale is 2.27 wt% (Table 1). Estimated TOC values within the Neal shale range from 0.30–6.85 wt%, based on XRF trace element analysis.

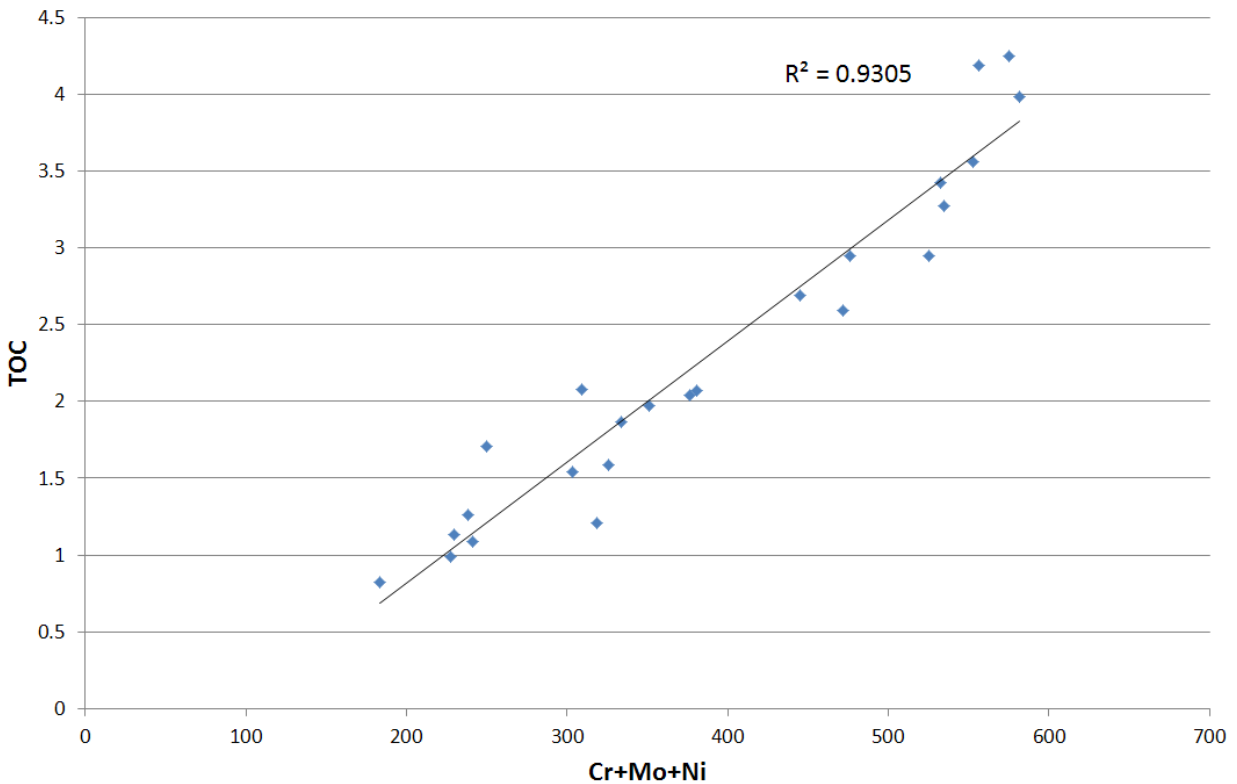


Figure 6: Graph of TOC values obtained by pyrolysis (Pashin et al., 2011) vs. Cr+Mo+Ni concentrations, determined by XRF analysis, for the Neal shale samples.

Table 1: Comparison of TOC values estimated from XRF Cr+Mo+Ni concentration with measured TOC values from Pashin et al. (2011).

Depth (ft)	Formation	Cr (ppm)	Ni (ppm)	Mo (ppm)	Sum	Estimated TOC	Measured TOC	% Difference
2740-45	Neal	184.16	59.38	6.03	249.56	1.22	1.71	28.9%
2750-55	Neal	251.09	73.00	7.96	332.06	1.87		
2760-65	Neal	252.80	75.17	8.87	336.85	1.91		
2770-75	Neal	351.17	90.21	10.35	451.72	2.81		
2780-85	Neal	448.34	111.97	14.69	575.01	3.79	4.25	10.9%
2790-95	Neal	454.37	115.42	14.43	584.22	3.86		
2800-05	Neal	350.17	95.75	10.04	455.96	2.85		
2810-15	Neal	303.77	77.93	5.87	387.57	2.31		
2820-25	Neal	296.21	78.36	5.88	380.45	2.25	2.07	8.7%
2830-35	Neal	337.24	84.26	6.56	428.06	2.63		
2840-45	Neal	295.79	75.97	6.38	378.14	2.23		
2850-55	Neal	344.33	89.49	8.95	442.77	2.74		
2860-65	Neal	394.07	99.52	12.22	505.80	3.24		
2870-75	Neal	445.53	111.38	13.78	570.70	3.75		
2880-85	Neal	325.40	93.48	7.79	426.67	2.61		
2890-95	Neal	226.52	70.65	5.65	302.83	1.64		
2900-05	Neal	293.73	87.61	6.62	387.96	2.31		
2910-15	Neal	318.39	83.32	7.90	409.62	2.48		
2920-25	Neal	433.26	112.01	10.98	556.25	3.64	4.19	13.2%
2930-35	Neal	155.15	50.56	6.96	212.66	0.92		
2940-45	Neal	113.45	37.37	4.48	155.30	0.47		
2950-55	Floyd	109.21	44.36	5.63	159.20	0.50		
2960-65	Floyd	98.92	33.96	3.16	136.04	0.32		
2970-65	Floyd	107.22	28.75	4.20	140.16	0.35		
2980-85	Floyd	67.47	22.28	4.16	93.92	-0.01		
2990-95	Floyd	82.34	20.79	4.16	107.29	0.09		
3000-05	Floyd	75.87	26.12	39.98	141.97	0.37		
6270-80	Neal	125.72	53.09	4.22	183.03	0.69	0.82	15.9%
6280-90	Neal	129.30	50.45	5.68	185.43	0.71		
6290-00	Neal	147.02	65.51	4.27	216.79	0.96		
6300-10	Neal	158.82	63.53	5.19	227.54	1.04	0.99	5.2%
6310-20	Neal	182.43	62.26	5.44	250.13	1.22		
6320-30	Neal	181.78	62.66	5.77	250.21	1.22		
6330-40	Neal	246.65	78.81	8.49	333.95	1.88	1.87	0.7%
6340-50	Neal	261.38	81.04	8.69	351.11	2.02	1.97	2.4%
6350-60	Neal	235.57	75.35	7.76	318.68	1.76	1.21	45.6%
6360-70	Neal	159.59	65.20	4.69	229.48	1.06	1.13	6.5%
6370-80	Neal	167.08	66.53	4.92	238.54	1.13	1.26	10.4%

Table 1, continued: Comparison of TOC values estimated from XRF Cr+Mo+Ni concentration with measured TOC values from Pashin et al. (2011).

Depth (ft)	Formation	Cr (ppm)	Ni (ppm)	Mo (ppm)	Sum	Estimated TOC	Measured TOC	% Difference
6380-90	Neal	169.11	66.78	4.99	240.87	1.15	1.09	5.2%
6390-00	Neal	222.23	75.87	5.39	303.49	1.64	1.54	6.6%
6400-10	Neal	207.37	72.95	5.19	285.51	1.50		
6410-20	Neal	241.97	78.03	5.46	325.46	1.82	1.59	14.2%
6420-30	Neal	420.58	104.93	9.12	534.64	3.47	3.27	6.0%
6430-40	Neal	366.37	97.03	8.05	471.46	2.97	2.59	14.6%
6440-50	Neal	368.16	99.62	8.72	476.50	3.01	2.95	2.0%
6450-60	Neal	408.24	107.29	10.02	525.55	3.40	2.95	15.1%
6460-70	Neal	432.90	109.30	10.78	552.99	3.61	3.56	1.5%
6470-80	Neal	342.84	93.64	8.57	445.04	2.76	2.69	2.6%
6480-90	Neal	451.04	118.09	12.32	581.45	3.84	3.98	3.6%
6490-00	Neal	607.93	148.13	15.42	771.47	5.34		
6500-10	Neal	402.01	119.54	10.91	532.46	3.45	3.42	0.9%
6510-20	Neal	285.60	83.24	7.59	376.43	2.22	2.04	8.7%
6520-30	Neal	113.36	36.90	5.10	155.36	0.47		
6530-40	Neal	94.54	33.60	5.15	133.30	0.30		
6540-50	Neal	185.45	61.82	5.50	252.77	1.24		
6550-60	Neal	195.98	104.66	8.67	309.31	1.69	2.08	18.9%
6560-70	Neal	143.23	59.62	5.82	208.67	0.89		
9013.1	Neal	589.39	106.84	10.47	706.71	4.83		
9022.8	Neal	778.13	163.86	21.33	963.32	6.85		
9033.0	Lewis	48.03	47.02	11.38	106.42	0.08		
9044.0	Lewis	0.00	11.30	4.61	15.91	-0.63		
9053.0	Neal	134.25	60.11	5.24	199.59	0.82		
9062.7	Lewis	25.36	13.75	5.69	44.80	-0.40		
9073.0	Lewis	0.00	7.30	4.56	11.86	-0.66		

3.3 Strength Test Results

Table A-11 lists the results of unconfined uniaxial compressive point load test tests performed on 40 Neal shale samples and 9 Lewis Limestone samples selected from Well 15668 core. The strength of the Neal shale samples averaged 0.82 MPa ($\sigma=0.35$ MPa) for diametral tests and averaged 3.19 MPa ($\sigma=0.96$) for axial tests. The average strength at each depth for the diametral tests ranged from 0.43 MPa at 9,022.8 ft to 1.16 MPa at 9,021.0 ft. For axial tests, the

highest average strength was measured for the 9024.2 ft sample, which tested with a strength of 3.77 MPa; the lowest average strength was measured for the 9013.0 ft sample, which tested with a strength of 2.30 MPa. The Lewis Limestone showed greater strength in diametral tests than in axial tests, with a high diametral strength value of 35.76 MPa for the 9,073.0 ft sample and a low axial strength value of 0.51 MPa for the 9,044.6 ft sample.

3.4 FESEM Results

To verify the interpretation of Neal shale organic matter, and inorganic minerals, energy dispersive spectroscopy (EDS) was performed on selected samples. EDS maps of individual element concentrations were combined to allow conclusions to be made about the material at a specific imaged spot. The blue arrow in Figure 7 indicates the location of organic matter, which shows as a dark material. The organic matter interpretation was confirmed by examining EDS maps for carbon and calcium, which verified that the carbon is not associated with CaCO_3 . EDS maps also helped with the identification of unknown materials on or within the sample. For example, the red arrow on Figure 7 points to a pyrite framboid that has scavenged molybdenum.

Once identifications of the shale constituents were confirmed, 3-D reconstructions of shale organic matter, porosity, and pyrite distributions could be completed. A combination of both BSE detector and SE detector images provided the most information when analyzing the reconstructions. Because the SE detector uses low-energy secondary electrons that originate within a few nanometers of the surface, a high resolution image of the surface can be obtained. However, charging and shadowing of the surface can make it difficult to get an accurate analysis of porosity development using ImageJ software, which relies on image contrast for analysis. Figure 8 shows a comparison of BSE and SE images showing organic porosity development.

The organic porosity that developed with thermal maturation is much more visible in the SE image, compared to the BSE image. However, it was found that by adjusting the threshold value of the BSE detector to match the porosity imaged with the SE detector, the BSE detector also can be used to analyze porosity development, which negates the image charging and shadowing produced by the SE detector. Figure 9 shows the 3-D reconstruction completed for sample 3000-05, and Table 2 shows the results of the analysis after the samples were reconstructed.

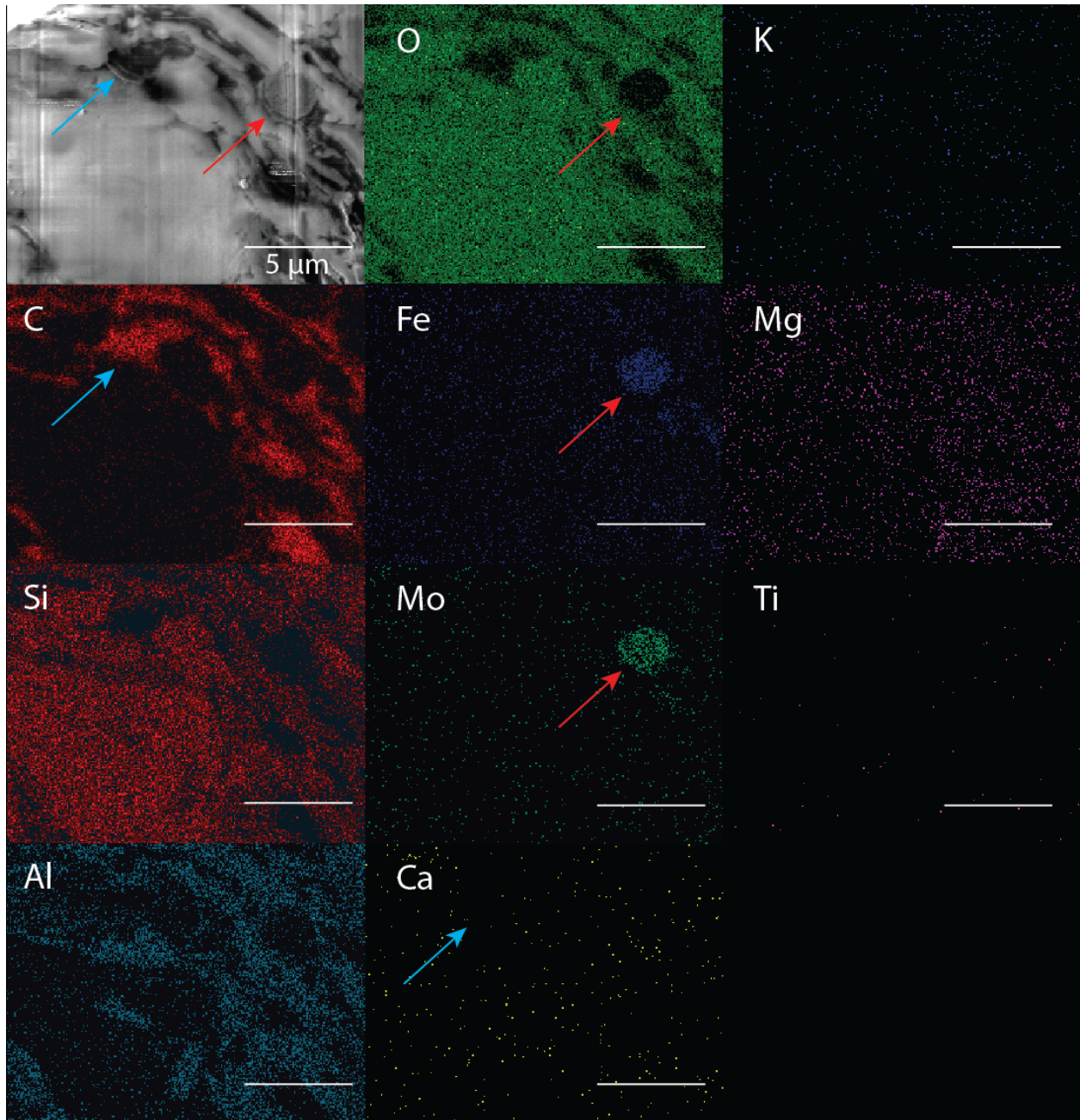


Figure 7: EDS maps of Neal shale 2920-25 ft sample, showing the location of organic matter (blue arrow) and a pyrite framboid (red arrow). The scale bar shows 5 μm for all images.

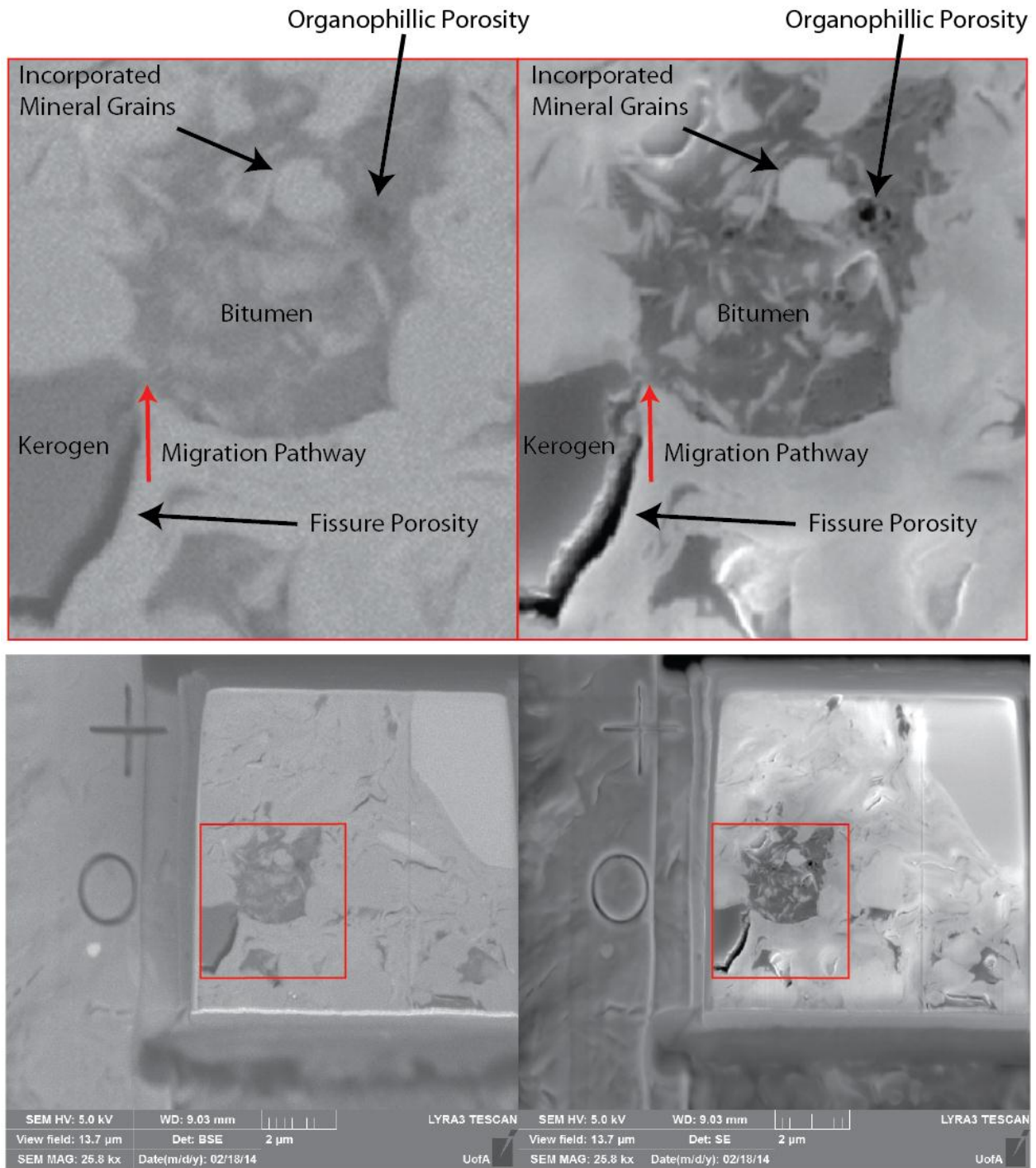


Figure 8: Images of the Neal shale 3000-05 ft sample collected using the BSE detector (left) and the SE detector (right). Notice the better image contrast and detail produced by the SE detector.

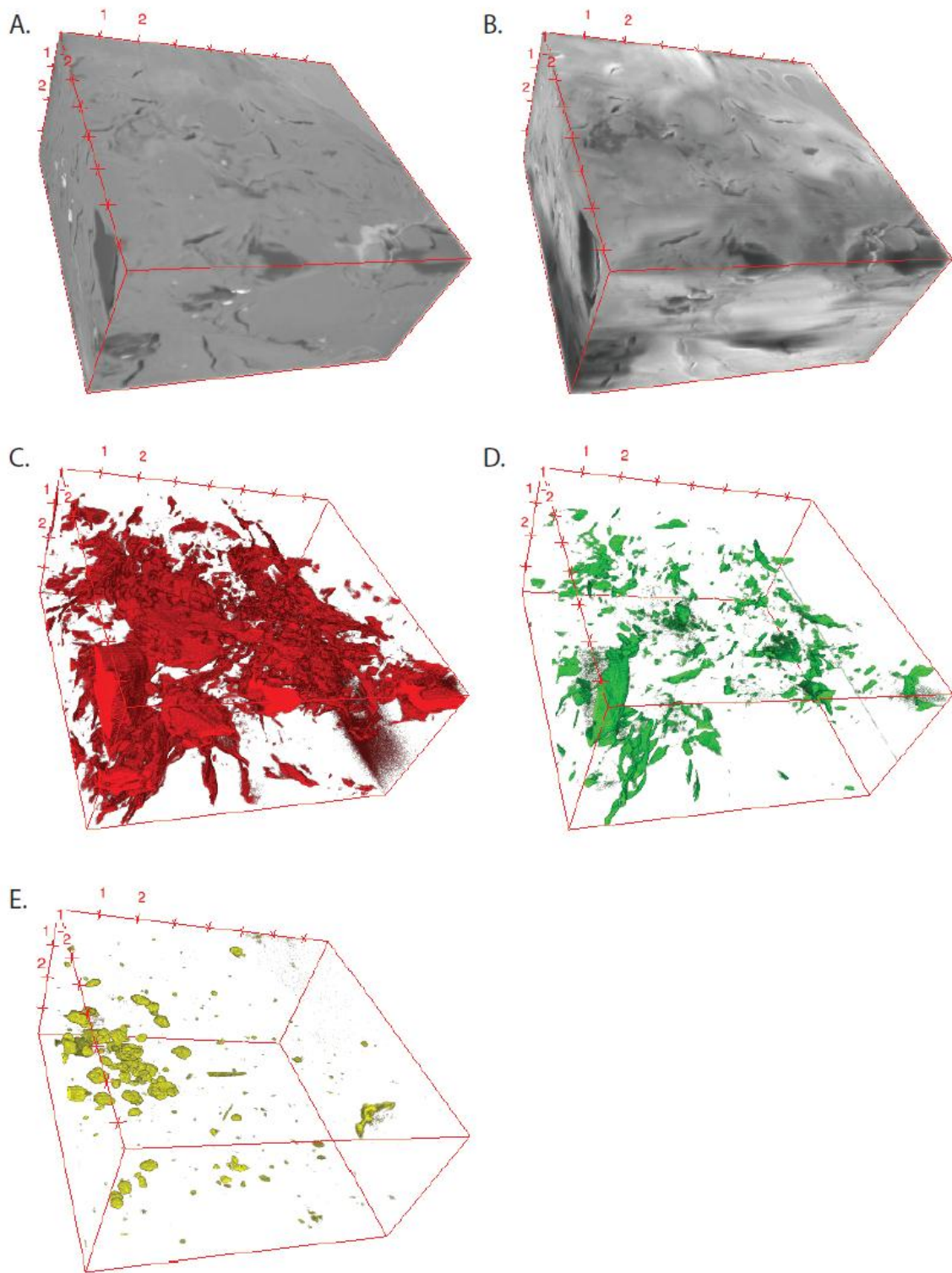


Figure 9: 3-D models of Neal shale 3000-05 ft sample from well 2191 showing the reconstructed sample using A) the BSE detector, B) the SE detector, C) reconstructed organic matter, D) porosity, and E) pyrite with the scale bar in micrometers.

Table 2: Results of FESEM 3-D reconstruction analysis of Neal shale samples, reported in volume percent with porosity representing total porosity (- indicates samples where the BSE detector was not used).

Depth	Porosity	Organic Matter	Pyrite
2740-45	0.17	1.58	0.18
2830-35	1.12	3.80	0.63
2920-25	0.08	22.07	0.23
3000-05	0.43	5.90	0.42
6270-80	0.04	0.00	0.00
6370-80	7.74	0.00	0.09
6460-70	0.08	1.06	0.01
6560-70	0.01	3.71	1.06
9013.1	0.20	0.00	1.67
9022.8	0.12	8.95	-
9033.0	0.20	0.70	0.06
9044.0	0.01	0.00	-
9053.0	0.07	0.69	-
9062.7	1.56	0.00	0.00
9073.0	1.46	0.00	0.00

3.5 Modeling Results

3.5.1 Kinetic Porosity

The calculated kerogen porosity within the Neal shale ranges from 0.26– 4.82% and averages 2.33% (Table 3). These values were calculated using Jarvie et al. (2007) alternative methods to calculate input values for the Modica and Lapierre (2012) kinetic porosity model. For Well 2191, with measured R_o values ranging from 0.92– 0.98%, calculated kerogen porosity ranges from 0.26–1.15% and averages 0.62%. Well 1780 has measured R_o values ranging from 1.44– 1.59%; the calculated kerogen porosity ranges from 0.74– 4.82% and averages 2.40%. Finally, for Well 15668 with Easy % R_o of 2.2– 2.3%, kerogen porosity ranges from 2.21– 4.63% and averages 3.68%.

Table 3: Table of calculated kerogen porosity including input data.

Top Depth (ft)	Hlo	TRHI	iTOC	Cc	PhiK
2740	439.25	0.49	1.94	0.24	0.55
2780	439.25	0.09	4.36	0.27	0.26
2820	439.25	0.68	2.55	0.28	1.15
2920	439.25	0.24	4.51	0.29	0.75
3010	439.25	0.95	0.61	0.27	0.37
6270	439.25	0.99	1.13	0.28	0.74
6300	439.25	0.96	1.35	0.28	0.86
6330	439.25	0.96	2.62	0.30	1.78
6340	439.25	0.93	2.74	0.30	1.82
6350	439.25	0.98	1.68	0.29	1.12
6360	439.25	0.98	1.56	0.28	1.03
6370	439.25	0.97	1.75	0.29	1.15
6380	439.25	0.97	1.50	0.28	0.98
6390	439.25	0.97	2.15	0.29	1.45
6410	439.25	0.97	2.22	0.29	1.50
6420	439.25	0.94	4.74	0.33	3.50
6430	439.25	0.95	3.69	0.31	2.61
6440	439.25	0.93	4.22	0.32	3.02
6450	439.25	0.94	4.23	0.32	3.04
6450	439.25	0.94	3.42	0.31	2.37
6460	439.25	0.93	5.17	0.34	3.82
6460	439.25	0.91	4.16	0.32	2.92
6470	439.25	0.93	4.12	0.32	2.91
6470	439.25	0.92	3.79	0.32	2.63
6480	439.25	0.91	5.80	0.35	4.32
6480	439.25	0.87	5.33	0.34	3.80
6490	439.25	0.96	6.15	0.34	4.82
6500	439.25	0.91	4.92	0.33	3.56
6510	439.25	0.92	2.83	0.30	1.88
6550	439.25	0.97	2.94	0.30	2.04
6560	439.25	0.97	3.78	0.31	2.74
9013.45	439.25	0.95	3.18	0.31	2.21
9016.75	439.25	0.97	5.90	0.34	4.63
9020.85	439.25	0.96	4.10	0.32	2.99
9023.05	439.25	0.95	5.56	0.34	4.24
9024.45	439.25	0.96	5.61	0.34	4.32

3.5.2 Basin Modeling

Basin modeling of Well 2191 (Figure 10) was designed to correlate with the measured R_o values from Carroll et al. (1995). By setting the amount of erosion to 7,300 ft and varying the

geothermal gradient through time, Easy %R_o values from Petromod[®] were 0.9– 1.0%, nearly identical to the measured R_o values of 0.92– 0.98%.

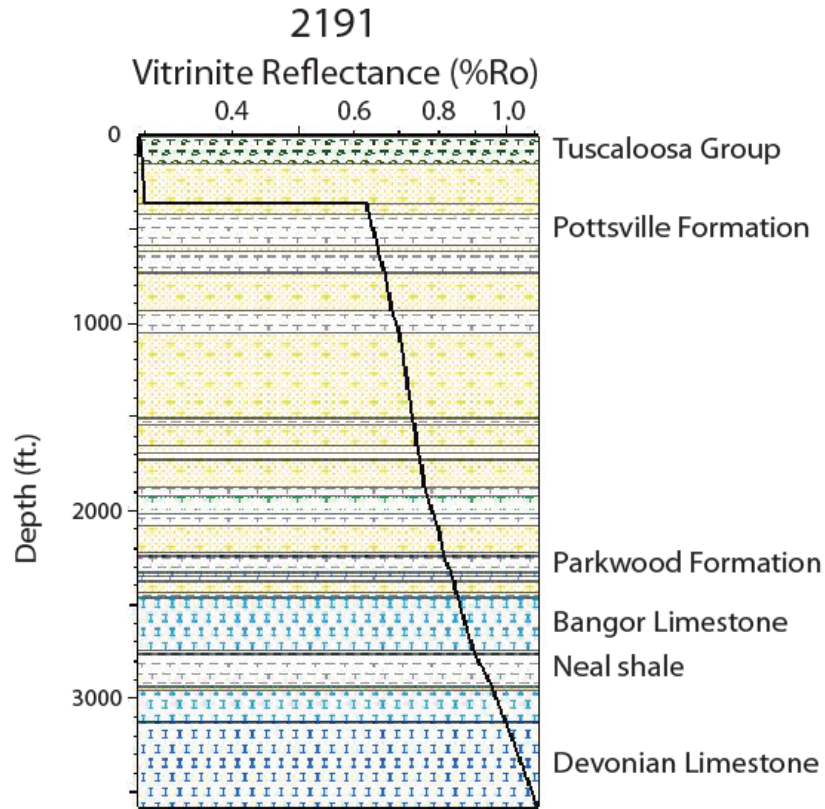


Figure 10: Easy %R_o values for Well 2191.

Basin modeling of Well 1780 (Figure 11) was also designed to match measured R_o values from Carroll et al. (1995). The same geothermal model was used for Well 1780 that was used for Well 2191. Erosion was then set at 7,000 ft to match the measured R_o values of 1.44– 1.59%, producing Easy %R_o values of 1.5– 1.6% for Well 1780.

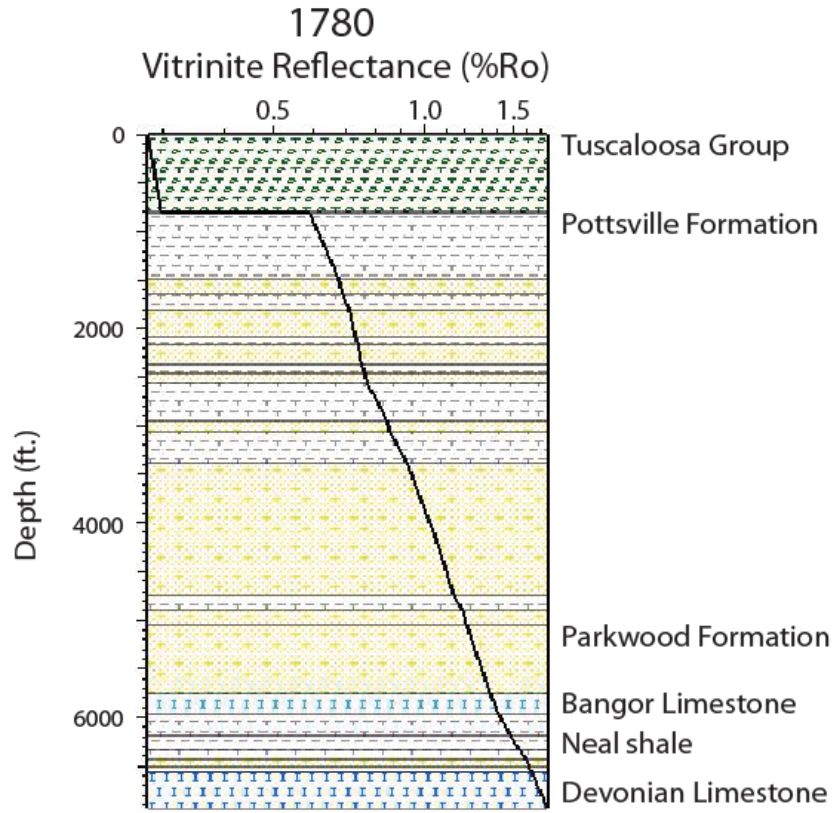


Figure 11: Easy %R_o values for Well 1780.

Basin modeling results from Well 15668 (Figure 12) were found by using the same geothermal gradient and 7,000 ft of erosion. The Easy %R_o values range from 2.2– 2.3% within the Neal shale, as compared to 1.26– 1.52% R_o values calculated from pyrolysis data.

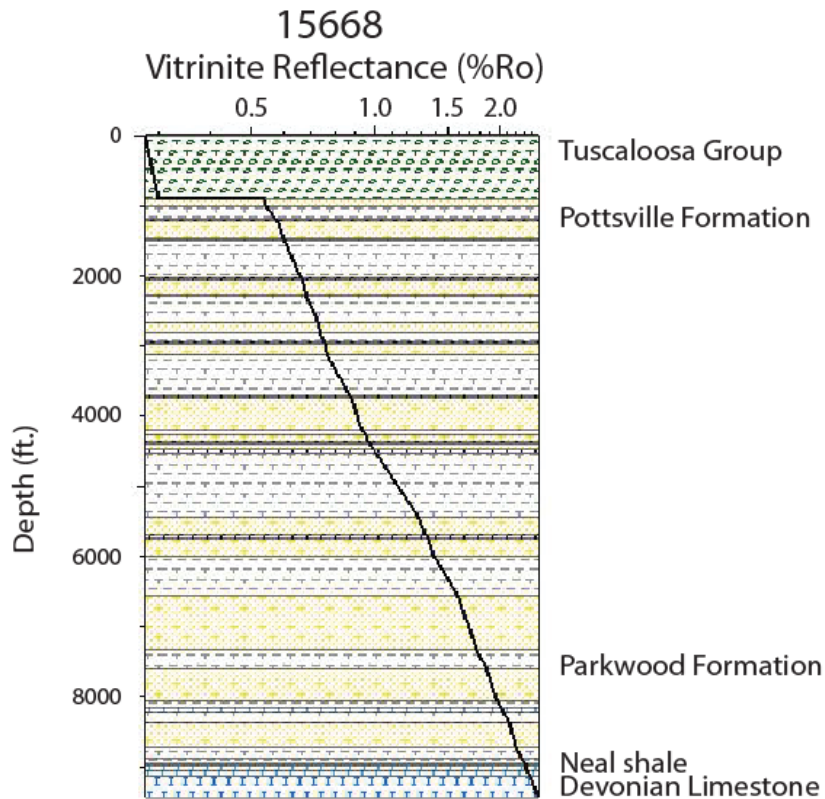


Figure 12: Easy %R_o values for Well 15668.

A burial model for Well 2191 (Figure 13) shows the rapid burial that occurred due to the Alleghanian Orogeny that began at the end of the Carboniferous and ended in the Late Permian. This rapid burial forced the Neal shale in Well 2191 to a maximum depth of approximately 10,000 ft. Uplift then eroded approximately 7,300 ft of Pottsville sediment and brought the Neal shale to much shallower depths. Overlaying Easy %R_o values shows that thermal maturation of the kerogen occurred rapidly and correlates with the maximum depth of burial.

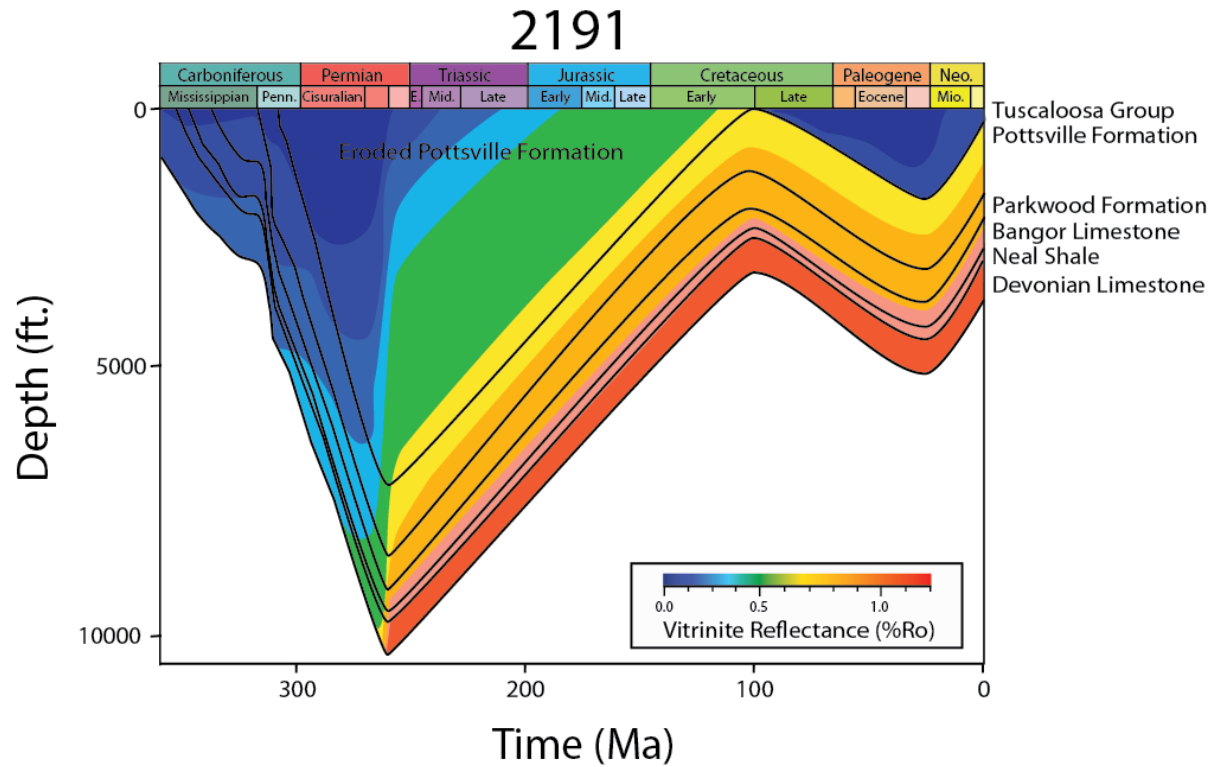


Figure 13: Burial history of Well 2191, including Easy %R_o values as an overlay.

A burial history model of Well 1780 (Figure 14) shows the rapid burial that began at the end of the Carboniferous and continued through the Permian. Rapid burial forced the Neal shale to a maximum depth of 12,500 ft and coincided with the timing of thermal maturation. Uplift and an estimated 7,000 ft of Pottsville sediment erosion then brought the Neal shale to shallower depths ranging from 6,000–6,270 ft.

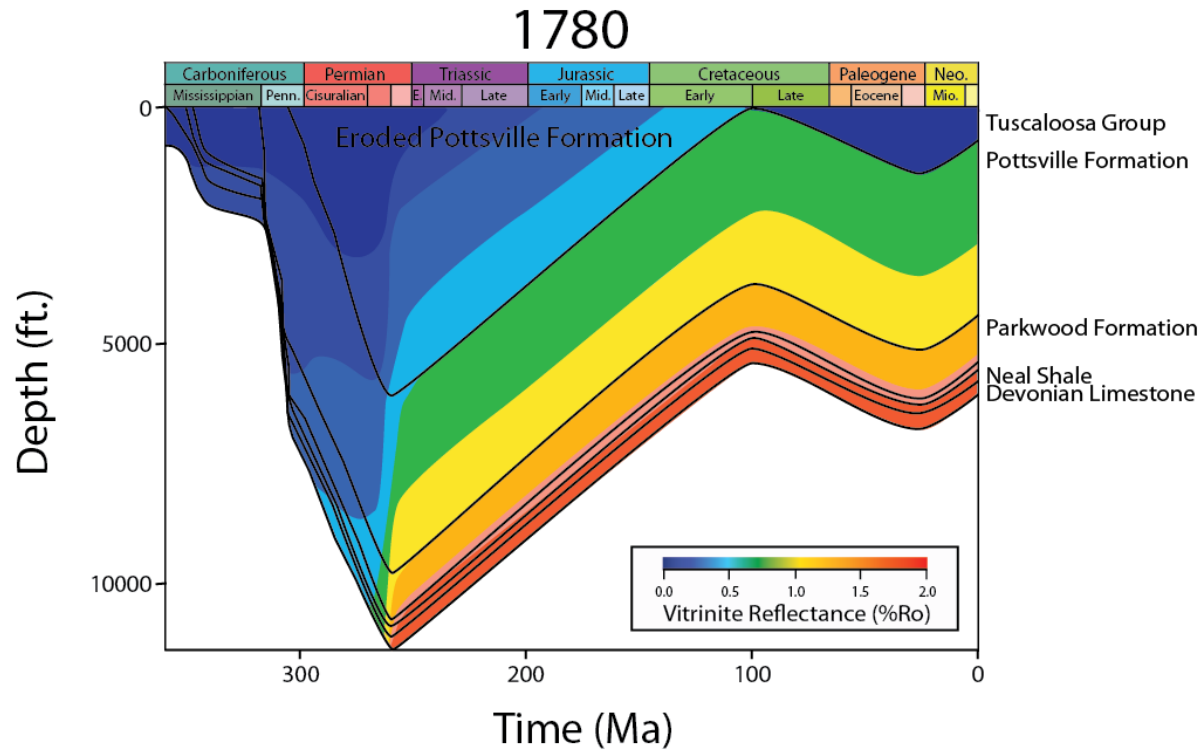


Figure 14: Burial history of Well 1780, including Easy %R_o values as an overlay.

Modeling the burial history based on Well 15668 (Figure 15) also shows the deposition of the Pottsville Formation that buried the Neal shale to a maximum depth of approximately 15,000 ft followed by 7,000 ft of erosion of the Pottsville Group. The timing of maximum burial coincides with the maximum thermal maturity reached by the Neal shale and corresponds to a Easy %R_o value of 2.2– 2.3%. Uplift and erosion placed the Neal shale at its current depth of 9,000–9,025 ft.

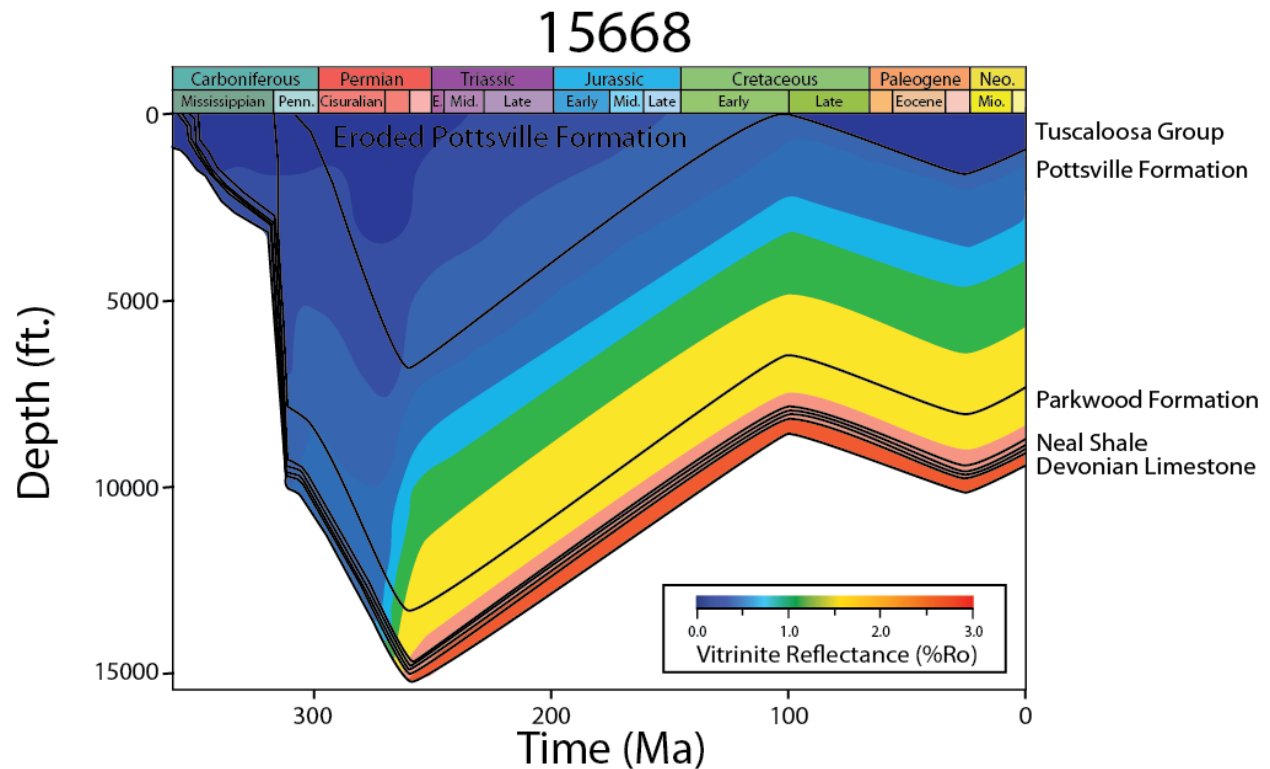


Figure 15: Burial history of Well 15668, including Easy %R_o values as an overlay.

The transformation ratio of the Neal shale (Figure 16) ranges from approximately 60% within Well 2191, to 97% within Well 15668. The 60% transformation ratio places the Neal shale in the early gas window for Well 2191, with hydrocarbon generation occurring rapidly during the point of maximum burial. The 97% transformation ratio puts the Neal shale in the dry gas window within both Well 1780 and Well 15668.

Transformation Ratio

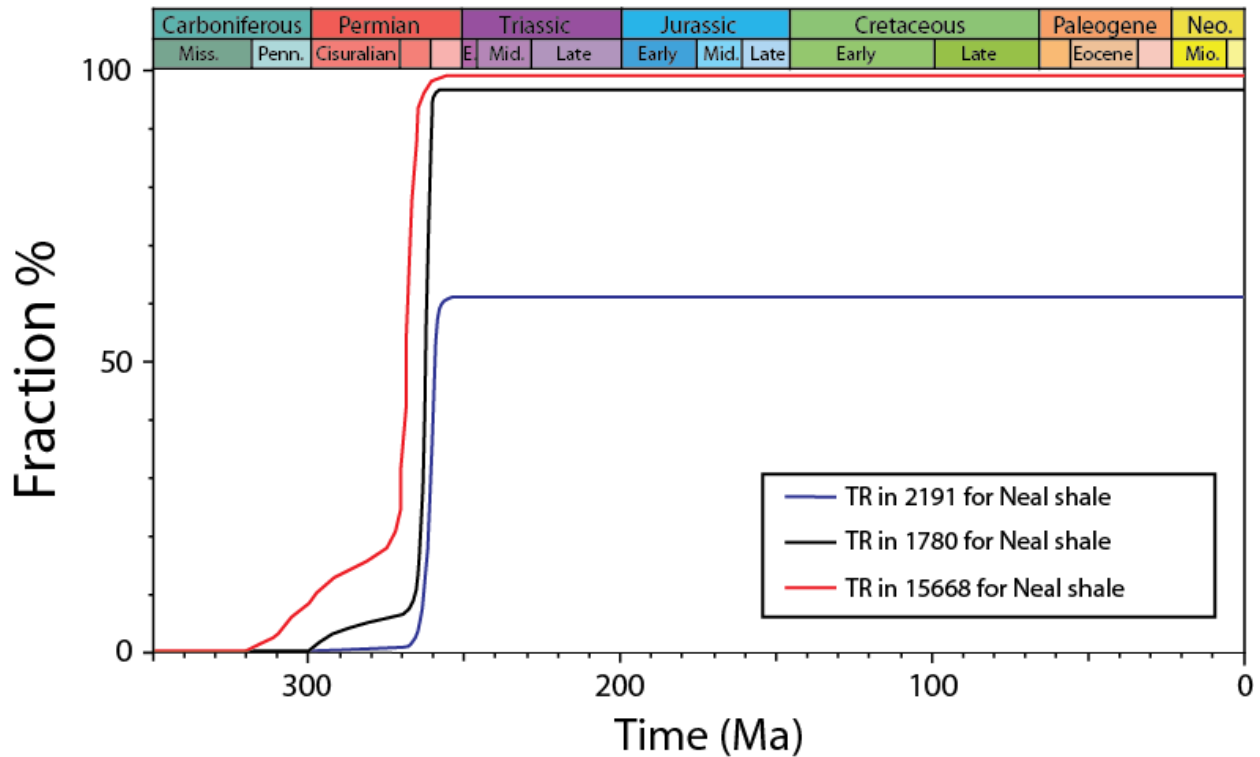


Figure 16: Transformation ratio of the kerogen within the Neal shale.

Figure 17 shows the burial history of Well 2191, including an overlay of the hydrocarbon zones as determined by kinetic modeling. These zones indicate that the Neal shale rapidly passed through the oil window and into the wet gas window during the time of maximum burial. These zones are modeled by incorporating the HI_0 and the TOC of the sample and selecting the kinetic parameters that best match the Neal shale. The kinetic models of hydrocarbon formation in the Kimmeridge Clay were chosen to model the Neal shale because the two shales were deposited in similar environments, are dominated by the same type of kerogen, and have similar HI_0 values.

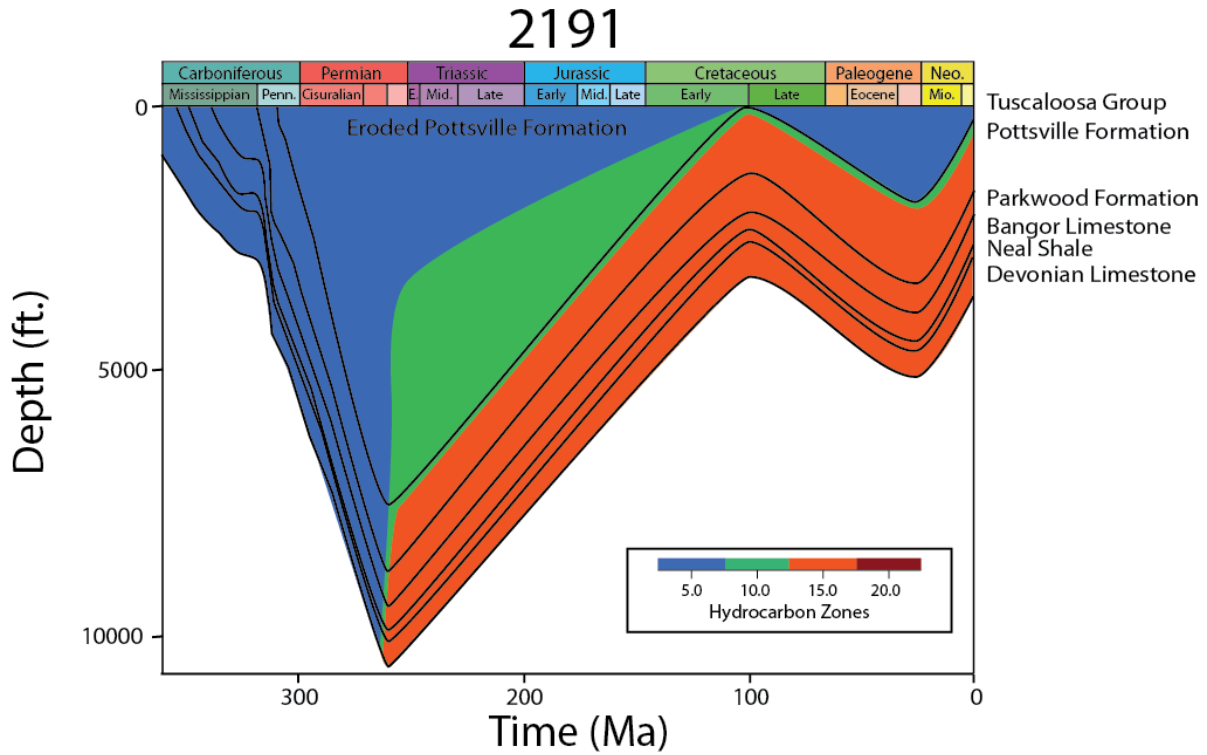


Figure 17: Burial history of Well 2191 with overlain hydrocarbon zones.

A burial model for Well 1780 (Figure 18) with hydrocarbon zone overlays shows the Neal shale rapidly passed through the oil and wet gas window and into the dry gas window. This timing corresponds to a maximum burial depth of approximately 10,000 ft during the Late Permian. The formation has since been uplifted approximately 7,300 ft, whereupon kerogen maturation rapidly ceased.

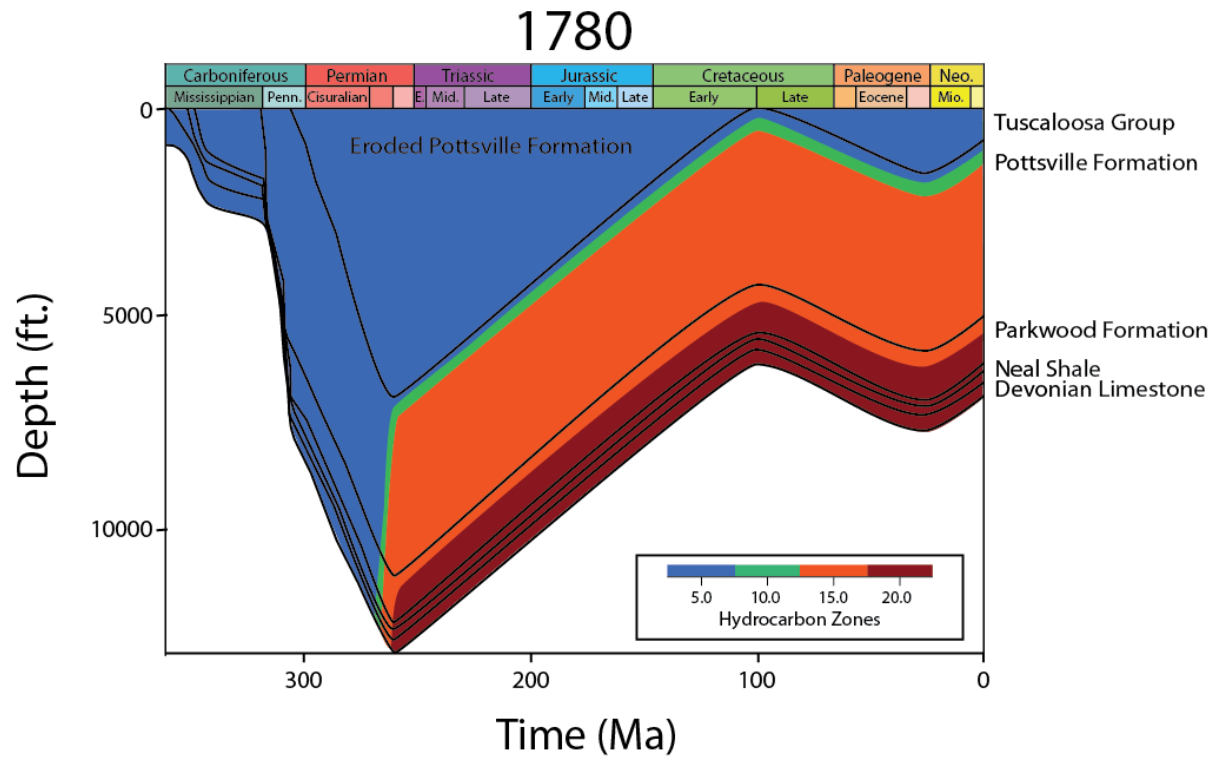


Figure 18: Burial history of Well 1780, with overlain hydrocarbon zones.

Modeling of Well 15668 (Figure 19) shows the Neal shale passed even further into the dry gas window than in Well 1780. The Neal shale passed into the dry gas window beginning at a burial depth of 14,000 ft, and was pushed even further into the dry gas window when buried to the maximum depth of 15,000 ft.

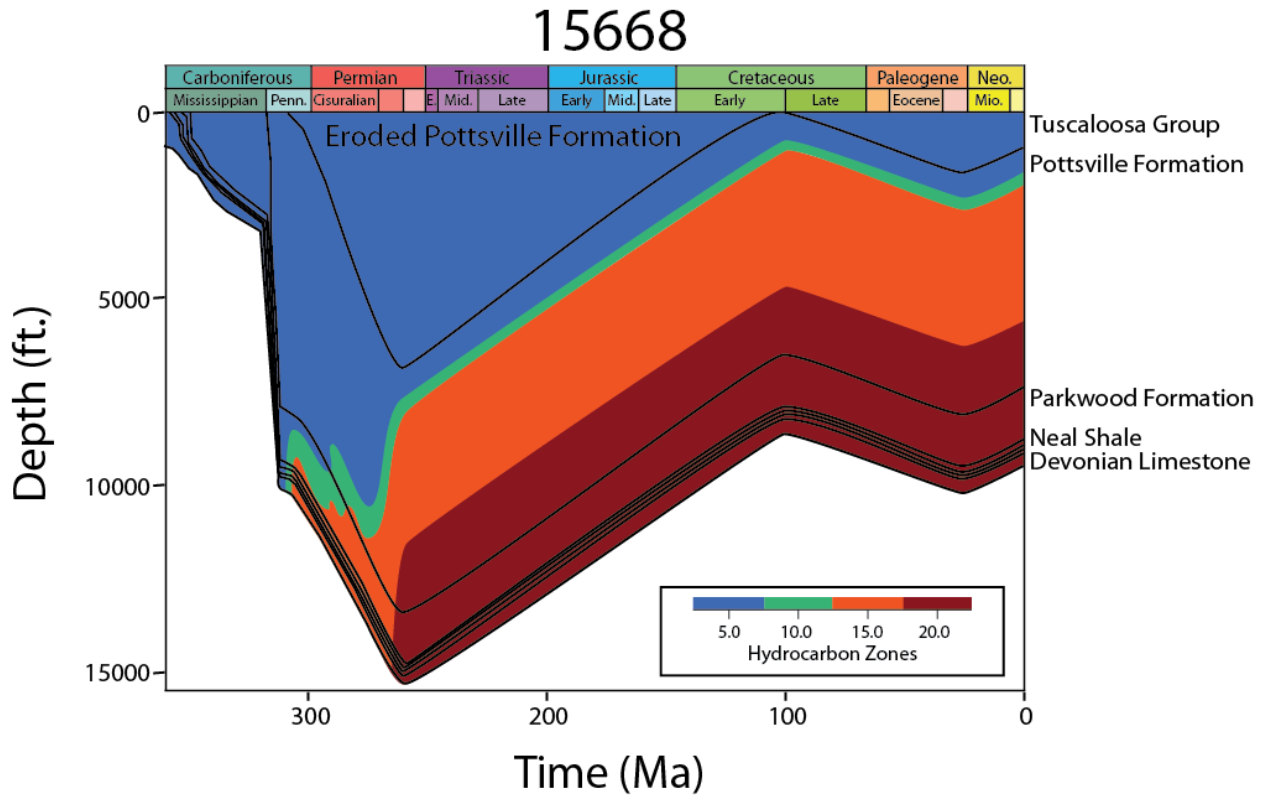


Figure 19: Burial history of Well 15668, with overlain hydrocarbon zones.

4 DISCUSSION

4.1 Mineralogy

XRD analysis results for Well 15668 samples were compared to those reported in the Geological Survey of Alabama's RPSEA shale study by Pashin et al. (2011) for samples from the same well. Mineralogical, tight rock, and Rock-Eval analyses were completed by TerraTek[®] for the RPSEA project. However, the TerraTek study reported illite/smectite and illite + mica as combined values. As a result, it is difficult to compare the reported clay contents with those determined by this study. The chlorite values differ by 7.9 wt% and the total wt% of clay varies by 10 wt% for the 9013.1 ft sample analyzed by this study, compared to TerraTek's[®] results for a sample at 9013.2 feet. These differences in mineralogic composition likely come from the different sampling depths. In both studies, the Neal shale was determined to be a clay-rich formation.

An additional area of difference in XRD results is seen when the plagioclase concentrations at 9,022.8 feet and 9,022.9 feet are compared. The largest difference is apparent when the plagioclase content reported by TerraTek for a sample at 9,022.9 feet is compared to that reported for albite by this study for a sample at 9,022.8 feet. The large difference of 7.7 wt% may be accounted for by the different sampling depths or through the use of different plagioclase structures in the Rietveld analyses. This study used the structure for albite because it provided the best fit to the XRD patterns, is the most common plagioclase, and is the most resistant to weathering. These factors make it more likely to be incorporated in a shale formation than anorthite. Despite these differences, the XRD results obtained in this study show good overall agreement with those of Pashin et al. (2011).

A correlation matrix for the average mineralogical, elemental, and TOC contents (Figure A-1) of the Neal shale samples selected for this study shows strontium concentrations correlate to calcite and dolomite, as well as Mg and Ca. This relationship is likely due to Sr substitution for Ca in CaCO_3 which is a function of 1) the Sr/Ca ratio in the liquid phase from which the solid phase is derived, 2) the temperature, and 3) the salinity of the liquid phase as described by Turekian (1955). Sr/Ca ratios within the Neal shale range from 0.004 to 0.013 and average 0.006. Quartz is strongly correlated with the concentration of Si, with a correlation coefficient (r) of 0.86, and moderately correlated to Zr with $r = 0.55$, which is likely due to its association with sediment shed from the same source. If not for the presence of silica within the structure of clay minerals, it should be expected that this correlation would be near 1. The total wt% of the clay minerals chlorite, illite, montmorillonite, and muscovite within the shale samples strongly correlates with many of the trace elements. However, the strongest clay content correlation is to Al, with $r = 0.93$. Pyrite within the shale facies correlates with several trace element concentrations, including V, Cr, Ni, Zn, and Ba, and also correlates with TOC. The genetic relationship between TOC and pyrite formation is due to bacterially mediated sulfate reduction during oxidation of organic matter, resulting in the production of hydrogen sulfide (Emeis and Morse, 1990). Part of this reduced sulfur is then retained in iron sulfide minerals.

A distinction between the Neal shale and the Floyd Shale can be made based on mineralogy and chemical composition. The Neal shale contains less quartz and more clay minerals than the Floyd Shale, which is a mix of gray shale, limestone, and siltstone facies. Because of this mineralogical difference, there is also a difference in the chemical compositions of the shales. The Floyd Shale contains less Al_2O_3 due to the lower clay content. In addition, because the Floyd Shale is richer in quartz, it has a higher SiO_2 concentration. The Neal shale

also contains an average of 2.27 wt% TOC, while the Floyd Shale TOC is less than 0.5 wt%. Because of the lower TOC content, the Floyd Shale has an average decrease of 47.2 percent in the abundance of most trace elements.

The Neal shale sediment was transported towards the southeast along depositional strike of the Warrior platform, and deposited in epeiric ramp and basinal environments during the Late Mississippian. The formation is clay-rich, and quartz-poor with varying amounts of organic matter. Zones where the quartz content is greater than 50 wt% may better represent the Floyd Shale, which is a mixture of gray shale, limestone, and sandstone facies.

The Neal shale thins toward the southeast, where it interfingers with the Lewis Limestone. The Well 15668 core contains 25 feet of the Neal shale facies and 48 ft of the underlying Lewis Limestone. Within the Lewis Limestone is a 0.5 ft thick stringer of the Neal shale. This was confirmed through XRD analysis in which the mineralogy of the stringer shale was nearly identical to the thick section of Neal shale facies.

4.2 Strength Test

Uniaxial strength tests of selected Well 15668 core samples show that the Neal shale has a lower strength than the underlying Lewis Limestone. This suggests that the Lewis Limestone may serve as an active barrier during hydraulic fracturing of the Neal shale, if horizontal wells are used. Hydraulic fracturing of the Barnett Shale within the Fort Worth Basin is more successful where the quartz content is greater than 45 wt% and the clay content is less than 27 wt% (Bowker, 2003). This statement could not be tested within the Neal shale due to the lack of equipment available to accurately measure the maximum load required for failure. However, an overall comparison of the Neal shale strength to the Lewis Limestone strength shows that mineralogy plays an important role in fracturing success.

Axial tests of the Neal shale indicate that it has a higher strength than in diametral tests, for unconfined samples collected at the same depth. This occurs because the formation is highly friable and breaks along pre-existing planes of weakness due to bedding. At reservoir conditions, the Neal shale would not fracture along these planes of weakness, but would cut perpendicularly across them. Axial strength results would thus provide more accurate results when designing the fracture stimulation job. One major factor that could not be tested was the strength of the Neal shale at the confining pressure of the surrounding rock. At reservoir conditions, the Neal shale will not have the same strength as indicated by unconfined compressive strength tests. Strength tests should be conducted at a variety of confining pressures to enable extrapolation to reservoir conditions. Strength tests at reservoir conditions were beyond the scope of this project and the equipment necessary to conduct such tests was not available.

4.3 Organic Porosity

The Neal shale was rapidly buried during the Permian, followed by rapid uplift and subsequent erosion of the overlying Pottsville sediments. During the time of maximum burial, the Neal shale was pushed through the oil window and into the wet-dry gas windows. It was at this time that a large volume of hydrocarbons were generated and expelled into overlying reservoirs. In addition to the large volume of hydrocarbons expelled from the formation, the Neal shale also retained a substantial volume of hydrocarbons both within its pore spaces and adsorbed onto organic material. The basin model indicates that further burial during the Cretaceous-Paleogene did not result in further maturation of the kerogen or petroleum generation. The Neal shale is modeled to contain condensate within the less mature Well 2191,

while dry gas dominates in the more mature Wells 1780 and 15668. The average TOC used for this analysis was 2.27 wt%, based on the correlation of XRF Cr+Ni+Mo concentrations with TOC data obtained by pyrolysis (Pashin et al., 2011). Also, the Langmuir pressure and volume determined by the Pashin et al. (2011) study were incorporated in the basin model to determine the adsorbed volume of hydrocarbons.

Figure 8 shows that there are two distinctly different types of porosity present within the Neal shale organic matter. The first type is fissure porosity, which may be the result of oil generation, as proposed by Curtis et al. (2013). The fissure porosity is only present in the organic material at the lower left, and ends at the juncture with the more circular patch of organic matter. Curtis et al. (2013) suggested that with oil generation and pressure build up, oil may hydraulically fracture the organic matter. Oil generation may therefore be the cause of the fissure porosity seen within the organic matter of the Neal shale. The second porosity type is organophillic porosity, in which round pores have developed from the generation of gas. Organophillic porosity is only evidenced within the adjacent circular patch of organic material. The interpretation for the organic material shown in Figure 8 is that the irregular patch of organic material in the lower left of the image is kerogen, and the circular patch of organic material is bitumen or pyrobitumen. As the kerogen broke down to form oil, overpressuring occurred, creating the kerogen fissure porosity and allowing the migration of petroleum. In this sample, the petroleum did not migrate far before organophillic porosity developed. The other distinguishing characteristic between these two patches of organic material is that the circular patch shows entrained inorganic mineral grains, which likely formed during the fracturing process.

Kerogen within the Neal shale has been reported by Carroll et al. (1995) to be dominated by matrix bituminite (95%), with minor accumulations of liptinite (1%), vitrinite (3%), and inertinite (1%). Using these kerogen maceral concentrations and equation (1), the HI_o value calculated in the current study for the Neal shale is 439.25. This value was compared to the HI values calculated by Pashin et al. (2011) for the least mature Well 2191, in which the highest HI value was 427. This similarity suggests that the calculated HI_o value of 439.25 is reasonable.

The hypothesis of this study was that as kerogen breaks down to form hydrocarbons, porosity ensues. Results from the Modica and Lapierre (2012) kinetic model of porosity development indicate that kerogen within the Neal shale has developed as much as 4.82% porosity. However, this value does not agree with FIB-FESEM observations of kerogen porosity within the Neal shale. The maximum organic porosity found in this study was 1.12% at a sample depth of 2,830 ft, and organic matter interpreted to be kerogen was not observed to develop any organophillic porosity. While the maximum observed organic porosity value is nearly identical to the kinetic model calculation of 1.15% kerogen porosity at sample depth 2,820 ft, at all other sample depths porosity is highly overestimated by the kinetic model. One possible explanation for this discrepancy is that the FESEM cannot resolve pore spaces smaller than a few nanometers. This would lead to the method underestimating the porosity within both organic matter and the inorganic matrix, if it is in the sub-nanometer size range. Another explanation for the difference in calculated and observed porosity development may be that kerogen does not break down with thermal maturation to form porosity, as originally hypothesized. If the interpretation of Figure 2 is correct, then it is not the kerogen that breaks down to form organophillic porosity, as modeled by Modica and Lapierre (2012), but rather bitumen or pyrobitumen. This indicates that thermal maturity is not the only driving force for porosity

development, and suggests that the chemical makeup of the organic material is also a primary control. This conclusion agrees with previous studies of shale porosity development in which samples at the same thermal maturity level were observed to have different kerogen porosity values (Curtis et al., 2011, 2012). To accurately model organic porosity development, the volumes of bitumen or pyrobitumen retained during maturation and the degree of compaction during subsequent burial need to be known. In addition, organic fracturing caused by oil generation should be investigated further as a source of porosity.

4.4 Volumetric Analysis

The Neal shale has a large potential to store hydrocarbons. Porosity values within the formation range from 2.4– 7.7%, while hydrocarbon saturation values range from 29.9– 78.8%, based on TerraTek[®] TRA (Pashin et al., 2011). Rose and Associates risk analysis performed using this data, and the results of basin modeling, were used to calculate the volume of recoverable free gas and adsorbed gas in place (table 4).

Table 4: Recoverable free gas estimates and adsorbed gas-in-place based on risk analysis and basin modeling.

Free Gas				
	Area (km ²)	Oil (MMbo)	Gas (Bcf)	
P90	6690	0.01	227.22	
P10	6690	12.89	4943.27	
Adsorbed Gas				
Well	Area (km ²)	(Mcf/km ²)	Mcf	Tcf
2191	2230	179915.10	401210673.00	401.21
1780	2230	19559.71	43618153.30	43.62
15668	2230	6902.39	15392329.70	15.39
Total	6690	-	460221156.00	460.22

The Neal shale of Alabama has a large resource potential. Based on Rose and Associates risk analysis, there is a 10% chance that 4.94 Tcf and a 90% chance that 227.22 Bcf may be recovered from the free space of the formation. Because the formation is within the wet gas window for Well 2191, it has been estimated that the oil concentration may range from 0–5%, at most. If this were the case, there would be a 10% chance that 12.89 MMbo are recoverable from the formation and a 90% chance that 0.01 MMbo are recoverable. The estimated volume of recoverable free gas from the Neal shale is minor compared to the volume of adsorbed gas within the formation. As the temperature of the formation decreases, Zhou et al. (2000) showed that the ability of methane to adsorb on activated carbon increases. The molecular sizes of the hydrocarbon components present within the formation also play a role in determining adsorption affinities and thus the overall volume of gas adsorbed to the organic material (Jarvie et al., 2007). Pepper (1992) estimated that gas adsorption may be reduced by a factor of 10 at high maturities. For example, as the source rock passes from the oil window to the gas window, adsorption of higher molecular weight hydrocarbons decreases from approximately 200 mg HC/g TOC to 20 mg HC/g TOC. An average TOC value of 2.27 wt% was used to determine the volume of gas adsorbed within the Neal shale. At a temperature of approximately 150°F, Easy %R_o of 2.1–2.2% and lithostatic pressure of 62– 63 MPa, the Neal shale adsorbs 6,902.39 Mcf/km². Gas adsorption on the Neal shale increases dramatically at lower temperatures and maturities as seen in the adsorption model of Well 2191 (Table 4). The bottom-hole temperature for Well 2191 is approximately 100°F, while lithostatic pressure ranges from 19.5– 21 Mpa. Gas adsorption may be as great as 179,918 Mcf/km² within this well, where condensate is also modeled to occur.

5 CONCLUSIONS

The Neal shale of Alabama is a clay-rich, quartz-poor formation, with TOC contents averaging 2.27 wt%. TOC values can be estimated for samples where pyrolysis data are lacking, using a linear equation derived from the correlation between the sum of trace element concentrations (Cr+Mo+Ni) and measured TOC values.

Porosity within the Neal shale is a mix of fissure, organophillic, and intergranular porosity. Kinetic models of porosity development indicate that organic matter within the Neal shale may have developed as much as 4.5% porosity, while FIB-FESEM results show a maximum of 1.12% porosity development. In addition, there is no evidence for an increase in organic porosity with increasing thermal maturation, based on FIB-FESEM imaging. Organic porosity development within the Neal shale is a mixture of fissure and organophillic porosity. Fissure porosity is likely related to the generation of oil from kerogen creating overpressuring and fracturing. With additional maturation, this was followed by gas generation which created organophillic porosity within bitumen.

Basin modeling shows the Neal shale was rapidly buried during the Mississippian, resulting in kerogen maturation and hydrocarbon generation. Burial was followed by uplift and erosion of the overlying Pottsville sediments from the Early Permian to the Early Cretaceous, which brought the formation to much shallower depths. During the time of maximum burial, the Neal shale generated a large volume of hydrocarbons. Up to 460 Tcf of gas may be adsorbed onto the organic matter of the formation, while free gas estimates range from 227–4,493 Bcf. The underlying Lewis Limestone has an average unconfined diametral strength of 22.22 MPa and should serve as an active barrier to hydraulic fracturing efforts in the Neal shale, which has an average unconfined axial strength of 3.19 MPa

REFERENCES

- Ambrose, R. J., Hartman, R. C., Diaz-Campos, M., Akkutlu, I. Y., & Sondergeld, C. H., 2012, Shale gas-in-place calculations part I: New pore-scale considerations. *SPE Journal* **17**(01), 219-229.
- ASTM Standard D7012-13, 2013, Standard test methods for compressive strength and elastic moduli of intact rock core specimens under varying states of stress and temperature, ASTM International, West Conshohocken, PA, 2013, DOI: 10.1520/D7012, www.astm.org.
- Bernard, S., Wirth, R., Schreiber, A., Schulz, H., & Horsfield, B., 2012, Formation of nanoporous pyrobitumen residues during maturation of the Barnett Shale (Fort Worth Basin). *International Journal of Coal Geology* **103**, 3-11.
- Bowker, K. A., 2003, Recent development of the Barnett Shale play. Fort Worth Basin: *West Texas Geological Society Bulletin* **42**(6), 4-11.
- Carroll, R. E., Pashin, J. C., & Kugler, R. L., 1995, Burial history and source-rock characteristics of Upper Devonian through Pennsylvanian strata, Black Warrior Basin, Alabama: Alabama Geological Survey Circular 187, 29 p.
- Cleaves, A. W., & Broussard, M. C., 1980, Chester and Pottsville depositional systems, outcrop and subsurface, in the Black Warrior Basin of Mississippi and Alabama: *Gulf Coast Association of Geological Societies Transactions*, Vol. 30, p. 49-60.
- Curtis, M. E., Ambrose, R. J., Sondergeld, C. S., & Rai, C. S., 2010, Structural characterization of gas shales on the micro- and nano-scales. SPE-137693, paper presented at the CSUG/SPE Canadian Unconventional Resources and International Petroleum Conference, Calgary, Alberta, October 19-21, 2010.
- Curtis, M. E., Ambrose, R. J., Sondergeld, C. H., & Rai, C. S., 2011, Investigation of the relationship between organic porosity and thermal maturity in the Marcellus shale. SPE-144370, SPE Unconventional Gas Conference and Exhibition, June 12-16, 2011, The Woodlands, Texas.
- Curtis, M. E., Cardott, B. J., Sondergeld, C. H., & Rai, C. S., 2012, Development of organic porosity in the Woodford Shale with increasing thermal maturity. *International Journal of Coal Geology* Vol. 103, p. 26-31.
- Curtis, M. E., Sondergeld, C. H., & Rai, C. S., 2013, Relationship between organic shale microstructure and hydrocarbon generation. Society of Petroleum Engineers. Doi:10.2118/164540-MS.
- DIFFRACplus TOPAS R Version 3.0 Tutorial, 2005. *Bruker D8 Advance Diffractometer.*: BRUKER AXS, INC., Madison, WI.

- Emeis, K. C. and Morse, J. W., 1990, Organic carbon, reduced sulfur, and iron relationships in sediments of the Peru Margin, sites 680 and 688. *Proceedings of the Ocean Drilling Program, Scientific Results*, Vol. 112, p. 441-453.
- Goldstein, J., Newbury, D. E., Joy, D. C., Lyman, C. E., Echlin, P., Lifshin, E., Sawyer, L., and Michael, J. R., 2003, *Scanning electron microscopy and X-ray microanalysis*, 3rd edition, Springer, New York, NY. 690 p.
- Groshong, R. H., Jr., Hawkins, W. B*, Jr., Pashin, J. C., and Harry, D. L., 2010, Extensional structures of the Alabama promontory and Black Warrior foreland basin: Styles and relationship to the Appalachian fold-thrust belt, in Tollo, R.P., Bartholomew, M.J., Hibbard, J. P., and Karabinos, P. M., eds., *From Rodinia to Pangea: The Lithotectonic Record of the Appalachian Region: Geological Society of America Memoir 206*, p. 579-605.
- Hatch, J. R., & Pawlewicz, M. J., 2007, Introduction to the assessment of undiscovered oil and gas resources of the Black Warrior Basin province of Alabama and Mississippi, in Hatch, Joseph R., and Pawlewicz, M. J., compilers, *Geologic assessment of undiscovered oil and gas resources of the Black Warrior Basin Province, Alabama and Mississippi: U.S. Geological Survey Digital Data Series DDS-69-I*, chap. 2, 6 p.
- Jarvie, D. M., Hill, R. J., Ruble, T. E., & Pollastro, R. M., 2007, Unconventional shale-gas systems: The Mississippian Barnett Shale of north-central Texas as one model for thermogenic shale-gas assessment. *AAPG Bulletin* **91**(4), 475-499.
- Lopatin, N. V., 1971, Temperature and time as geologic factors in coalification (in Russian): *Izv. Akad. Nauk SSSR, Seriya Geologicheskaya*, (3), 95-106.
- McCarthy, K., Rojas, K., Niemann, M., Palmowski, D., Peters, K., & Stankiewicz, A., 2011, Basic petroleum geochemistry for source rock evaluation. *Oilfield Review* **23**(2), 32-43.
- Modica, C. J. and Lapierre, S. G., 2012, Estimation of kerogen porosity in source rocks as a function of thermal transformation: Example from the Mowry Shale in the Powder River Basin of Wyoming. *AAPG Bulletin* **96**(1), 87-108.
- Okiongbo, K. S., Aplin, A. C., & Larter, S. R., 2005, Changes in type II kerogen density as a function of maturity: Evidence from the Kimmeridge Clay formation. *Energy & Fuels* **19**(6), 2495-2499.
- Pashin, J. C., 1994, Cycles and stacking patterns in Carboniferous rocks of the Black Warrior foreland basin: *Gulf Coast Association of Geological Societies Transactions*, v. 44, p. 555-563.
- Pashin, J. C. and Raymond, D. E., Glacial-eustatic control of coalbed methane reservoir distribution (Pottsville Formation; Lower Pennsylvanian) in the Black Warrior Basin of Alabama, 2004 International Coalbed Methane Symp. Proc., Univ. Alabama, Tuscaloosa, paper 413 (2004) 15 p.

- Pashin, J. C., 2008 Gas shale potential of Alabama: Tuscaloosa, Alabama, University of Alabama, College of Continuing Studies, 2008 International Coalbed & Shale Gas Symposium Proceedings, paper 0808, 13 p.
- Pashin, J. C., Kopaska-Merkel, D. C., Arnold, A. C., and McIntyre, M. R., 2011, Geological foundation for production of natural gas from diverse shale formations: Sugarland, Texas, Research Partnership to Secure Energy for America (RPSEA) Final Report, 7122.17.01; Geological Survey of Alabama Open-File Report 1110, 156 p.
- Pawlewicz, M. J., & Hatch, J. R., 2007, Petroleum assessment of the Chattanooga Shale/Floyd Shale–Paleozoic total petroleum system, Black Warrior Basin, Alabama and Mississippi, in Hatch, Joseph R., and Pawlewicz, Mark J., compilers, Geologic assessment of undiscovered oil and gas resources of the Black Warrior Basin Province, Alabama and Mississippi: U.S. Geological Survey Digital Data Series DDS-69-I, chap. 3, p. 1-23.
- Pelet, R., 1985, Quantitative evaluation of products formed during the geochemical evolution of organic matter, v. 40, no. 5, p. 551-562
- Pepper, A. S., 1992, Estimating the petroleum expulsion behavior of source rocks: A novel quantitative approach, in W. A. England and A. L. Fleet, eds., Petroleum migration: Geological Society (London) Special Publication 59, p. 9-31.
- Pepper, A. S., and Corvie, P. J., 1995, Simple kinetic models of petroleum formation. Part I: oil and gas generation from kerogen. *Marine and Petroleum Geology*, 12(3), p. 291-319.
- PetroMod: Petroleum systems modeling software (v2012.2 Windows 64-bit) [software]. (2011): Schlumberger.
- Rietveld, H.M., 1969, A profile refinement method for nuclear and magnetic structures. *Journal of Applied Crystallography*, 2 (2): p. 65-61. doi:10.1107/S0021889869006558
- Rose & Associates Multi-Method Risk Analysis (v4-4-051) [software]. (2012). Rose & Associates, LLP.
- Sondergeld, C. H., Ambrose, R. J., Rai, C. S., & Moncrieff, J., 2010, Micro-structural studies of gas shales. SPE-131771, SPE Unconventional Gas Conference, Pittsburgh, PA, February 23-25, 2010.
- Sweeney, J. J. and Burnham, A. K., 1990, Evaluation of a simple model of vitrinite reflectance based on chemical kinetics. *American Association of Petroleum Geologists Bulletin*, 74, p. 1559-1570.
- Telle, W. R., Thompson, D. A., Lottman, L. K., and Malone, P. G., 1987, Preliminary burial-thermal history investigations of the Black Warrior basin: implications for coalbed methane and conventional hydrocarbon development: Tuscaloosa, Alabama, University of Alabama, 1987 Coalbed Methane Symposium Proceedings, p. 37-50.

- Thomas, W. A., 1977, Evolution of Appalachian-Ouachita salients and recesses from reentrants and promontories in the continental margin. *American Journal of Science* **277** (10), p. 1233-1278.
- Thomas, W. A., 1988, *The Black Warrior Basin*, in Sloss, L. L., ed., *Sedimentary cover—North American craton: Geological Society of America*, The Geology of North America, v. D-2, p. 471-492.
- Turekian, K., 1955, Paleocological significance of the strontium-calcium ratio in fossils and sediments. *Geological Society of America Bulletin*, **66** (1), p. 155-158.
- Zhou, L., Zhou, Y., Li, M., Chen, P., & Wang, Y., 2000, Experimental and modeling study of the adsorption of supercritical methane on a high surface activated carbon. *Langmuir*, **16**(14), p. 5955-5959.

APPENDIX

Table A-1: Geochemical data for the Neal shale (from Pashin et al., 2011).

Permit	Top Depth (ft)	Formation	TOC (wt%)	S1(mg/g)	S2 (mg/g)	S3 (mg/g)	Tmax(°C)	HI	OI
2191	2740	Neal	1.71	0.88	4.78	0.34	442	280	20
2191	2780	Neal	4.25	2.52	18.16	0.54	440	427	13
2191	2820	Neal	2.07	0.72	3.97	0.29	441	192	14
2191	2920	Neal	4.19	1.65	15.67	0.49	441	374	12
2191	3010	Floyd	0.46	0.02	0.16	0.3	478	35	65
1780	6270	Neal	0.82	0.05	0.06	0.15	454	7	18
1780	6300	Neal	0.99	0.07	0.27	0.1	465	27	10
1780	6330	Neal	1.87	0.23	0.56	0.29	448	30	16
1780	6340	Neal	1.97	0.45	0.98	0.27	451	50	14
1780	6350	Neal	1.21	0.06	0.17	0.15	451	14	12
1780	6360	Neal	1.13	0.06	0.19	0.1	467	17	9
1780	6370	Neal	1.26	0.06	0.24	0.12	467	19	10
1780	6380	Neal	1.09	0.07	0.23	0.12	468	21	11
1780	6390	Neal	1.54	0.09	0.31	0.07	454	20	5
1780	6410	Neal	1.59	0.12	0.35	0.14	456	22	9
1780	6420	Neal	3.27	0.53	1.28	0.26	454	39	8
1780	6430	Neal	2.59	0.34	0.91	0.12	453	35	5
1780	6440	Neal	2.95	0.67	1.42	0.2	456	48	7
1780	6450	Neal	2.95	0.45	1.21	0.17	457	41	6
1780	6450	Neal	2.42	0.47	1.05	0.28	452	43	12
1780	6460	Neal	3.56	0.58	1.7	0.17	454	48	5
1780	6460	Neal	2.93	0.79	1.72	0.27	455	59	9
1780	6470	Neal	2.89	0.47	1.37	0.13	451	47	4
1780	6470	Neal	2.69	0.62	1.51	0.2	461	56	7
1780	6480	Neal	3.98	0.9	2.44	0.24	456	61	6
1780	6480	Neal	3.73	1.28	3.06	0.29	458	82	8
1780	6490	Neal	4.12	0.29	1.2	0.48	453	29	12
1780	6500	Neal	3.42	0.72	1.94	0.21	458	57	6
1780	6510	Neal	2.04	0.45	1.08	0.07	458	53	3
1780	6550	Neal	2.08	0.08	0.45	0.17	453	22	8
1780	6560	Neal	2.63	0.1	0.49	0.41	436	19	16
15668	9013.45	Neal	2.25	0.21	0.70	0.99	482	31	44
15668	9016.75	Neal	3.96	0.13	0.82	0.40	475	21	10
15668	9020.85	Neal	2.84	0.15	0.69	0.16	468	24	6
15668	9023.05	Neal	3.78	0.25	1.24	0.26	477	33	7
15668	9024.45	Neal	3.80	0.26	1.08	0.15	469	28	4

APPENDIX

Table A-2: XRD results for Well 2191 samples.

Depth (ft)	Formation	Quartz	Albite	Calcite	Chlorite	Dolomite	Fluorite	Illite	Montmorillonite	Muscovite	K-spar	Pyrite	Sum Clay
2740-45	Neal	34.2	4.3	21.3	6.0	6.9	0.0	0.0	3.3	10.7	12.1	1.1	20.0
2750-55	Neal	22.2	2.2	14.7	6.1	10.0	1.2	26.4	0.7	6.9	8.5	1.2	40.0
2760-65	Neal	18.7	4.4	9.5	6.9	16.3	0.0	0.0	0.3	28.0	14.6	1.3	35.2
2770-75	Neal	26.2	3.0	18.3	12.1	9.4	0.0	17.3	0.0	2.5	9.5	1.6	31.9
2780-85	Neal	29.0	3.1	9.8	9.2	3.8	0.2	28.1	0.8	3.7	9.7	2.5	41.7
2790-95	Neal	27.1	3.9	8.2	7.9	2.2	0.5	31.2	0.6	6.7	9.8	1.9	46.3
2800-05	Neal	25.7	2.9	10.7	9.6	2.6	0.0	28.9	0.1	6.4	10.9	2.2	45.1
2810-15	Neal	34.0	7.5	1.5	14.5	1.0	0.0	0.0	0.5	28.9	11.9	0.2	43.9
2820-25	Neal	27.4	3.4	1.7	9.4	1.5	0.0	32.8	2.7	10.4	8.3	2.3	55.3
2830-35	Neal	21.9	4.2	2.6	9.0	2.1	1.0	31.2	4.5	9.7	12.6	1.1	54.4
2840-45	Neal	37.0	1.6	6.0	6.5	1.0	0.0	25.1	1.2	6.7	14.0	1.0	39.5
2850-55	Neal	16.7	7.8	6.9	8.2	3.3	0.0	0.0	1.7	25.6	28.6	1.2	35.5
2860-65	Neal	26.8	4.3	10.2	5.3	3.3	1.7	28.2	1.3	6.1	11.4	1.4	40.9
2870-75	Neal	25.3	4.5	13.8	5.9	3.1	0.0	26.8	0.4	6.7	11.9	1.6	39.8
2880-85	Neal	20.0	3.6	7.4	5.5	1.9	1.5	34.6	2.2	11.5	10.6	1.1	53.8
2890-95	Neal	18.6	1.8	12.7	8.4	3.4	3.8	27.7	0.4	13.1	9.6	0.6	49.6
2900-05	Neal	21.4	2.1	7.6	10.7	2.3	2.4	30.8	0.5	9.6	11.3	1.2	51.7
2910-15	Neal	20.3	1.2	15.2	9.7	1.9	0.4	30.0	1.1	9.8	8.6	1.8	50.5
2920-25	Neal	23.3	2.8	9.9	8.0	1.4	2.6	30.7	1.3	7.6	10.6	1.8	47.6
2930-35	Neal	17.7	3.1	15.9	4.4	18.1	0.0	0.0	0.0	27.6	12.5	0.7	31.9
2940-45	Neal	23.4	4.1	15.3	5.3	4.1	0.0	0.0	0.7	26.1	20.2	0.7	32.1
2950-55	Floyd	51.4	0.0	19.3	7.3	5.7	0.0	0.0	0.5	3.5	11.4	0.9	11.4
2960-65	Floyd	50.1	2.6	1.6	4.3	1.7	0.0	14.1	1.9	11.4	11.9	0.4	31.7
2970-75	Floyd	59.1	2.6	1.1	4.8	0.9	0.3	9.7	1.6	8.4	11.0	0.6	24.4
2980-85	Floyd	69.5	2.2	1.5	7.4	1.0	0.0	0.0	1.5	5.3	11.1	0.5	14.2
2990-95	Floyd	69.5	2.5	1.5	6.2	0.8	0.0	0.0	1.4	6.5	11.2	0.4	14.1
3000-05	Floyd	51.5	1.6	21.2	5.5	5.5	0.0	0.0	1.1	3.7	9.2	0.5	10.4

APPENDIX

Table A-3: XRD results for Well 1780 samples.

Depth (ft)	Formation	Quartz	Albite	Calcite	Chlorite	Dolomite	Fluorite	Illite	Montmorillonite	Muscovite	K-spar	Pyrite	Siderite	Sum Clay
6270-80	Neal	23.3	3.3	22.2	8.2	5.0	0.1	25.4	1.2	5.6	5.3	0.5	0.0	40.4
6280-90	Neal	18.8	4.8	36.2	9.3	4.3	0.0	0.0	0.7	18.8	6.2	0.8	0.0	28.9
6290-00	Neal	14.7	9.8	5.7	11.9	0.8	0.0	0.0	0.1	38.0	18.6	0.4	0.0	50.0
6300-10	Neal	23.3	5.5	6.0	7.4	3.3	0.0	22.2	0.0	22.3	9.7	0.3	0.0	51.9
6310-20	Neal	23.3	3.6	22.4	8.7	7.6	0.9	23.9	0.5	3.8	5.0	0.4	0.0	36.9
6320-30	Neal	23.2	3.4	13.3	8.5	9.8	2.7	29.0	0.5	2.6	6.6	0.4	0.0	40.5
6330-40	Neal	33.0	3.0	13.8	14.4	9.9	0.0	16.3	0.0	4.9	3.2	1.5	0.0	35.6
6340-50	Neal	21.8	8.4	8.3	9.2	7.1	0.0	0.0	0.2	28.6	14.8	1.7	0.0	37.9
6350-60	Neal	25.3	3.9	9.8	9.5	6.9	0.4	26.7	1.2	5.6	9.4	1.4	0.0	42.9
6360-70	Neal	19.3	7.1	3.0	12.7	1.2	0.0	26.8	1.1	3.3	25.1	0.5	0.0	43.9
6370-80	Neal	28.6	3.6	2.6	11.7	1.4	0.0	24.9	0.1	15.9	10.8	0.3	0.0	52.7
6380-90	Neal	30.2	2.7	5.4	11.6	1.5	0.0	33.8	1.6	4.4	8.1	0.7	0.0	51.4
6390-00	Neal	25.4	1.7	0.4	12.6	0.4	2.3	36.2	0.5	10.2	9.4	0.9	0.0	59.5
6400-10	Neal	22.3	3.8	1.4	10.7	1.7	3.4	31.1	0.4	12.6	11.9	0.6	0.0	54.9
6410-20	Neal	23.1	3.4	3.0	9.9	3.2	2.3	32.0	2.4	10.2	9.9	0.6	0.0	54.5
6420-30	Neal	30.5	4.8	2.1	8.1	6.1	1.1	30.1	1.5	4.0	10.8	1.0	0.0	43.7
6430-40	Neal	15.3	7.4	2.0	8.2	6.2	0.0	13.1	13.6	5.2	28.2	0.9	0.0	40.1
6440-50	Neal	32.7	5.5	0.0	9.2	4.4	0.0	28.0	0.1	6.9	12.1	1.2	0.0	44.2
6450-60	Neal	27.8	4.4	3.1	9.2	5.8	0.7	32.0	0.3	7.3	7.8	1.6	0.0	48.9
6460-70	Neal	28.8	5.9	1.1	8.8	7.6	0.6	32.3	0.7	3.4	8.6	2.2	0.0	45.2
6470-80	Neal	25.5	4.4	1.9	10.1	4.8	2.4	37.0	0.4	3.5	8.7	1.2	0.0	51.0
6480-90	Neal	25.9	5.4	0.8	9.7	3.8	1.3	36.5	0.6	6.2	8.3	1.4	0.0	53.1
6490-00	Neal	25.5	5.5	9.0	7.4	4.5	0.0	30.4	0.7	5.5	9.7	1.8	0.0	44.0
6500-10	Neal	28.4	4.2	5.1	11.2	5.0	2.3	30.9	0.4	4.0	6.8	1.7	0.0	46.5
6510-20	Neal	25.4	3.2	18.9	7.7	4.3	0.0	21.1	0.3	8.1	10.0	1.0	0.0	37.2
6520-30	Neal	16.1	4.9	30.9	2.6	7.0	0.0	0.0	11.2	13.2	13.5	0.6	0.0	27.0
6530-40	Neal	35.0	2.1	35.4	5.8	5.4	0.0	0.0	1.9	7.4	6.7	0.5	0.0	15.0
6540-50	Neal	25.5	2.8	15.2	6.4	5.5	2.5	24.6	2.2	6.7	8.2	0.7	0.0	39.8
6550-60	Neal	27.6	3.0	11.8	7.1	5.3	1.8	27.4	1.3	5.0	8.9	0.7	0.0	40.8
6560-70	Neal	28.8	4.3	14.3	7.9	2.3	1.0	22.7	0.9	7.1	7.5	0.6	2.6	38.6

APPENDIX

Table A-4: XRD results for Well 15668 samples.

Depth (ft)	Formation	Quartz	Albite	Calcite	Chlorite	Dolomite	Fluorite	Illite	Montmorillonite	Muscovite	K-spar	Pyrite	Sum Clay
9013.1	Neal	32.3	3.0	0.0	7.9	7.4	0.0	32.1	0.6	5.5	8.8	2.4	46.1
9022.8	Neal	37.0	8.7	0.0	7.8	6.0	0.0	23.1	0.2	2.7	12.3	2.2	33.8
9033.0	Lewis	9.5	6.8	46.6	2.7	18.7	0.0	0.0	1.8	12.3	1.0	0.7	16.7
9044.0	Lewis	1.6	2.0	88.4	4.8	2.7	0.0	0.0	0.1	0.0	0.0	0.5	4.8
9053.0	Neal	17.8	6.0	2.0	7.5	7.4	4.0	31.5	0.0	11.2	11.8	0.8	50.2
9062.7	Lewis	10.8	2.0	79.2	3.8	1.2	0.0	0.0	0.0	2.7	0.0	0.3	6.4
9073.0	Lewis	72.4	1.7	15.2	2.3	2.3	0.0	0.0	2.5	0.0	3.5	0.2	4.8

APPENDIX

Table A-5: XRF results for Well 2191 samples.

Depth (ft)	SiO ₂	TiO ₂	Al ₂ O ₃	Fe ₂ O ₃	MnO	MgO	CaO	Na ₂ O	K ₂ O	P ₂ O ₅
2740-45	63.929	0.543	10.575	3.918	0.030	1.748	16.488	0.538	1.918	0.131
σ	0.053	0.002	0.023	0.003	0.000	0.004	0.009	0.003	0.001	0.001
2750-55	59.049	0.683	15.139	5.897	0.048	2.349	13.194	0.681	2.551	0.209
σ	0.051	0.001	0.029	0.006	0.000	0.010	0.013	0.007	0.005	0.001
2760-65	57.327	0.734	15.854	5.825	0.055	3.187	13.215	0.706	2.723	0.176
σ	0.054	0.001	0.021	0.002	0.000	0.009	0.012	0.003	0.006	0.000
2770-75	57.767	0.714	15.077	5.876	0.043	2.403	14.176	0.713	2.768	0.235
σ	0.011	0.002	0.010	0.004	0.000	0.004	0.005	0.003	0.003	0.001
2780-85	62.089	0.778	16.812	6.548	0.033	2.033	7.500	0.750	2.999	0.215
σ	0.059	0.003	0.015	0.002	0.000	0.004	0.005	0.005	0.007	0.001
2790-95	63.007	0.874	17.850	5.999	0.032	1.964	5.931	0.778	3.163	0.160
σ	0.062	0.002	0.026	0.002	0.000	0.005	0.009	0.004	0.006	0.000
2800-05	60.747	0.842	18.344	6.657	0.033	2.120	6.949	0.834	3.059	0.180
σ	0.125	0.002	0.047	0.005	0.000	0.011	0.008	0.005	0.006	0.001
2810-15	64.975	0.835	20.393	5.816	0.023	1.987	1.857	0.938	2.904	0.111
σ	0.312	0.001	0.086	0.007	0.000	0.006	0.004	0.005	0.007	0.001
2820-25	63.791	0.794	19.727	6.848	0.037	2.017	2.747	0.879	2.875	0.121
σ	0.097	0.002	0.043	0.007	0.000	0.003	0.003	0.006	0.004	0.001
2830-35	64.727	0.817	19.733	5.671	0.029	1.930	3.025	0.888	2.885	0.125
σ	0.050	0.004	0.018	0.004	0.000	0.005	0.005	0.007	0.005	0.000
2840-45	64.998	0.797	17.934	5.829	0.029	1.785	4.838	0.810	2.666	0.152
σ	0.034	0.002	0.008	0.004	0.000	0.005	0.004	0.003	0.006	0.000
2850-55	62.951	0.797	16.641	5.580	0.033	1.819	8.291	0.714	2.789	0.197
σ	0.116	0.003	0.035	0.002	0.000	0.008	0.011	0.008	0.002	0.001
2860-65	63.107	0.802	16.171	5.807	0.029	1.773	8.418	0.697	2.740	0.253
σ	0.069	0.002	0.035	0.005	0.000	0.005	0.008	0.004	0.008	0.001
2870-75	60.100	0.862	16.226	6.223	0.032	1.891	10.561	0.698	2.947	0.229
σ	0.045	0.002	0.028	0.002	0.000	0.009	0.006	0.008	0.005	0.001
2880-85	60.902	0.918	19.217	6.484	0.033	1.981	5.981	0.800	3.280	0.184
σ	0.060	0.004	0.006	0.004	0.000	0.005	0.006	0.006	0.007	0.000
2890-95	55.622	0.817	19.012	8.676	0.065	2.224	9.699	0.692	2.872	0.150
σ	0.034	0.002	0.022	0.004	0.000	0.011	0.011	0.003	0.004	0.000
2900-05	59.854	0.890	20.686	6.955	0.038	1.964	5.339	0.770	3.191	0.129
σ	0.145	0.002	0.062	0.006	0.000	0.008	0.004	0.003	0.004	0.001
2910-15	56.756	0.830	18.597	6.761	0.042	2.204	10.576	0.702	3.195	0.139
σ	0.136	0.003	0.057	0.005	0.000	0.005	0.011	0.006	0.004	0.001
2920-25	59.753	0.844	18.186	7.786	0.048	1.976	6.915	0.750	3.290	0.231
σ	0.134	0.001	0.056	0.005	0.000	0.005	0.005	0.005	0.004	0.001

(σ denotes standard deviation)

APPENDIX

Table A-5, continued: XRF results for Well 2191

Depth (ft)	SiO ₂	TiO ₂	Al ₂ O ₃	Fe ₂ O ₃	MnO	MgO	CaO	Na ₂ O	K ₂ O	P ₂ O ₅
2930-35	53.345	0.571	11.648	6.385	0.079	3.725	21.476	0.435	2.093	0.103
σ	0.117	0.002	0.034	0.004	0.000	0.011	0.014	0.005	0.003	0.001
2940-45	63.455	0.599	12.859	4.462	0.046	1.629	13.966	0.436	2.324	0.100
σ	0.049	0.002	0.023	0.004	0.000	0.006	0.007	0.004	0.004	0.000
2950-55	65.692	0.565	11.702	5.732	0.059	1.617	12.205	0.361	1.855	0.095
σ	0.059	0.001	0.013	0.006	0.000	0.004	0.014	0.002	0.005	0.000
2960-65	78.166	0.644	12.392	3.158	0.026	0.994	2.343	0.310	1.761	0.086
σ	0.293	0.004	0.033	0.004	0.000	0.001	0.004	0.003	0.005	0.000
2970-75	83.192	0.480	9.577	2.609	0.019	0.746	1.597	0.283	1.308	0.084
σ	0.147	0.001	0.020	0.002	0.000	0.005	0.003	0.002	0.003	0.001
2980-85	87.648	0.309	6.760	2.086	0.015	0.563	1.412	0.224	0.851	0.060
σ	0.072	0.002	0.006	0.002	0.000	0.004	0.004	0.004	0.002	0.000
2990-95	88.911	0.358	5.770	1.947	0.015	0.470	1.473	0.162	0.743	0.061
σ	0.069	0.001	0.005	0.001	0.000	0.001	0.003	0.005	0.002	0.001
3000-05	71.257	0.326	6.453	3.351	0.134	1.128	15.881	0.214	1.012	0.151
σ	0.036	0.002	0.006	0.003	0.000	0.004	0.016	0.003	0.002	0.000

(σ denotes standard deviation)

APPENDIX

Table A-6: XRF results for Well 1780 samples

Depth (ft)	SiO ₂	TiO ₂	Al ₂ O ₃	Fe ₂ O ₃	MnO	MgO	CaO	Na ₂ O	K ₂ O	P ₂ O ₅
6270-80	54.452	0.924	16.470	6.180	0.039	2.124	16.049	0.920	2.533	0.148
σ	0.094	0.002	0.039	0.004	0.000	0.007	0.005	0.009	0.004	0.001
6280-90	46.115	0.799	13.898	5.624	0.048	1.992	28.274	0.798	2.093	0.189
σ	0.067	0.003	0.027	0.001	0.000	0.003	0.005	0.007	0.003	0.001
6290-00	58.951	0.990	20.360	6.818	0.053	2.105	6.107	0.821	3.468	0.159
σ	0.089	0.002	0.045	0.004	0.000	0.009	0.004	0.003	0.006	0.001
6300-10	58.946	0.920	18.880	8.284	0.146	2.067	6.625	0.860	2.798	0.305
σ	0.278	0.001	0.064	0.011	0.000	0.008	0.007	0.007	0.006	0.002
6310-20	53.668	0.856	16.314	6.950	0.068	2.092	16.261	0.866	2.391	0.374
σ	0.026	0.002	0.013	0.005	0.000	0.005	0.005	0.006	0.002	0.001
6320-30	56.263	0.870	17.113	7.428	0.099	2.217	11.869	0.912	2.441	0.625
σ	0.043	0.002	0.019	0.006	0.000	0.004	0.010	0.013	0.005	0.001
6330-40	57.627	0.877	17.272	6.764	0.084	2.108	10.811	0.995	2.574	0.699
σ	0.044	0.003	0.025	0.001	0.000	0.005	0.010	0.010	0.004	0.001
6340-50	59.117	0.876	17.796	6.317	0.054	2.059	9.601	0.829	2.558	0.596
σ	0.066	0.003	0.018	0.003	0.000	0.004	0.004	0.007	0.004	0.001
6350-60	59.560	0.931	18.126	6.075	0.047	1.994	9.174	0.830	2.618	0.456
σ	0.025	0.001	0.019	0.005	0.000	0.008	0.005	0.007	0.002	0.001
6360-70	62.721	1.012	19.853	7.607	0.039	1.883	2.932	0.858	2.738	0.198
σ	0.038	0.002	0.036	0.004	0.000	0.006	0.003	0.005	0.005	0.000
6370-80	61.830	1.001	19.810	7.894	0.048	1.939	3.540	0.842	2.737	0.191
σ	0.021	0.002	0.021	0.003	0.000	0.006	0.005	0.003	0.005	0.001
6380-90	61.488	1.001	19.833	7.543	0.043	1.960	4.160	0.823	2.776	0.206
σ	0.045	0.002	0.017	0.003	0.000	0.006	0.003	0.003	0.004	0.001
6390-00	61.423	0.980	22.035	8.144	0.073	1.800	1.441	0.808	2.991	0.131
σ	0.064	0.002	0.043	0.005	0.000	0.003	0.003	0.001	0.003	0.001
6400-10	61.137	0.979	21.530	7.965	0.098	1.823	2.370	0.834	2.967	0.128
σ	0.072	0.003	0.031	0.005	0.000	0.005	0.002	0.005	0.006	0.001
6410-20	60.317	0.953	19.710	8.644	0.081	1.957	4.116	0.899	2.907	0.233
σ	0.147	0.002	0.066	0.005	0.000	0.004	0.007	0.006	0.005	0.000
6420-30	64.380	0.836	17.100	6.707	0.059	2.085	4.272	0.894	3.008	0.440
σ	0.159	0.004	0.048	0.003	0.000	0.003	0.004	0.007	0.008	0.001
6430-40	61.780	0.871	18.772	7.020	0.070	2.368	4.428	0.893	3.259	0.330
σ	0.183	0.002	0.064	0.006	0.000	0.008	0.002	0.011	0.004	0.002
6440-50	62.142	0.884	18.691	7.870	0.084	2.087	3.599	0.876	3.222	0.335
σ	0.243	0.001	0.085	0.006	0.000	0.009	0.003	0.006	0.004	0.001
6450-60	64.803	0.857	18.215	5.796	0.044	2.023	3.668	0.883	3.219	0.275
σ	0.253	0.003	0.048	0.006	0.000	0.005	0.005	0.007	0.008	0.002

(σ denotes standard deviation)

APPENDIX

Table A-6, continued: XRF results for Well 1780 samples

Depth (ft)	SiO ₂	TiO ₂	Al ₂ O ₃	Fe ₂ O ₃	MnO	MgO	CaO	Na ₂ O	K ₂ O	P ₂ O ₅
6460-70	63.617	0.857	18.041	6.618	0.053	2.170	3.713	0.944	3.259	0.498
σ	0.049	0.003	0.027	0.005	0.000	0.006	0.003	0.005	0.003	0.001
6470-80	62.534	0.928	19.455	7.000	0.066	2.005	3.314	0.915	3.160	0.416
σ	0.035	0.001	0.026	0.004	0.000	0.005	0.008	0.007	0.005	0.001
6480-90	62.511	0.974	19.910	6.744	0.051	2.051	2.787	0.950	3.515	0.265
σ	0.067	0.001	0.026	0.007	0.000	0.008	0.007	0.008	0.008	0.001
6490-00	61.279	0.892	17.731	5.915	0.053	2.168	7.142	0.879	3.285	0.389
σ	0.109	0.002	0.014	0.001	0.000	0.008	0.007	0.011	0.003	0.001
6500-10	61.444	0.865	18.158	8.051	0.095	2.042	5.172	0.770	2.845	0.341
σ	0.088	0.001	0.018	0.006	0.000	0.004	0.007	0.008	0.002	0.002
6510-20	54.704	0.893	17.084	6.689	0.112	1.857	14.799	0.813	2.670	0.190
σ	0.091	0.002	0.026	0.005	0.000	0.006	0.017	0.004	0.005	0.000
6520-30	51.653	0.441	7.332	3.617	0.105	1.365	33.618	0.327	1.314	0.104
σ	3.323	0.002	0.010	0.004	0.001	0.005	0.019	0.002	0.004	0.001
6530-40	56.800	0.490	8.098	4.449	0.115	1.406	26.731	0.372	1.251	0.160
σ	4.631	0.003	0.006	0.005	0.001	0.005	0.024	0.003	0.004	0.001
6540-50	56.072	0.778	16.499	8.607	0.191	2.024	12.559	0.563	2.332	0.217
σ	0.913	0.003	0.022	0.004	0.001	0.004	0.008	0.005	0.003	0.001
6550-60	61.401	0.809	15.786	6.865	0.135	1.813	9.651	0.610	2.520	0.242
σ	0.141	0.002	0.047	0.006	0.000	0.008	0.007	0.004	0.002	0.001
6560-70	59.054	0.789	15.668	8.203	0.140	1.824	10.937	0.608	2.470	0.151
σ	1.964	0.001	0.027	0.005	0.000	0.004	0.009	0.005	0.006	0.001

(σ denotes standard deviation)

APPENDIX

Table A-7: XRF results for Well 15668 samples.

Depth (ft)	SiO ₂	TiO ₂	Al ₂ O ₃	Fe ₂ O ₃	MnO	MgO	CaO	Na ₂ O	K ₂ O	P ₂ O ₅
9013.0	63.229	0.870	19.978	5.889	0.025	2.304	2.723	0.944	3.704	0.106
σ	0.149	0.001	0.257	0.002	0.000	0.013	0.004	0.006	0.008	0.001
9022.8	66.876	0.900	15.584	5.195	0.030	1.651	4.830	0.933	3.276	0.428
σ	2.066	0.002	0.146	0.003	0.000	0.022	0.009	0.010	0.007	0.002
9033.0	15.444	0.382	4.345	2.645	0.049	4.314	71.100	0.504	0.969	0.085
σ	0.036	0.002	0.055	0.003	0.000	0.010	0.018	0.007	0.002	0.000
9044.0	3.237	0.052	0.511	0.627	0.042	0.884	94.094	0.081	0.130	0.174
σ	0.030	0.001	0.002	0.001	0.000	0.005	0.053	0.003	0.001	0.001
9053.0	63.565	0.859	19.606	4.596	0.019	2.020	4.503	0.672	3.871	0.152
σ	0.048	0.002	0.021	0.005	0.000	0.005	0.002	0.004	0.006	0.000
9062.7	12.685	0.084	1.142	0.575	0.056	0.704	84.170	0.123	0.174	0.179
σ	0.008	0.002	0.003	0.001	0.001	0.003	0.036	0.002	0.001	0.001
9073.0	86.754	0.027	0.157	0.612	0.015	0.355	11.848	0.132	0.020	0.039
σ	0.093	0.000	0.002	0.000	0.000	0.003	0.004	0.002	0.001	0.000

(σ denotes standard deviation)

APPENDIX

Table A-8: XRF trace element data for samples from Well 2191.

Depth (ft)	Formation	V	Cr	Ni	Cu	Zn	Rb	Sr	Y	Zr	Nb	Ba	Mo	U
2740-45	Neal	120.09	184.16	59.38	22.77	124.56	91.30	725.92	28.57	134.60	8.93	300.68	6.03	3.35
σ		3.38	2.61	0.40	1.02	0.80	0.40	0.80	0.49	0.49	0.63	10.98	0.49	0.00
2750-55	Neal	172.33	251.09	73.00	28.32	163.93	121.45	563.23	34.51	141.36	11.28	438.91	7.96	4.42
σ		1.47	1.79	0.63	0.49	0.75	0.40	1.33	0.75	0.40	0.40	11.34	0.40	0.00
2760-65	Neal	215.77	252.80	75.17	26.83	181.17	130.17	540.86	35.70	148.80	11.75	334.85	8.87	4.44
σ		3.26	3.03	1.17	0.98	1.50	0.49	0.98	0.40	0.40	0.49	16.02	0.00	0.00
2770-75	Neal	211.91	351.17	90.21	34.19	197.52	126.20	547.11	39.14	148.48	11.47	526.41	10.35	4.50
σ		2.42	1.72	0.75	0.80	1.02	0.40	1.36	0.40	0.00	0.40	22.51	0.40	0.00
2780-85	Neal	285.61	448.34	111.97	42.52	252.67	133.79	427.42	45.19	152.71	12.24	491.31	14.69	4.45
σ		2.15	2.04	1.50	0.40	1.10	0.40	0.63	0.49	0.40	0.00	11.25	0.40	0.00
2790-95	Neal	307.87	454.37	115.42	43.95	229.07	142.06	371.79	40.84	171.58	14.65	505.20	14.43	4.44
σ		1.62	3.32	0.63	0.49	1.50	0.63	0.89	0.40	0.80	0.40	19.81	0.00	0.00
2800-05	Neal	260.68	350.17	95.75	34.59	184.35	146.85	382.98	41.29	159.13	13.84	660.84	10.04	4.46
σ		2.42	1.17	0.40	0.63	0.75	0.49	0.75	0.63	0.49	0.49	9.28	0.00	0.00
2810-15	Neal	181.64	303.77	77.93	24.93	134.29	138.69	247.84	33.31	172.84	14.46	272.77	5.87	4.19
σ		2.58	2.76	0.49	0.40	0.40	0.49	0.49	0.40	0.00	0.40	12.74	0.49	0.00
2820-25	Neal	172.48	296.21	78.36	26.05	131.51	137.39	256.09	32.56	161.97	14.08	326.88	5.88	4.20
σ		3.60	1.26	1.36	0.98	0.75	0.40	0.75	0.00	0.75	0.49	6.94	0.49	0.00
2830-35	Neal	179.10	337.24	84.26	31.76	153.06	136.76	271.19	33.03	160.89	14.82	289.40	6.56	4.23
σ		1.33	1.74	0.80	0.63	1.36	0.40	0.40	0.98	0.00	0.00	8.48	0.40	0.00
2840-45	Neal	161.72	295.79	75.97	28.51	139.38	126.19	287.06	34.69	178.96	13.62	272.38	6.38	4.26
σ		3.16	2.45	0.80	0.40	1.10	0.49	0.98	0.49	0.40	0.40	9.88	0.00	0.00
2850-55	Neal	186.15	344.33	89.49	35.13	171.16	129.54	347.46	39.38	188.61	13.65	315.02	8.95	4.47
σ		1.02	3.31	0.63	0.49	0.00	0.75	1.02	0.40	0.49	0.40	4.96	0.00	0.00
2860-65	Neal	203.25	394.07	99.52	41.10	195.26	119.73	358.08	45.32	192.37	13.33	356.97	12.22	4.44
σ		2.76	2.14	1.02	0.63	1.17	0.40	0.49	0.75	0.40	0.00	20.77	0.00	0.00
2870-75	Neal	244.81	445.53	111.38	49.61	231.26	128.15	413.38	50.52	194.29	14.01	391.56	13.78	4.59
σ		1.47	1.26	0.63	0.98	0.49	1.02	0.89	0.63	0.75	0.40	14.87	0.00	0.00
2880-85	Neal	225.02	325.40	93.48	37.84	174.05	158.70	432.46	41.18	187.63	15.14	489.22	7.79	4.45
σ		1.83	0.80	1.10	0.63	0.49	0.80	0.49	0.63	1.02	0.49	9.07	0.00	0.00
2890-95	Neal	200.22	226.52	70.65	24.13	131.96	142.17	431.09	37.83	147.61	13.70	267.17	5.65	4.35
σ		2.14	3.61	0.63	0.75	1.02	0.40	1.02	0.40	0.40	0.49	11.72	0.40	0.00
2900-05	Neal	230.39	293.73	87.61	30.23	152.05	161.10	342.72	37.96	155.58	15.45	329.48	6.62	4.41
σ		2.04	2.64	0.49	1.02	1.17	0.00	0.49	0.49	0.00	0.00	11.57	0.00	0.00
2910-15	Neal	195.78	318.39	83.32	30.48	164.16	155.58	450.04	36.81	156.94	13.55	360.84	7.90	4.52
σ		2.33	2.97	0.40	1.10	0.49	0.40	1.20	0.80	0.63	0.00	9.89	0.00	0.00
2920-25	Neal	211.70	433.26	112.01	45.92	232.76	147.41	318.56	41.22	178.10	14.56	454.32	10.98	4.48
σ		2.10	2.14	0.63	0.89	1.60	0.49	0.80	0.75	0.63	0.00	12.94	0.40	0.00
2930-35	Neal	107.14	155.15	50.56	31.54	119.43	94.85	357.61	23.42	173.93	9.51	275.74	6.96	3.48
σ		1.74	2.40	0.80	0.40	0.63	0.75	1.02	0.40	0.00	0.40	9.50	0.00	0.00
2940-45	Neal	91.07	113.45	37.37	23.50	71.38	97.56	287.54	25.06	222.87	9.62	242.57	4.48	3.36
σ		0.80	2.06	0.49	0.63	0.75	0.40	0.63	0.49	0.75	0.49	8.93	0.00	0.00

(σ denotes standard deviation)

APPENDIX

Table A-8, continued: XRF trace element data for samples from Well 2191.

Depth (ft)	Formation	V	Cr	Ni	Cu	Zn	Rb	Sr	Y	Zr	Nb	Ba	Mo	U
2950-55	Floyd	90.07	109.21	44.36	29.95	72.73	83.99	263.91	24.99	209.64	9.68	205.59	5.63	3.38
	σ	1.67	1.41	1.02	0.49	0.80	0.49	0.49	0.40	0.40	0.80	7.76	0.00	0.00
2960-65	Floyd	77.62	98.92	33.96	20.88	60.32	68.34	117.27	27.42	376.06	9.49	318.48	3.16	3.16
	σ	2.87	2.40	0.40	0.75	0.40	0.40	0.40	0.00	0.49	0.00	7.13	0.00	0.00
2970-75	Floyd	64.62	107.22	28.75	18.04	52.03	50.36	98.40	21.61	323.75	7.34	274.02	4.20	3.15
	σ	1.36	1.72	0.49	0.40	0.49	0.00	0.40	0.49	0.80	0.00	12.66	0.00	0.00
2980-85	Floyd	47.06	67.47	22.28	16.03	29.57	37.69	82.05	13.54	166.81	6.46	220.74	4.16	3.12
	σ	0.75	1.60	0.49	1.02	0.49	0.40	0.40	0.00	0.40	0.40	11.56	0.00	0.00
2990-95	Floyd	43.25	82.34	20.79	17.05	27.03	29.73	74.85	17.67	331.01	5.20	249.92	4.16	3.12
	σ	0.80	1.83	0.63	0.49	0.00	0.49	0.63	0.00	0.49	0.00	7.61	0.00	0.00
3000-05	Floyd	51.79	75.87	26.12	19.53	37.02	44.75	235.10	18.40	178.08	6.13	185.81	39.98	3.41
	σ	1.85	1.94	0.63	1.17	0.49	0.49	0.63	0.40	0.40	0.49	7.47	0.40	0.00

(σ denotes standard deviation)

APPENDIX

Table A-9: XRF trace element data for samples from Well 1780.

Depth (ft)	Formation	V	Cr	Ni	Cu	Zn	Rb	Sr	Y	Zr	Nb	Ba	Mo	U
6270-80	Neal	142.60	125.72	53.09	29.99	126.39	149.71	434.03	40.20	195.69	15.77	282.99	4.22	4.44
σ		2.15	2.23	1.17	0.63	1.17	0.40	0.98	0.40	0.40	0.75	10.85	0.40	0.00
6280-90	Neal	124.76	129.30	50.45	28.63	115.21	125.67	643.78	39.77	175.20	13.18	234.29	5.68	4.54
σ		1.83	0.75	0.49	1.17	0.49	0.49	1.36	0.63	0.40	0.49	4.83	0.00	0.00
6290-00	Neal	151.50	147.02	65.51	49.72	123.12	183.08	295.75	40.76	176.68	17.07	420.36	4.27	4.27
σ		2.53	1.94	0.49	0.49	0.49	0.49	0.75	0.40	0.49	0.00	8.67	0.00	0.00
6300-10	Neal	139.31	158.82	63.53	32.18	139.10	154.88	346.51	48.37	183.74	15.57	385.33	5.19	4.15
σ		1.33	1.26	1.33	0.89	1.10	0.98	1.33	0.80	0.63	0.00	16.39	0.00	0.00
6310-20	Neal	135.62	182.43	62.26	30.91	140.85	137.80	445.40	45.93	182.64	14.15	213.77	5.44	4.35
σ		1.36	1.74	0.75	0.80	1.02	0.49	0.40	0.40	0.75	0.00	4.72	0.00	0.00
6320-30	Neal	135.58	181.78	62.66	31.65	139.65	137.29	412.31	50.47	188.40	14.33	258.12	5.77	4.28
σ		2.32	2.61	2.06	1.20	1.02	0.49	0.49	0.40	0.40	0.49	8.31	0.49	0.00
6330-40	Neal	178.51	246.65	78.81	37.88	189.62	140.63	456.52	56.82	188.31	14.15	289.11	8.49	4.35
σ		3.41	1.85	0.80	0.75	0.40	0.75	0.80	0.40	0.63	0.00	11.20	0.40	0.00
6340-50	Neal	203.80	261.38	81.04	35.20	199.67	132.75	464.31	51.06	190.11	14.34	315.70	8.69	4.35
σ		3.01	2.58	1.02	0.80	0.98	0.40	0.49	0.00	0.63	0.40	10.13	0.00	0.00
6350-60	Neal	197.46	235.57	75.35	32.36	179.95	141.61	441.89	50.08	200.34	15.73	305.60	7.76	4.43
σ		2.56	2.58	0.89	0.40	1.36	0.75	0.75	0.75	0.40	0.40	10.57	0.00	0.00
6360-70	Neal	159.38	159.59	65.20	30.90	137.86	164.28	287.86	49.43	196.88	17.90	314.28	4.69	4.26
σ		3.38	1.47	0.98	0.89	0.49	0.40	0.75	0.49	0.40	0.40	8.79	0.49	0.00
6370-80	Neal	164.73	167.08	66.53	33.37	139.91	163.23	315.55	45.78	196.18	17.11	344.65	4.92	4.28
σ		1.10	2.32	0.98	0.40	1.33	0.49	0.63	0.40	1.02	0.00	6.55	0.49	0.00
6380-90	Neal	170.84	169.11	66.78	34.47	142.23	163.26	330.63	47.48	197.51	17.56	320.88	4.99	4.34
σ		2.58	2.68	0.49	0.75	0.98	0.49	0.63	0.75	0.40	0.40	12.96	0.49	0.00
6390-00	Neal	212.74	222.23	75.87	33.63	155.62	171.14	257.58	43.76	171.58	17.89	361.04	5.39	4.31
σ		1.50	2.23	0.80	0.40	0.80	0.75	1.10	0.49	0.40	0.49	5.69	0.00	0.00
6400-10	Neal	211.05	207.37	72.95	33.55	149.57	168.62	265.16	45.46	175.55	17.10	344.17	5.19	4.33
σ		3.22	2.42	0.49	0.63	0.75	0.75	0.00	0.63	0.75	0.40	4.90	0.40	0.00
6410-20	Neal	193.88	241.97	78.03	37.60	170.05	162.40	314.53	48.31	182.73	17.05	362.18	5.46	4.37
σ		1.50	1.50	1.02	1.20	0.49	0.80	1.17	0.40	0.75	0.49	17.57	0.00	0.00
6420-30	Neal	199.43	420.58	104.93	46.49	243.10	139.90	359.97	48.88	167.06	14.34	411.46	9.12	4.34
σ		2.24	4.49	0.80	0.40	0.98	0.75	1.36	0.00	0.75	0.75	13.20	0.49	0.00
6430-40	Neal	196.68	366.37	97.03	43.29	212.56	156.86	348.10	46.78	166.87	15.01	422.29	8.05	4.35
σ		2.79	1.94	0.75	0.98	1.02	0.40	0.63	0.63	0.49	0.40	8.38	0.49	0.00
6440-50	Neal	201.41	368.16	99.62	45.12	221.25	159.99	333.72	54.06	174.82	15.26	411.98	8.72	4.36
σ		2.79	3.87	1.50	1.02	0.00	0.40	0.98	0.49	0.49	0.63	7.13	0.00	0.00
6450-60	Neal	200.92	408.24	107.29	47.78	250.83	149.94	348.52	44.36	171.27	14.72	413.36	10.02	4.27
σ		1.85	3.49	0.49	0.40	0.98	0.49	0.98	0.49	0.49	0.75	14.15	0.49	0.00
6460-70	Neal	201.58	432.90	109.30	52.39	253.53	151.99	392.80	55.62	175.49	14.66	426.01	10.78	4.31
σ		1.26	1.85	0.80	1.02	1.17	0.00	1.02	0.49	0.40	0.49	21.61	0.00	0.00
6470-80	Neal	196.06	342.84	93.64	45.64	220.49	158.99	349.26	51.85	185.13	16.07	397.47	8.57	4.29
σ		2.10	2.10	1.36	0.49	0.75	0.49	0.63	0.49	0.75	0.00	16.37	0.00	0.00
6480-90	Neal	241.90	451.04	118.09	57.62	285.67	171.09	361.98	52.34	197.26	16.71	459.84	12.32	4.40
σ		2.61	2.93	1.50	0.80	0.98	0.49	0.75	0.49	0.49	0.40	19.29	0.40	0.00
6490-00	Neal	235.71	607.93	148.13	69.71	344.07	151.26	405.95	52.28	188.12	14.52	434.33	15.42	4.47
σ		1.67	3.43	0.80	0.49	0.63	0.49	0.49	0.40	1.02	0.00	13.73	0.40	0.00

(σ denotes standard deviation)

APPENDIX

Table A-9, continued: XRF trace element data for samples from Well 1780.

Depth (ft)	Formation	V	Cr	Ni	Cu	Zn	Rb	Sr	Y	Zr	Nb	Ba	Mo	U
6500-10	Neal	200.24	402.01	119.54	55.84	244.31	141.35	354.68	49.73	173.63	14.83	407.03	10.91	4.36
	σ	2.06	3.44	1.36	0.75	1.10	0.80	0.40	0.49	0.75	0.49	4.62	0.00	0.00
6510-20	Neal	189.94	285.60	83.24	38.86	180.97	144.18	380.80	43.92	180.05	15.18	317.79	7.59	4.60
	σ	2.99	3.07	1.02	0.40	1.02	0.80	1.17	0.40	0.49	0.40	14.84	0.49	0.00
6520-30	Neal	69.73	113.36	36.90	24.67	81.56	61.98	434.69	22.84	200.02	6.52	171.27	5.10	3.06
	σ	3.44	1.72	0.75	0.40	1.41	0.75	0.80	0.49	0.40	0.49	21.23	0.00	0.00
6530-40	Neal	68.11	94.54	33.60	26.88	70.57	57.58	384.22	25.99	282.28	6.72	224.48	5.15	3.36
	σ	1.17	1.85	1.26	0.63	0.63	0.49	0.89	0.40	1.10	0.63	9.97	0.49	0.00
6540-50	Neal	139.47	185.45	61.82	33.22	134.41	120.11	360.56	45.32	200.85	12.54	269.05	5.50	4.40
	σ	3.25	1.36	1.94	0.98	0.40	0.40	0.75	0.40	0.49	0.49	5.68	0.00	0.00
6550-60	Neal	145.54	195.98	104.66	37.11	143.54	130.21	350.86	42.00	220.43	13.55	291.31	8.67	4.44
	σ	1.90	3.50	0.75	0.49	0.75	0.75	0.40	0.40	0.49	0.40	9.26	0.40	0.00
6560-70	Neal	119.24	143.23	59.62	38.66	141.60	132.98	339.09	45.41	210.53	16.07	325.12	5.82	4.66
	σ	2.42	2.76	1.17	0.75	1.02	0.40	0.40	0.63	0.40	0.40	20.44	0.00	0.00

(σ denotes standard deviation)

Table A-10: XRF trace element data for samples from Well 15668.

Depth (ft)	Formation	V	Cr	Ni	Cu	Zn	Rb	Sr	Y	Zr	Nb	Ba	Mo	U
9013.0	Neal	209.96	589.39	106.84	45.39	187.39	180.17	415.51	34.92	175.51	14.90	317.27	10.47	4.66
	σ	1.36	3.72	0.75	0.63	0.63	0.40	1.10	0.00	0.40	0.40	10.74	0.00	0.00
9022.8	Neal	215.05	778.13	163.86	92.84	460.46	152.31	377.40	56.21	210.53	16.06	432.10	21.33	5.02
	σ	3.14	1.72	0.49	0.63	0.63	0.49	0.75	0.75	0.40	0.40	3.61	0.00	0.00
9033.0	Lewis	63.70	48.03	47.02	18.45	160.01	41.71	1019.21	15.67	154.70	5.31	60.67	11.38	3.79
	σ	1.50	1.26	1.33	0.80	0.49	0.00	0.80	0.49	0.49	0.75	13.96	0.00	0.00
9044.0	Lewis	14.30	0.00	11.30	12.69	42.44	8.53	1370.72	9.23	90.18	-1.15	93.41	4.61	3.46
	σ	2.24	2.40	1.60	1.55	1.47	0.49	1.36	0.63	0.75	0.63	21.15	0.63	0.00
9053.0	Neal	121.26	134.25	60.11	23.46	141.79	189.33	288.81	28.48	145.35	16.55	231.43	5.24	4.19
	σ	1.94	1.33	0.80	0.80	1.20	0.75	0.75	0.40	0.40	0.40	15.72	0.00	0.00
9062.7	Lewis	22.04	25.36	13.75	19.44	34.84	8.06	745.41	20.86	64.70	0.71	130.36	5.69	3.56
	σ	3.44	1.02	1.02	0.49	1.20	0.40	1.10	0.80	0.80	0.49	13.61	0.75	0.00
9073.0	Neal	6.61	0.00	7.30	10.95	7.98	2.05	317.29	3.19	22.81	3.19	36.50	4.56	3.42
	σ	0.98	1.47	0.49	0.49	0.63	0.40	0.75	0.40	0.00	0.75	2.10	0.00	0.00

(σ denotes standard deviation)

APPENDIX

Table A-11: Uniaxial strength test results for Well 15668 core samples.

Top Depth	Formation	Test	D (mm)	L (mm)	W (mm)	psi	Load (N)	Is, MPa	F	Is(50), MPa
9016.9	Neal	d	24.5	8.3	-	40	478.28	0.80	0.73	0.58
9016.9	Neal	d	24.5	11.5	-	60	717.42	1.20	0.73	0.87
9016.9	Neal	d	24.5	8.0	-	20	239.14	0.40	0.73	0.29
9021.0	Neal	d	24.5	10.5	-	80	956.55	1.59	0.73	1.16
9021.0	Neal	d	24.5	16.0	-	80	956.55	1.59	0.73	1.16
9022.8	Neal	d	24.5	16.8	-	20	239.14	0.40	0.73	0.29
9022.8	Neal	d	24.5	5.3	-	40	478.28	0.80	0.73	0.58
9024.2	Neal	d	24.5	9.5	-	80	956.55	1.59	0.73	1.16
9024.2	Neal	d	24.5	17.3	-	75	896.77	1.49	0.73	1.08
9033.5	Lewis	d	24.5	22.0	-	975	11658.01	19.42	0.73	14.09
9044.6	Lewis	d	24.5	23.3	-	675	8070.93	13.45	0.73	9.75
9062.9	Lewis	d	24.5	17.3	-	2025	24212.79	40.34	0.73	29.26
9073.0	Lewis	d	24.5	19.0	-	2475	29593.41	49.30	0.73	35.76
9013.0	Neal	a	9.5	-	24.5	100	1195.69	4.03	0.47	1.91
9013.0	Neal	a	11.5	-	24.5	120	1434.83	4.00	0.52	2.06
9013.0	Neal	a	5	-	24.5	100	1195.69	7.67	0.35	2.72
9013.0	Neal	a	8	-	24.5	120	1434.83	5.75	0.44	2.52
9014.0	Neal	a	10	-	24.5	140	1673.97	5.37	0.48	2.60
9014.0	Neal	a	8.5	-	24.5	160	1913.11	7.22	0.45	3.25
9016.9	Neal	a	16.5	-	24.5	220	2630.53	5.11	0.61	3.10
9016.9	Neal	a	6	-	24.5	80	956.55	5.11	0.39	1.97
9016.9	Neal	a	12	-	24.5	220	2630.53	7.03	0.53	3.70
9016.9	Neal	a	9	-	24.5	220	2630.53	9.37	0.46	4.33
9016.9	Neal	a	12	-	24.5	260	3108.80	8.30	0.53	4.37
9016.9	Neal	a	6	-	24.5	120	1434.83	7.67	0.39	2.95
9021.06	Neal	a	9.5	-	24.5	220	2630.53	8.88	0.47	4.20
9021.0	Neal	a	7	-	24.5	80	956.55	4.38	0.41	1.81
9021.0	Neal	a	11	-	24.5	180	2152.25	6.27	0.51	3.17
9021.1	Neal	a	14	-	24.5	280	3347.94	7.67	0.56	4.32
9021.0	Neal	a	13	-	24.5	160	1913.11	4.72	0.55	2.57
9021.0	Neal	a	20	-	24.5	440	5261.05	8.43	0.66	5.58

d: diametral test; a: axial test; i: irregular lump; D: distance between platen contact points; L: length of the sample measured from the platen contact point to the edge of the sample; W: width; psi: pounds per square inch; N: load measured in Newton; Is: index strength; MPa: Mega-Pascal; F: correction factor; Is(50): index strength normalized to D=50mm

APPENDIX

Table A-11, continued: Uniaxial strength test results for Well 15668 core samples.

Top Depth	Formation	Test	D (mm)	L (mm)	W (mm)	psi	Load (N)	Is, MPa	F	Is(50), MPa
9022.8	Neal	a	12	-	24.5	280	3347.94	8.94	0.53	4.71
9022.8	Neal	a	12	-	24.5	200	2391.39	6.39	0.53	3.36
9022.8	Neal	a	7	-	24.5	160	1913.11	8.76	0.41	3.62
9022.8	Neal	a	14	-	24.5	140	1673.97	3.83	0.56	2.16
9022.8	Neal	a	16	-	24.5	180	2152.25	4.31	0.60	2.58
9022.8	Neal	a	4	-	24.5	80	956.55	7.67	0.32	2.46
9024.2	Neal	a	8	-	24.5	180	2152.25	8.62	0.44	3.78
9024.2	Neal	a	7	-	24.5	180	2152.25	9.86	0.41	4.07
9024.2	Neal	a	6	-	24.5	130	1554.40	8.30	0.39	3.20
9024.2	Neal	a	8	-	24.5	160	1913.11	7.67	0.44	3.36
9024.2	Neal	a	11	-	24.5	300	3587.08	10.45	0.51	5.29
9024.2	Neal	a	10	-	24.5	200	2391.39	7.67	0.48	3.72
9024.2	Neal	a	6	-	24.5	120	1434.83	7.67	0.39	2.95
9044.6	Lewis	a	20	-	24.5	40	478.28	0.77	0.66	0.51
9044.6	Lewis	a	23	-	24.5	80	956.55	1.33	0.71	0.94
9062.9	Lewis	a	15	-	24.5	840	10043.82	21.47	0.58	12.49
9073.0	Lewis	a	8	-	24.5	200	2391.39	9.58	0.44	4.20
9062.9	Lewis	i	14	17.0	24.5	700	8369.85	13.81	0.56	7.79

d: diametral test; a: axial test; i: irregular lump; D: distance between platen contact points; L: length of the sample measured from the platen contact point to the edge of the sample; W: width; psi: pounds per square inch; N: load measured in Newton; Is: index strength; MPa: Mega-Pascal; F: correction factor; Is(50): index strength normalized to D=50mm

APPENDIX

Table A-12: TerraTek® XRD analysis of Well 15668 for the Geological Survey of Alabama study by Pashin et al. (2011).

X-RAY DIFFRACTION DATA - Whole Rock and Clay Mineralogy (Weight %)
 GEOLOGICAL SURVEY OF ALABAMA RPSEA Shale Study Lamb 1-3 #1 Well
 TerraTek Project No. 503098 10 May 2010



WHOLE ROCK MINERALOGY

SAMPLE ID	1	2	3	4	5	6	7	8
DEPTH (FT)	9013.20	9016.60	9020.65	9022.90	9024.35	9134.50	9137.20	9140.65
QUARTZ	28	36	31	43	37	35	41	34
K-FELDSPAR	8	16	15	12	3	12	7	15
PLAGIOCLASE	1	3	0	1	6	8	5	3
CALCITE	0	0	2	1	0	0	0	0
ANKERITE/FE-DOLOMITE	0	1	0	0	1	0	2	0
DOLOMITE	4	2	3	4	2	2	0	3
PYRITE	4	4	4	4	6	12	6	4
FLUORAPATITE	0	0	0	1	0	0	0	0
BARITE	0	1	0	0	0	0	4	0
TOTAL NON-CLAY	44	62	54	65	55	68	65	58
ILLITE/SMECTITE (I/S)	24	13	22	11	18	7	0	10
ILLITE+MICA	32	23	23	23	27	25	35	32
KAOLINITE	0	0	0	0	0	0	0	0
CHLORITE	0	2	0	0	0	0	0	0
TOTAL CLAY	56	38	46	34	45	32	35	42
GRAND TOTAL	100	100	100	100	100	100	100	100

RELATIVE CLAY ABUNDANCE IN BULK SAMPLE

% I/S Expandability	20	20	20	20	20	10	10	10
ILLITE/SMECTITE (I/S)	43	34	49	33	39	21	0	23
ILLITE+MICA	57	62	51	67	61	79	100	77
KAOLINITE	0	0	1	0	0	0	0	0
CHLORITE	0	4	0	0	0	0	0	0
TOTAL	100	100	100	100	100	100	100	100
TOTAL EXPANDABLE CLAY	5	3	4	2	4	1	0	1

CLAY MINERALOGY

RELATIVE CLAY ABUNDANCE (LESS THAN 4 MICRON SIZE FRACTION)

SAMPLE ID	1	2	3	4	5	6	7	8
DEPTH (FT)	9013.20	9016.60	9020.65	9022.90	9024.35	9134.50	9137.20	9140.65
% I/S Expandability	20	20	20	20	20	10	10	10
ILLITE/SMECTITE (I/S)	76	70	75	60	74	56	57	51
ILLITE	21	23	19	34	20	44	43	49
KAOLINITE	1	3	3	0	3	0	0	0
CHLORITE	2	4	3	6	3	0	0	0
TOTAL	100	100	100	100	100	100	100	100

APPENDIX

	Quartz	Albite	Calcite	Chlorite	Dolomite	Fluorapatite	Illite	Montmorillonite	Muscovite	Orthoclase	Pyrite	Siderite	Total Clay	SiO2	TiO2	Al2O3	Fe2O3	MnO	MgO	CaO	Na2O	K2O	P2O5	V	Cr	Ni	Cu	Zn	Rb	Sr	Y	Zr	Nb	Ba	Mo	U	TOC	
Quartz	1.00																																					
Albite	-0.42	1.00																																				
Calcite	-0.16	-0.25	1.00																																			
Chlorite	-0.22	0.25	-0.34	1.00																																		
Dolomite	-0.25	-0.01	0.36	-0.21	1.00																																	
Fluorapatite	-0.25	-0.23	-0.18	0.13	-0.10	1.00																																
Illite	-0.31	-0.18	-0.40	0.31	-0.26	0.54	1.00																															
Montmorillonite	-0.13	0.18	0.09	-0.30	0.00	-0.11	-0.16	1.00																														
Muscovite	-0.31	0.51	-0.01	0.01	0.10	-0.21	-0.54	-0.09	1.00																													
Orthoclase	-0.20	0.54	-0.26	-0.07	-0.10	-0.25	-0.35	0.41	0.40	1.00																												
Pyrite	-0.21	0.01	-0.13	0.14	0.09	-0.03	0.39	-0.12	-0.23	-0.12	1.00																											
Siderite	0.00	0.03	0.07	-0.03	-0.09	0.04	0.03	-0.03	-0.05	-0.10	-0.10	1.00																										
Total Clay	-0.62	0.24	-0.51	0.51	-0.26	0.46	0.78	-0.12	0.07	-0.05	0.28	-0.02	1.00																									
SiO2	0.86	-0.16	-0.53	-0.18	-0.40	-0.17	-0.18	-0.01	-0.17	0.14	-0.13	-0.05	-0.36	1.00																								
TiO2	-0.66	0.37	-0.35	0.63	-0.18	0.31	0.68	-0.20	0.03	0.00	0.22	0.00	0.87	-0.50	1.00																							
Al2O3	-0.63	0.31	-0.48	0.67	-0.22	0.38	0.69	-0.19	0.08	0.05	0.29	-0.02	0.93	-0.42	0.95	1.00																						
Fe2O3	-0.66	0.14	-0.19	0.52	0.00	0.51	0.63	-0.19	-0.02	-0.10	0.14	0.16	0.76	-0.62	0.82	0.82	1.00																					
MnO	-0.18	-0.07	0.31	-0.11	0.25	0.29	0.02	0.06	-0.06	-0.23	-0.29	0.28	-0.03	-0.38	0.02	-0.04	0.39	1.00																				
MgO	-0.75	0.22	0.06	0.24	0.63	0.10	0.22	-0.13	0.26	0.01	0.30	-0.03	0.45	-0.72	0.50	0.52	0.61	0.12	1.00																			
CaO	-0.25	-0.12	0.95	-0.42	0.52	-0.20	-0.47	0.19	0.13	-0.16	-0.15	0.04	-0.49	-0.57	-0.38	-0.50	-0.19	0.35	0.17	1.00																		
Na2O	-0.64	0.41	-0.30	0.66	-0.01	0.21	0.62	-0.14	-0.02	-0.07	0.34	-0.07	0.79	-0.51	0.90	0.89	0.72	-0.06	0.57	-0.31	1.00																	
K2O	-0.69	0.37	-0.40	0.51	-0.09	0.29	0.66	-0.14	0.06	0.09	0.49	-0.03	0.86	-0.45	0.87	0.92	0.74	-0.10	0.61	-0.41	0.85	1.00																
P2O5	-0.25	0.31	-0.08	0.30	0.37	0.12	0.27	-0.11	-0.20	-0.20	0.29	-0.07	0.21	-0.28	0.41	0.31	0.35	0.20	0.31	-0.06	0.55	0.33	1.00															
V	-0.55	0.22	-0.33	0.44	-0.04	0.26	0.64	-0.18	-0.09	0.00	0.69	-0.11	0.71	-0.37	0.72	0.76	0.58	-0.21	0.53	-0.35	0.73	0.87	0.31	1.00														
Cr	-0.35	0.25	-0.34	0.21	-0.01	0.14	0.56	-0.05	-0.22	0.01	0.76	-0.13	0.51	-0.17	0.47	0.53	0.33	-0.24	0.38	-0.34	0.59	0.74	0.36	0.84	1.00													
Ni	-0.48	0.29	-0.33	0.32	0.00	0.24	0.64	-0.10	-0.20	-0.02	0.70	-0.08	0.62	-0.30	0.64	0.66	0.52	-0.10	0.47	-0.34	0.69	0.83	0.43	0.88	0.95	1.00												
Cu	-0.41	0.40	-0.25	0.26	0.02	0.16	0.52	-0.10	-0.16	-0.05	0.50	0.05	0.50	-0.30	0.60	0.53	0.49	0.08	0.39	-0.23	0.59	0.71	0.49	0.65	0.79	0.85	1.00											
Zn	-0.49	0.34	-0.28	0.32	0.13	0.18	0.60	-0.11	-0.20	-0.06	0.69	-0.04	0.58	-0.35	0.64	0.62	0.51	-0.06	0.53	-0.26	0.72	0.80	0.54	0.85	0.92	0.95	0.89	1.00										
Rb	-0.72	0.36	-0.34	0.65	-0.11	0.33	0.66	-0.17	0.06	0.03	0.29	0.01	0.89	-0.54	0.96	0.96	0.84	0.02	0.60	-0.35	0.91	0.93	0.36	0.76	0.52	0.68	0.62	0.68	1.00									
Sr	-0.60	0.12	0.56	0.04	0.53	-0.01	0.03	-0.01	0.04	-0.18	0.33	-0.02	0.07	-0.74	0.23	0.14	0.26	0.08	0.58	0.57	0.36	0.28	0.34	0.35	0.24	0.31	0.20	0.39	0.30	1.00								
Y	-0.55	0.39	-0.26	0.52	0.03	0.28	0.64	-0.19	-0.19	-0.12	0.34	0.07	0.67	-0.48	0.86	0.76	0.76	0.19	0.46	-0.27	0.84	0.76	0.73	0.69	0.57	0.71	0.74	0.78	0.82	0.35	1.00							
Zr	0.55	-0.14	-0.04	-0.37	-0.24	-0.17	-0.25	0.03	-0.05	-0.01	-0.39	0.06	-0.39	0.52	-0.36	-0.46	-0.48	-0.02	-0.61	-0.06	-0.54	-0.53	-0.18	-0.55	-0.42	-0.47	-0.28	-0.46	-0.53	-0.55	-0.32	1.00						
Nb	-0.61	0.36	-0.41	0.66	-0.23	0.34	0.68	-0.19	0.01	0.01	0.17	0.11	0.87	-0.45	0.98	0.95	0.83	0.04	0.46	-0.43	0.88	0.85	0.36	0.68	0.43	0.60	0.57	0.60	0.96	0.16	0.83	-0.40	1.00					
Ba	-0.31	0.20	-0.38	0.26	-0.09	0.08	0.53	-0.14	-0.13	0.02	0.64	-0.02	0.53	-0.09	0.48	0.51	0.36	-0.23	0.35	-0.40	0.48	0.69	0.18	0.77	0.71	0.72	0.61	0.70	0.54	0.20	0.49	-0.31	0.44	1.00				
Mo	0.09	-0.05	0.09	-0.11	0.12	-0.06	0.04	-0.09	-0.23	-0.09	0.34	-0.06	-0.16	0.05	-0.16	-0.14	-0.11	0.14	0.01	0.06	-0.07	0.01	0.14	0.19	0.33	0.27	0.25	0.26	-0.10	0.07	0.03	-0.23	-0.14	0.18	1.00			
U	-0.65	0.25	-0.14	0.52	-0.02	0.31	0.63	-0.24	-0.08	-0.10	0.42	0.14	0.71	-0.57	0.83	0.81	0.76	0.08	0.57	-0.20	0.82	0.82	0.41	0.80	0.61	0.74	0.59	0.72	0.85	0.43	0.80	-0.55	0.82	0.54	0.09	1.00		
TOC	0.16	0.08	-0.27	-0.20	0.14	0.36	0.27	0.02	-0.34	-0.07	0.69	-	0.03	0.38	-0.29	-0.05	-0.05	-0.13	0.30	-0.27	0.02	0.65	0.17	0.73	0.96	0.93	0.81	0.89	-0.05	-0.05	0.18	-0.35	-0.31	0.84	0.92	0.22	1.00	

Figure A-1: Correlation coefficient matrix for the Neal shale.

APPENDIX

	Quartz	Albite	Calcite	Chlorite	Dolomite	Fluorapatite	Illite	Montmorillonite	Muscovite	Orthoclase	Pyrite	Total Clay	SiO2	TiO2	Al2O3	Fe2O3	MnO	MgO	CaO	Na2O	K2O	P2O5	V	Cr	Ni	Cu	Zn	Rb	Sr	Y	Zr	Nb	Ba	Mo	U			
Quartz	1.00																																					
Albite	-0.11	1.00																																				
Calcite	-0.62	-0.48	1.00																																			
Chlorite	-0.10	0.42	-0.56	1.00																																		
Dolomite	-0.27	0.60	-0.19	-0.07	1.00																																	
Fluorapatite	-0.15	0.26	-0.36	0.40	0.07	1.00																																
Illite	0.09	0.42	-0.77	0.93	0.08	0.54	1.00																															
Montmorillonite	0.64	-0.14	-0.19	-0.67	0.30	-0.33	-0.42	1.00																														
Muscovite	-0.37	0.56	-0.28	0.15	0.83	0.55	0.35	0.00	1.00																													
Orthoclase	0.30	0.60	-0.88	0.84	0.04	0.52	0.92	-0.28	0.26	1.00																												
Pyrite	0.11	0.46	-0.62	0.80	0.18	-0.11	0.76	-0.29	0.10	0.70	1.00																											
Total Clay	0.00	0.52	-0.76	0.86	0.28	0.60	0.97	-0.37	0.55	0.88	0.71	1.00																										
SiO2	0.87	0.17	-0.90	0.34	-0.16	0.25	0.55	0.34	-0.07	0.72	0.37	0.48	1.00																									
TiO2	0.02	0.69	-0.78	0.88	0.33	0.43	0.94	-0.36	0.49	0.91	0.83	0.96	0.46	1.00																								
Al2O3	0.04	0.52	-0.78	0.91	0.21	0.52	0.99	-0.40	0.46	0.91	0.79	0.99	0.50	0.97	1.00																							
Fe2O3	0.06	0.63	-0.78	0.85	0.37	0.32	0.92	-0.29	0.47	0.87	0.89	0.94	0.47	0.99	0.96	1.00																						
MnO	-0.73	-0.05	0.81	-0.37	0.18	-0.42	-0.56	-0.28	0.05	-0.67	-0.27	-0.49	-0.91	-0.41	-0.50	-0.42	1.00																					
MgO	-0.36	0.61	-0.19	0.06	0.98	0.09	0.19	0.15	0.85	0.11	0.29	0.39	-0.19	0.43	0.33	0.47	0.21	1.00																				
CaO	-0.69	-0.34	0.98	-0.57	0.01	-0.36	-0.77	-0.15	-0.13	-0.88	-0.58	-0.72	-0.95	-0.71	-0.74	-0.72	0.87	0.00	1.00																			
Na2O	0.09	0.69	-0.78	0.80	0.41	0.22	0.87	-0.23	0.45	0.84	0.91	0.89	0.46	0.97	0.92	0.99	-0.36	0.50	-0.70	1.00																		
K2O	0.03	0.58	-0.78	0.91	0.24	0.52	0.98	-0.40	0.47	0.92	0.79	0.99	0.50	0.99	1.00	0.97	-0.49	0.34	-0.74	0.93	1.00																	
P2O5	-0.13	0.61	-0.14	0.56	-0.17	-0.05	0.31	-0.59	-0.20	0.48	0.49	0.23	0.03	0.44	0.32	0.37	0.11	-0.11	-0.14	0.42	0.37	1.00																
V	0.10	0.61	-0.73	0.87	0.23	0.14	0.87	-0.33	0.27	0.85	0.96	0.85	0.46	0.95	0.90	0.97	-0.35	0.34	-0.68	0.98	0.91	0.53	1.00															
Cr	0.22	0.54	-0.64	0.78	0.06	-0.12	0.71	-0.29	-0.02	0.75	0.96	0.64	0.45	0.80	0.73	0.83	-0.29	0.15	-0.62	0.87	0.74	0.67	0.94	1.00														
Ni	0.13	0.73	-0.67	0.78	0.23	0.01	0.73	-0.29	0.17	0.80	0.92	0.70	0.42	0.87	0.77	0.88	-0.26	0.31	-0.61	0.92	0.80	0.70	0.96	0.97	1.00													
Cu	0.17	0.67	-0.54	0.69	0.03	-0.13	0.57	-0.33	-0.06	0.71	0.83	0.51	0.37	0.71	0.60	0.71	-0.17	0.10	-0.51	0.77	0.63	0.85	0.85	0.95	0.95	1.00												
Zn	0.06	0.85	-0.56	0.65	0.29	-0.02	0.57	-0.27	0.18	0.72	0.79	0.56	0.30	0.78	0.63	0.76	-0.14	0.34	-0.48	0.82	0.68	0.80	0.84	0.89	0.96	0.96	1.00											
Rb	0.03	0.55	-0.78	0.91	0.22	0.54	0.99	-0.41	0.46	0.92	0.77	0.99	0.50	0.98	1.00	0.96	-0.50	0.32	-0.74	0.92	1.00	0.35	0.90	0.73	0.78	0.61	0.65	1.00										
Sr	-0.70	-0.23	0.87	-0.42	0.15	-0.38	-0.64	-0.13	-0.10	-0.76	-0.38	-0.59	-0.91	-0.56	-0.60	-0.54	0.73	0.15	0.91	-0.53	-0.60	-0.10	-0.52	-0.47	-0.45	-0.41	-0.33	-0.60	1.00									
Y	-0.01	0.70	-0.55	0.82	0.09	0.11	0.73	-0.52	0.15	0.78	0.84	0.69	0.31	0.85	0.76	0.82	-0.13	0.19	-0.52	0.85	0.79	0.81	0.91	0.92	0.95	0.94	0.92	0.77	-0.45	1.00								
Zr	-0.25	0.81	-0.50	0.74	0.54	0.15	0.70	-0.38	0.50	0.67	0.83	0.75	0.11	0.88	0.78	0.89	-0.05	0.63	-0.38	0.91	0.81	0.57	0.89	0.79	0.89	0.76	0.87	0.79	-0.17	0.84	1.00							
Nb	0.20	0.65	-0.88	0.83	0.26	0.50	0.94	-0.25	0.45	0.96	0.76	0.95	0.63	0.98	0.97	0.96	-0.57	0.34	-0.84	0.94	0.98	0.38	0.91	0.76	0.83	0.68	0.73	0.97	-0.71	0.80	0.78	1.00						
Ba	0.07	0.57	-0.61	0.91	-0.04	0.14	0.82	-0.54	0.05	0.84	0.89	0.74	0.40	0.86	0.82	0.85	-0.28	0.07	-0.60	0.86	0.84	0.75	0.94	0.94	0.94	0.92	0.86	0.83	-0.50	0.97	0.80	0.83	1.00					
Mo	0.10	0.79	-0.44	0.46	0.34	-0.27	0.36	-0.12	0.10	0.52	0.74	0.36	0.22	0.61	0.44	0.62	0.01	0.37	-0.35	0.72	0.48	0.75	0.74	0.84	0.90	0.93	0.96	0.45	-0.23	0.83	0.79	0.56	0.75	1.00				
U	0.11	0.68	-0.72	0.85	0.20	0.12	0.83	-0.35	0.22	0.86	0.93	0.80	0.45	0.93	0.87	0.93	-0.32	0.30	-0.67	0.96	0.88	0.64	0.99	0.96	0.99	0.91	0.91	0.87	-0.52	0.95	0.89	0.90	0.96	0.81	1.00			

Figure A-2: Correlation coefficient matrix for the Lewis Limestone.